Luminescent Molecules in Nanoporous Silicates

Functional Group Distributions and Light-Harvesting Applications

Habilitationsschrift

vorgelegt der

Mathematisch-naturwissenschaftlichen Fakultät

der

Universität Zürich

von

Dominik Brühwiler

von Niederbüren SG

Zürich, 2010

Dank

Prof. Dr. Heinz Berke hat mir die Möglichkeit gegeben, im Verlaufe der letzten 5 Jahre ein unabhängiges Forschungsprogramm zu entwickeln und, mit den notwendigen Freiheiten ausgestattet, zu verfolgen. Ebenso dankbar bin ich für die finanzielle Unterstützung durch den Schweizerischen Nationalfonds, die KTI und das Marie-Curie Programm der EU.

Besonderer Dank gilt den Mitgliedern der Brühwiler Gruppe für den fleissigen Einsatz an vorderster Forschungsfront. Es sind dies, in chronologischer Reihenfolge und mit der bekleideten Rolle in Klammern: Dr. Hanna Ritter (Doktorandin), Dr. Jan Hinrich Ramm (Doktorand), Dr. Le-Quyenh Dieu (Doktorandin), Dr. Dongbin Zhao (Postdoc), Dr. André Devaux (Gast-Postdoc), Nando Gartmann (Master Student und Doktorand), Christina Schütze und Christian Meister (kurz aber effizient), Dr. Christophe Bauer (Postdoc), Dr. Igor Dolamic (Postdoc) und Dr. Thomas Dienel (Postdoc). Es war und ist mir ein Vergnügen mit Euch zusammen zu arbeiten.

Vieles ist leichter wenn die Administration stimmt, seien es Anstellungsverträge, Rechnungen oder ähnliche Zerstreuungen. In diesem Zusammenhang konnte ich mich stets auf den kompetenten Rat von Beatrice Spichtig verlassen. Dem Sachbearbeiterinnen-Team sei ebenso gedankt wie Manfred Jöhri, Hanspeter Stalder, Heinz Spring und Dr. Ferdinand Wild für die Unterstützung im technischen und im analytischen Bereich.

Wissenschaftliche Zusammenarbeiten haben wesentlich dazu beigetragen, meinen Horizont in vielerlei Hinsicht zu erweitern. Prof. Dr. Gion Calzaferri, Dr. Andreas Kunzmann, Prof. Dr. Tomás Torres und Dr. Sophie Brasselet möchte ich für die mehrjährigen, ertragreichen Kollaborationen danken.

Schliesslich geht ein Danke, das nicht gross genug sein kann, an Karin, Alexa und Saskia.

Summary

The unique properties of the defined channel systems of nanoporous silicates, such as zeolites and mesoporous silica, are of interest for a variety of applications, including fields as diverse as catalysis, biological imaging, sensing, adsorption, and drug delivery. Appropriate functionalization of the porous host materials is the key to a successful implementation. Extending the organization provided by a given channel system to a macroscopic level, establishing an interaction with the surrounding medium, or assigning tasks to specific parts of the external and internal surfaces requires multiple degrees of modification. This important aspect of the chemistry of ordered nanoporous materials is discussed with emphasis on the synthetic and analytical challenges associated with the controlled placement of functional groups on mesoporous silica. Luminescent labeling in combination with nitrogen sorption, optical spectroscopy, confocal laser scanning microscopy, and the quantitative analysis of grafted organic moieties provides insights into the parameters that control the distribution of functional groups on mesoporous silica.

The inclusion of luminescent molecules into nanoporous hosts not only serves analytical purposes, but can further lead to materials with intriguing photophysical properties, opening novel possibilities for light-harvesting applications. Obtaining high conversion efficiency at low costs is the key issue in current research on photovoltaics. Concepts that are directed towards a better use of the complete solar spectrum combined with a conversion to light of a narrow wavelength range are particularly promising in this regard. Two novel approaches that fall into this category are discussed, both based on the inclusion of luminescent molecules into the channels of zeolite L crystals. Luminescent solar concentrators employing dye-zeolite antenna materials as active components have the potential to solve the self-absorption problem that has been limiting the commercial viability of such devices for more than 30 years. Similar antenna materials with specifically designed zinc phthalocyanine acceptors are proposed for the sensitization of organic solar cells.

Table of Contents

PART I: The Distribution of Functional Groups on Mesoporous Silica

1. Introduction 1
2. Publication A: Postsynthetic functionalization of mesoporous silica 13
3. Publication B: A comparative study of the functionalization of mesoporous silica MCM-41 by deposition of 3-aminopropyltrimethoxysilane from toluene and from the vapor phase 23
4. Publication C: Distribution of amino groups on a mesoporous silica surface after submonolayer deposition of aminopropylsilanes from an anhydrous liquid phase 31
5. Publication D: Accessibility of amino groups in postsynthetically modified mesoporous silica 41
6. Publication E: Controlling and imaging the functional-group distribution on mesoporous silica 53
7. Publication F: The effect of water on the functionalization of mesoporous silica with 3-aminopropyltriethoxysilane 59
8. Publication G: Direct synthesis and fluorescent imaging of bifunctionalized mesoporous iodopropyl-silica 65

PART II: Dye-Zeolite Materials for Solar Energy Conversion Devices

1. Introduction 75
   - 1.1. General Concepts 75
   - 1.2. Sensitization of Organic Solar Cells 75
   - 1.3. Luminescent Solar Concentrators 78
   - 1.4. Conclusions 80
2. Phthalocyanine-based Stopcocks 82
3. An Advanced Luminescent Solar Concentrator 86
   - 3.1. Self-Absorption: The Problem 86
   - 3.2. Self-Absorption: A Possible Solution 89
   - 3.3. Optimization of the First Prototypes 93
   - 3.4. Future Directions 95
4. Pattern Formation in Zeolite/Polymer Films 100
5. Dye-Zeolite Materials: Scientific Collaborations 107

Appendix

Curriculum Vitae 113
Publications 115
Supervised PhD Theses 118

PART I

The Distribution of Functional Groups on Mesoporous Silica

Financial Support:
Swiss National Science Foundation (Projects 200021-109185 and 200020-117591)
European Commission Marie-Curie RTN *Nanomatch* (MRTN-CT-2006-035884)

1. Introduction

In 1992, researchers at Mobil R&D reported the synthesis of highly ordered mesoporous silica, designated as M41S type materials.[1] In the following years, the preparation of these materials was further developed to provide a wide range of pore sizes and morphologies,[2] as illustrated in Figure 1. The number of scientific publications on mesoporous silica literally exploded, mainly due to potential applications of these materials in various fields, including catalysis[3] and drug delivery[4] (Figure 2).

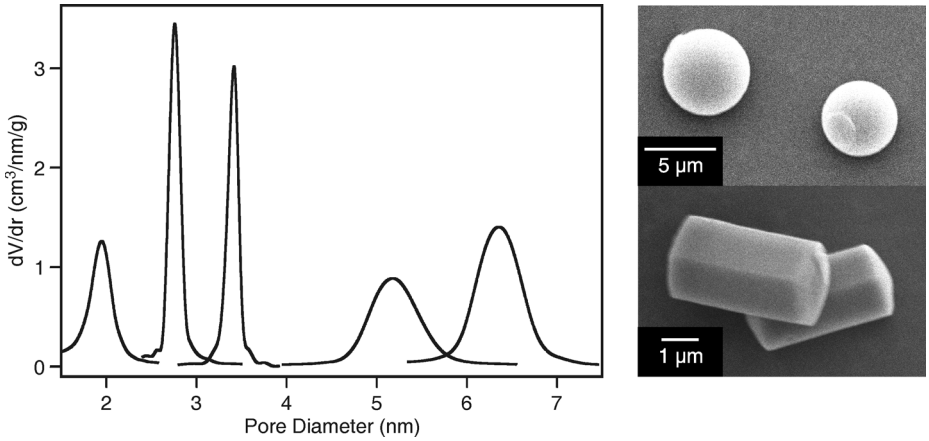

Figure 1. Pore size and morphology of mesoporous silica. Left: Pore size distributions of five different mesoporous silicas, calculated by the BJH method (nitrogen desorption isotherm). Right: Scanning electron microscopy images of spherical and hexagonal mesoporous silica particles (arrays of silica nanochannels, ASNCs).

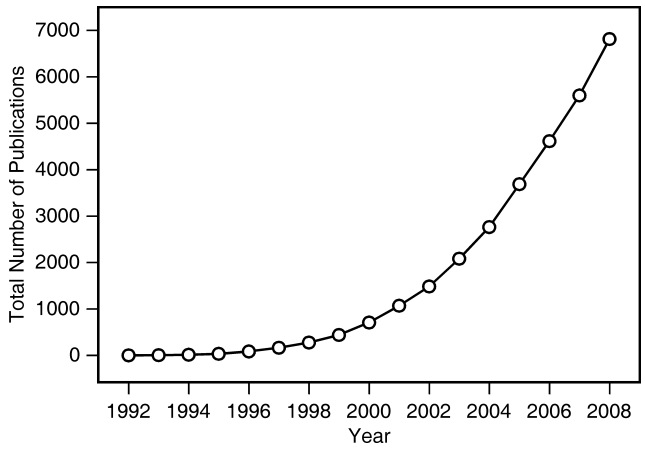

Figure 2. Total number of publications on mesoporous silica according to SciFinder®.

Narrow pore size distributions are typically obtained by means of a structure directing agent (SDA), such as alkyltrimethylammonium ions[1] or block copolymers.[5] The SDA is removed after the formation of the mesoporous framework by calcination at elevated temperatures (typically around 500 °C) or by extraction. Functional groups can be introduced by postsynthetic grafting or co-condensation.[6]

The incorporation of guests into the channels of mesoporous silica can lead to materials with intriguing properties.[7] Proteins and enzymes,[8] DNA,[9] dendrimers,[10] polyoxometalates,[11] preformed quantum dots,[12] fullerenes,[13] luminescent transition metal and rare earth complexes,[14] porphyrins,[15] phthalocyanines,[15,16] and semiconducting polymers[17] are examples of guests that have been included in mesoporous silica. The channel walls are often functionalized prior to the introduction of the guests in order to provide specific adsorption sites or to create an environment in which the guests exhibit ideal properties. This is illustrated by the physisorption of nile red in the channels of MCM-41 (Figure 3). Nile red is a solvatochromic dye that has been extensively used for probing local polarities.[18] Bright luminescence is observed when the surface silanol groups of MCM-41 are capped by reaction with trimethylchlorosilane, creating a hydrophobic environment.

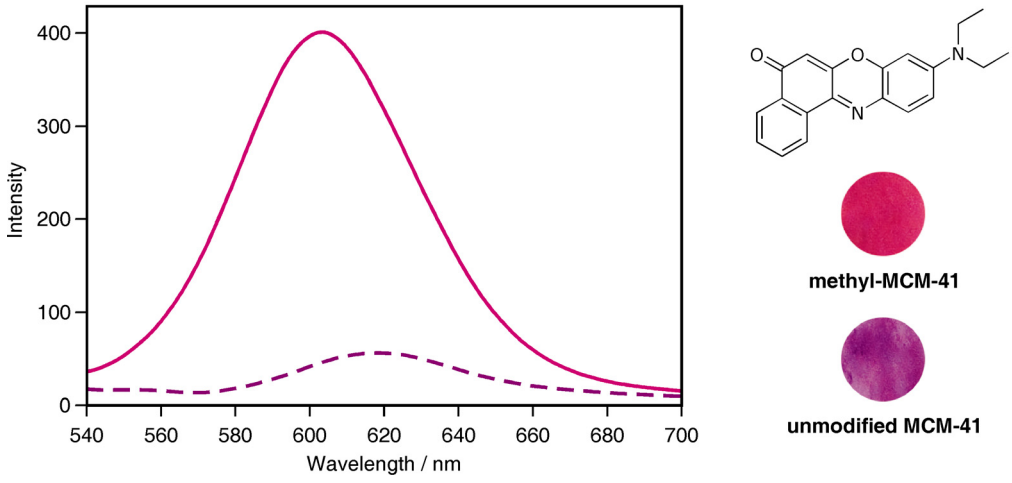

Figure 3. Photoluminescence spectra of nile red in unmodified MCM-41 (dashed) and in MCM-41 after modification of the pore surface with trimethylchlorosilane. Both samples contain approximately the same amount of nile red. Excitation was performed at 500 nm. Photographic images of the samples (powders) are shown on the right.

Several potential applications of mesoporous silica require multi-functionalization. Drug delivery is a classical example where multiple functional groups on specific parts of the mesoporous silica surface are crucial. The development of drug delivery systems based on meso-

porous silica relies on the fact that amorphous silica particles are non-toxic and highly biocompatible. Functional groups on the external particle surface define the interaction with the surrounding medium, solving different tasks, such as targeting, avoiding detection by the immune system, or preventing particle aggregation. In addition to the modification of the external surface, the internal (pore) surface needs to be functionalized independently with moieties for the optimization of drug adsorption. An ideal drug delivery system should further be equipped with stimuli-responsive gates ensuring zero release before reaching the target. The concept of opening and closing mesoporous silica channels by an external physical or chemical stimulus has recently gained substantial interest.[4]

The two key questions concerning the characterization of functional groups on mesoporous silica are "where?" and "how much?". Unfortunately, in many reports, particularly in the field of catalysis, these questions are not well addressed. As a result, conclusions regarding structure-activity relationships are often based on incomplete data and do not contribute to advance the understanding of the respective systems. We set ourselves the goal of introducing methods to control and to analyze functional group distributions on mesoporous silica. The following publications provide an overview of our work in this field. Publication A reviews general approaches and challenges of postsynthetic functionalization of mesoporous silica and serves as a summary of the state of the art in the field.

To investigate the parameters that affect the functional group distribution, we have been mainly focusing on amines, as they are among the most frequently employed groups for the modification of mesoporous silica surfaces. Once the amines are anchored, a further moiety can be coupled by means of amine-reactive derivatives such as isothiocyanates or sulfonyl chlorides. This concept is especially helpful for the analysis of the amino group distributions, as it allows the attachment of labels which amplify the presence of the amino groups in the pores by reducing the pore volume and, in certain cases, the pore diameter. The use of fluorescent labels opens further possibilities for characterizing the functional group distributions by confocal laser scanning microscopy (CLSM).

When studying the surface distribution of different silanes, we found ourselves confronted with the problem of comparability. The structural properties of mesoporous silica (BET surface area, pore volume, pore diameter, external surface area, pore surface area) show slight variation from batch to batch. For comparative studies, it is therefore absolutely necessary to perform experiments with the same parent material. In some cases, this required a scale-up of our experimental procedures. Publication B introduces a scale-up friendly method for the synthesis of high quality MCM-41 (Figure 4).

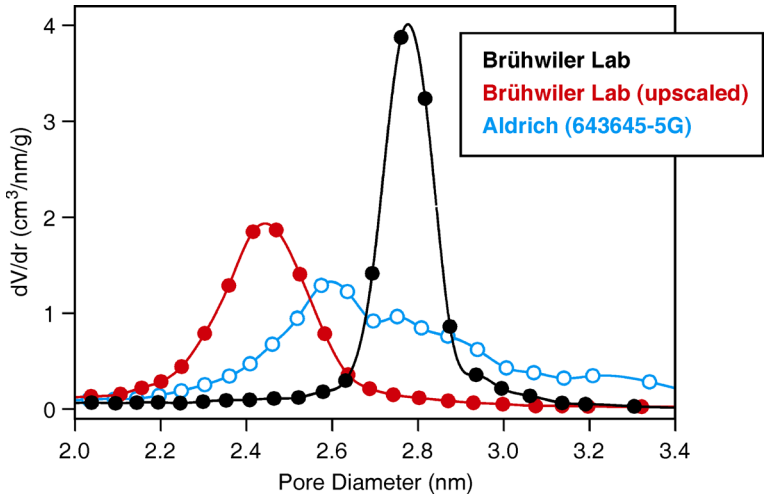

Figure 4. Pore size distributions (BJH, nitrogen desorption isotherms) of MCM-41 prepared by a hydrothermal synthesis[19] (black) and by a scale-up friendly room temperature synthesis[20] (red). A commercial product (blue) is shown for comparison.

The determination of the amount of functional groups on mesoporous silica is challenging. For high functionalization degrees, elemental or thermogravimetric analysis can yield reliable results. However, when attempting to produce a desired functional group distribution, such as a selective modification of the external surface, the amounts of surface-attached moieties are typically in the micromolar range (per gram of silica). To address this important issue, we adapted a procedure from biochemistry, originally developed for the analysis of peptides.[21] This method has proven essential for our work. Details are given in Publication B.

While most published procedures for the postsynthetic functionalization of mesoporous silica employ the deposition of an appropriate alkoxysilane from solution, we found it worthwhile to investigate the deposition from the vapor phase. Indeed, vapor phase deposition offers multiple advantages over the common solvent-based techniques. The elimination of trace water and silane oligomers is straightforward. Furthermore, the absence of a solvent during the deposition and washing of the samples is particularly beneficial for ecological and economical reasons. The results reported in Publication B indicate that amino-functionalized MCM-41 prepared by vapor phase deposition features a narrow pore size distribution, comparing favorably to corresponding samples prepared by reaction in toluene.

Publication C shows that the distribution of amino groups on the mesoporous silica surface can be tuned by adjusting the reactivity of the respective alkoxysilane precursor. By labeling the grafted amino groups with fluorescein and comparing the photoluminescence properties of the samples, we were able to obtain information on the grafting densities. Building upon these results, we investigated the accessibility of the amino groups as a function of the pore

structure and the amount of grafted amino groups (Publication D). We found that nanometer-sized mesoporous silica particles behave differently compared to their micrometer-sized counterparts. Methods for the functionalization of conventional mesoporous silica particles, which are typically micrometer-sized, therefore are not necessarily compatible with mesoporous silica nanoparticles. External surface functionalization seems to be a particularly problematic example in this regard, as the short channels in mesoporous silica nanoparticles lead to increased pore surface accessibility.

Results reported in Publications B, C, and D are mainly based on a careful analysis of the nitrogen sorption data of the parent and the functionalized materials. To identify subtle changes in the pore size distributions, we had to rely on our high quality MCM-41 samples, which feature an extraordinarily narrow pore size distribution. For the imaging of functional group distributions, these samples are, however, unsuitable due to their irregular particle morphology (Figure 5). Evaluating published procedures for the synthesis of large mesoporous silica particles with defined morphology, a report on so-called *arrays of silica nanochannels* (ASNCs) caught our attention. Overcoming initial difficulties concerning the reproducibility of the synthesis (mostly associated with the purity of the starting materials), we were able to prepare well-defined ASNCs with a narrow pore size distribution (Figure 5). In combination with mesoporous silica spheres, ASNCs served as a valuable platform for the imaging of functional group distributions by CLSM and allowed us to test literature procedures for external surface functionalization. Drawing from our previous experience with the analysis of nitrogen sorption data, we proposed an improved concept for placing amino groups on the external surface of mesoporous silica (Figure 6, left). Details are given in Publication E.

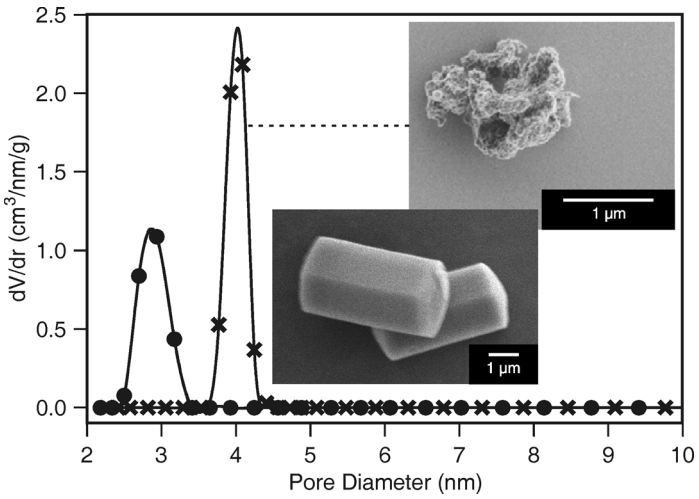

Figure 5. Pore size distributions (NLDFT) of mesoporous silica MCM-41 (hydrothermal synthesis,[19] crosses) and of arrays of silica nanochannels (ASNCs,[22,23] circles).

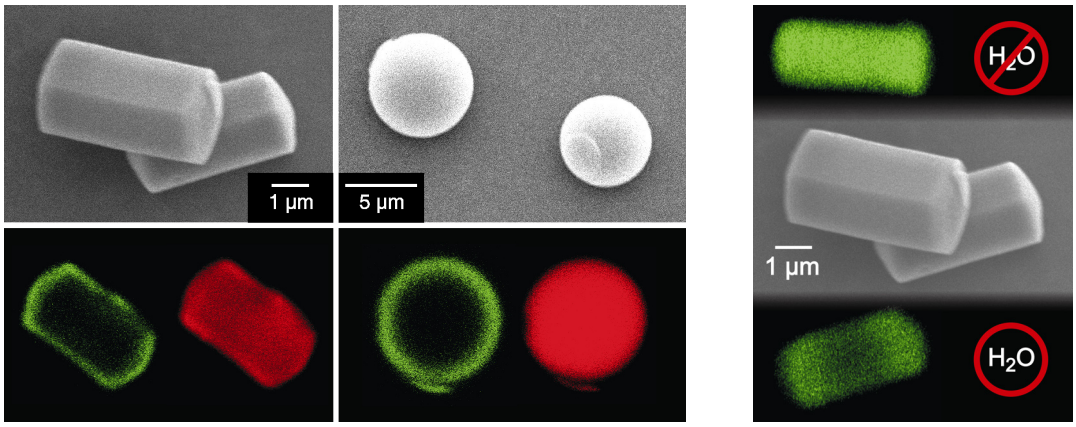

Figure 6. Left: External and internal functionalization of ASNCs and mesoporous silica spheres imaged by CLSM.[23] Right: The effect of water on the functionalization of mesoporous silica with 3-aminopropyltriethoxysilane.[24] Optical slices in the center of the particles were selected.

Reactions of alkoxysilanes with mesoporous silica are usually conducted in a dry solvent. Combining nitrogen sorption data of high quality MCM-41 and CLSM imaging of ASNCs, we investigated the effect of water on the distribution of amino groups (Publication F). With increasing amount of water, clustering of the silane occurs, leading to a non-uniform distribution of the grafted amino groups (Figure 6, right). The combination of nitrogen sorption and CLSM imaging was particularly valuable for establishing guidelines regarding the interpretation of subtle changes in the pore size distribution upon functionalization. In our current work, we are taking this approach one step further by studying CLSM images and nitrogen sorption data of the same material. First results are promising and indicate that complementing nitrogen sorption with CLSM imaging greatly facilitates the interpretation of pore structure data (Figure 7). In agreement with our previous work,[25] we found that monoalkoxysilanes (APDIPES, APDMMS, Figure 8) cause a considerable degree of pore surface functionalization. CLSM images show uniform distributions of fluorescent labels. Pore diameters and pore volumes are significantly reduced after the reaction. APTMEES and BTESPA, on the other hand, are excellent candidates for the selective functionalization of the external surface. It should be noted that the postsynthetic functionalization reported in Figure 7 employs calcined ASNCs with a pore diameter of 3.4 nm. Steric hindrance (APTMEES) and high reactivity (BTESPA) are most likely responsible for the astonishing behavior of these silanes. Interesting results are obtained for APTES, which is by far the most frequently used reagent for the functionalization of silica surfaces. The CLSM images show gradients, with high concentration at the channel entrances. A simple analysis of the pore diameter of the functionalized sample would reveal almost no change compared to the parent material, thus indicating

preferential grafting to the external surface. However, this conclusion would be incorrect, as the pore volume is rather strongly reduced as a consequence of the large amount of pore surface attached organic moieties. The pitfall present in this system is the scarcely functionalized pore body which ultimately determines the pore diameter.

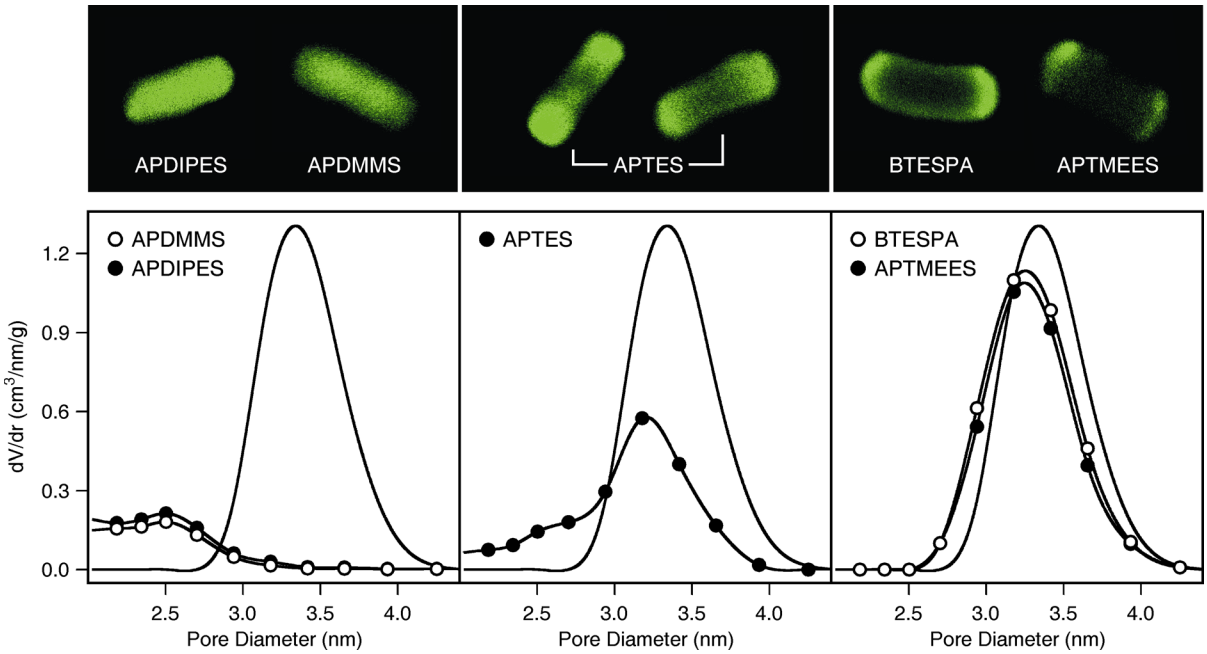

Figure 7. Representative CLSM images of ASNCs after reaction with amino-functionalized alkoxysilanes (see Figure 8 for the structures) and labeling with fluorescein isothiocyanate. The corresponding pore size distributions (before labeling, calculated by NLDFT) are shown in comparison to the parent material (line without points). The amino content of the samples is close to 100 µmol/g.[26]

Enzyme-functionalized mesoporous silica for bioanalytical applications can be seen as an emerging trend in the field of host-guest and inorganic-organic hybrid materials. Immobilization of enzymes in mesoporous silica has been shown to provide increased catalytic activity and stability, as well as possibilities for operation in organic solvents.[27] A general strategy for covalent attachment of the enzymes includes (i) grafting of functional groups (amino or carboxyl) onto the silica, (ii) derivatization with a cross-linking agent, and (iii) enzyme binding. It is obvious that the first step plays a crucial role in determining the final distribution of the enzymes. Having multiple, closely spaced anchoring points with some degree of vertical polymerization might facilitate the stable attachment and reduce leaching. We consider this as a key example where a non-uniform, clustered distribution of amino groups is potentially

more desirable than a uniform distribution. We have shown that the use of BTESPA (Publication C) or the addition of trace water (Publication F) can produce such distributions.

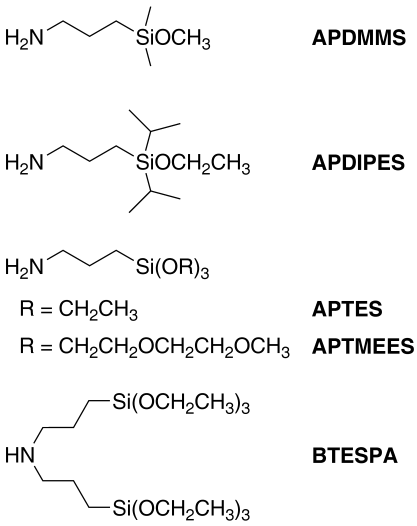

Figure 8. Structures of amino-functionalized alkoxysilanes used for the modification of mesoporous silica.

Part I is closed by a report on a functionalized mesoporous material that cannot be obtained by postsynthetic functionalization, namely a bifunctionalized mesoporous silica containing uniformly distributed iodopropyl groups (Publication G). The presence of iodopropyl groups on the pore surface opens intriguing possibilities for further modification by means of nucleophilic substitution. Co-condensation typically produces materials with uniform distributions of functional groups. Using such a "one-pot" synthesis, we successfully prepared iodopropyl-functionalized mesoporous silica with hydrophobic pore surfaces. The quality of the products thereby strongly depended on the nature of the respective silane additive. Using the same concept, we were able to introduce, in a single step, aminopropyl and iodopropyl moieties, yielding a material with a defined pore size distribution and orthogonal reactivity. Indeed, the two functional groups could be labeled selectively and CLSM imaging indicated that aminopropyl and iodopropyl moieties are uniformly distributed (Figure 9). Despite the considerable particle size, functional groups located in the center of the particles were found to be accessible, even for our relatively large fluorescent labels.

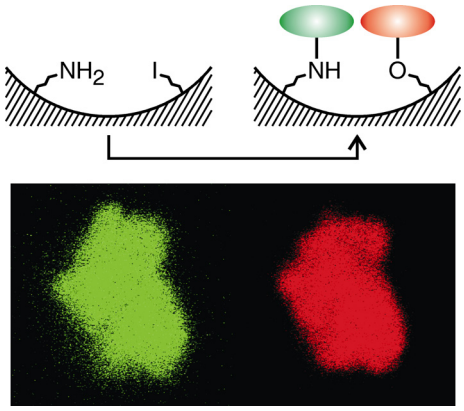

Figure 9. An aminopropyl-iodopropyl-functionalized mesoporous silica is prepared by a one-pot synthesis. CLSM images after selective labeling reveal a uniform distribution and excellent accessibility of both functional groups. The size of the irregular particles is in the order of 5 µm.[28]

In summary, our work has advanced the understanding of functionalization reactions of mesoporous silica with alkoxysilanes. The combination of nitrogen sorption, CLSM, and the quantitative determination of grafted moieties has proven essential for elucidating the parameters that determine the properties of the functionalized products. Future work in this field should concentrate on further extending the toolbox of characterization methods. Surface-selective quenching of fluorescent labels could open interesting possibilities to quantify the relative amounts of externally grafted groups. While the independent functionalization of external and internal surfaces is of particular interest for the development of novel drug delivery and controlled release systems,[4] the placement of active groups in a defined environment or at specific distances from each other is a key issue in the field of heterogeneous catalysis.[3] There is no question that reliable analytical and synthetic methods for such samples need to be developed. Having established novel concepts for the selective functionalization of external surfaces as well as for the general control and analysis of functional group distributions, our results contribute to this challenging task.

As outlined in Part II, we are investigating zeolite-based host-guest systems as optical additives in solar energy conversion devices. The desired optical properties of the respective materials (high optical density, optical anisotropy, energy transfer) are obtained as a consequence of a supramolecular organization of dye molecules in the zeolite channels. While this approach is highly versatile, the choice of guest species is restricted by the fact that zeolites have pore diameters of typically less than 1 nm. For many potential applications of our materials, including luminescent solar concentrators and color changing media, this limiting factor becomes particularly critical, as the desired emission in the red and near-infrared spectral

range is generally associated with molecules featuring extended aromatic systems. We intend to solve this problem by using mesoporous silica with defined channel systems (ASNCs) as host materials. To enable efficient adsorption of guest species, the pore surface needs to be functionalized accordingly. The external surface, on the other hand, has to be adapted to the medium in which the particles are dispersed (typically an organic polymer). Concepts for controlling the distribution of functional groups are essential for such endeavors and further advance – as Ozin and Arsenault put it – the "Escape from the Zeolite Prison".[29]

References (Chapter 1)

1. a) C. T. Kresge, M. E. Leonowicz, W. J. Roth, J. C. Vartuli, J. S. Beck, *Nature* **1992**, *359*, 710; b) J. S. Beck, J. C. Vartuli, W. J. Roth, M. E. Leonowicz, C. T. Kresge, K. D. Schmitt, C. T.-W. Chu, D. H. Olson, E. W. Sheppard, S. B. McCullen, J. B. Higgins, J. L. Schlenker, *J. Am. Chem. Soc.* **1992**, *114*, 10834.
2. a) Y. Wan, D. Zhao, *Chem. Rev.* **2007**, *107*, 2821; b) V. Meynen, P. Cool, E. F. Vansant, *Microporous Mesoporous Mater.* **2009**, *125*, 170.
3. a) A. Taguchi, F. Schüth, *Microporous Mesoporous Mater.* **2005**, *77*, 1; b) M. Hartmann, *Chem. Mater.* **2005**, *17*, 4577; c) J. H. Clark, D. J. Macquarrie, S. J. Tavener, *Dalton Trans.* **2006**, 4297; d) E. L. Margelefsky, R. K. Zeidan, M. E. Davis, *Chem. Soc. Rev.* **2008**, *37*, 1118.
4. a) M. Vallet Regí, *Chem. Eur. J.* **2006**, *12*, 5934; b) J. Lu, M. Liong, J. I. Zink, F. Tamanoi, *Small* **2007**, *3*, 1341; c) I. I. Slowing, B. G. Trewyn, S. Giri, V. S.-Y. Lin, *Adv. Funct. Mater.* **2007**, *17*, 1225; d) M. Vallet-Regí, F. Balas, D. Arcos, *Angew. Chem. Int. Ed.* **2007**, *46*, 7548; e) I. I. Slowing, J. L. Vivero-Escoto, C.-W. Wu, V. S.-Y. Lin, *Adv. Drug Deliv. Rev.* **2008**, *60*, 1278; f) S. B. Wang, *Microporous Mesoporous Mater.* **2009**, *117*, 1; g) K. T. Kim, S. A. Meeuwissen, R. J. M. Nolte, J. C. M. van Hest, *Nanoscale* **2010**, *2*, 844.
5. a) D. Zhao, J. Feng, Q. Huo, N. Melosh, G. H. Fredrickson, B. F. Chmelka, G. D. Stucky, *Science* **1998**, *279*, 548; b) D. Zhao, Q. Huo, J. Feng, B. F. Chmelka, G. D. Stucky, *J. Am. Chem. Soc.* **1998**, *120*, 6024.
6. a) F. Hoffmann, M. Cornelius, J. Morell, M. Fröba, *Angew. Chem. Int. Ed.* **2006**, *45*, 3216; b) D. Brühwiler, *Nanoscale* **2010**, *2*, 887.
7. D. Brühwiler, G. Calzaferri, T. Torres, J. H. Ramm, N. Gartmann, L.-Q. Dieu, I. López-Duarte, M. V. Martínez-Díaz, *J. Mater. Chem.* **2009**, *19*, 8040.

8. a) H. G. Manyar, E. Gianotti, Y. Sakamoto, O. Terasaki, S. Coluccia, S. Tumbiolo, *J. Phys. Chem. C* **2008**, *112*, 18110; b) A. Takimoto, T. Shiomi, K. Ino, T. Tsunoda, A. Kawai, F. Mizukami, K. Sakaguchi, *Microporous Mesoporous Mater.* **2008**, *116*, 601; c) Y. J. Lue, Y. L. Guo, Y. Q. Wang, X. H. Liu, Y. S. Wang, Y. Guo, Z. G. Zhang, G. Z. Lu, *Microporous Mesoporous Mater.* **2008**, *114*, 507; d) D. Jung, C. Streb, M. Hartmann, *Microporous Mesoporous Mater.* **2008**, *113*, 523; e) S. Hudson, E. Magner, J. Cooney, B. K. Hodnett, *J. Phys. Chem. B* **2005**, *109*, 19496; f) A. Salis, D. Meloni, S. Ligas, M. F. Casula, M. Monduzzi, V. Solinas, E. Dumitriu, *Langmuir* **2005**, *21*, 5511; g) C. H. Lee, J. Lang, C. W. Yen, P. C. Shih, T. S. Lin, C. Y. Mou, *J. Phys. Chem. B* **2005**, *109*, 12277; h) Y. J. Wang, F. Caruso, *Chem. Mater.* **2005**, *17*, 953; i) M. Hartmann, *Chem. Mater.* **2005**, *17*, 4577; j) C. H. Lei, Y. S. Shin, J. Liu, E. J. Ackerman, *J. Am. Chem. Soc.* **2002**, *124*, 11242; k) H. Takahashi, B. Li, T. Sasaki, C. Miyazaki, T. Kajino, S. Inagaki, *Chem. Mater.* **2000**, *12*, 3301; l) J. Felipe Diaz, K. J. Balkus, *J. Mol. Catal. B* **1996**, *2*, 115.
9. a) F. Gao, P. Botella, A. Corma, J. Blesa, L. Dong, *J. Phys. Chem. B* **2009**, *113*, 1796; b) S. M. Solberg, C. C. Landry, *J. Phys. Chem. B* **2006**, *110*, 15261.
10. I. Díaz, B. García, B. Alonso, C. M. Casado, M. Morán, J. Losada, J. Pérez-Pariente, *Chem. Mater.* **2003**, *15*, 1073.
11. a) W. Xu, Q. Luo, H. Wang, L. C. Francesconi, R. E. Stark, D. L. Akins, *J. Phys. Chem. B* **2003**, *107*, 497; b) J. A. F. Gamelas, D. V. Evtuguin, A. P. Esculcas, *Trans. Met. Chem.* **2007**, *32*, 1061; c) N. V. Maksimchuk, M. S. Melgunov, Y. A. Chesalov, J. Mrowiec-Bialon, A. B. Jarzebski, O. A. Kholdeeva, *J. Catal.* **2007**, *246*, 241; d) D. Kumar, C. C. Landry, *Microporous Mesoporous Mater.* **2007**, *98*, 309.
12. a) X. Gao, S. Nie, *J. Phys. Chem. B* **2003**, *107*, 11575; b) T. Hirai, H. Okubo, I. Komasawa, *J. Phys. Chem. B* **1999**, *103*, 4228; c) J. Zhang, B. Han, Z. Hou, Z. Liu, J. He, T. Jiang, *Langmuir* **2003**, *19*, 7616; d) W.-S. Chae, J.-H. Yoon, H. Yu, D.-J. Jang, Y.-R. Kim, *J. Phys. Chem. B* **2004**, *108*, 11509.
13. a) S. Minakata, R. Tsuruoka, M. Komatsu, *J. Am. Chem. Soc.* **2008**, *130*, 1536; b) S. Subbiah, R. Mokaya, *J. Phys. Chem. B* **2005**, *109*, 5079; c) J. R. Herance, E. Peris, J. Vidal, J. L. Bourdelande, J. Marquet, H. García, *Chem. Mater.* **2005**, *17*, 4097; d) A. Govindaraj, M. Nath, M. Eswaramoorthy, *Chem. Phys. Lett.* **2000**, *317*, 35.
14. a) M. Ogawa, T. Nakamura, J. Mori, K. Kuroda, *J. Phys. Chem. B* **2000**, *104*, 8554; b) M. Ogawa, T. Nakamura, J. Mori, K. Kuroda, *Microporous Mesoporous Mater.* **2001**, *48*, 159; c) M. Sohmiya, Y. Sugahara, M. Ogawa, *J. Phys. Chem. B* **2007**, *111*, 8836; d) S. Li, H. Song, W. Li, X. Ren, S. Lu, G. Pan, L. Fan, H. Yu, H. Zhang, R. Qin, Q. Dai, T. Wang, *J. Phys. Chem. B* **2006**, *110*, 23164.

15. M. Wark, in *The Porphyrin Handbook*, ed. K. M. Kadish, K. M. Smith, R. Guilard, Elsevier Science, USA, 2003, Vol. 17, pp. 247–283.
16. W. Xu, H. Guo, D. L. Akins, *J. Phys. Chem. B* **2001**, *105*, 1543.
17. a) W. C. Molenkamp, M. Watanabe, H. Miyata, S. H. Tolbert, *J. Am. Chem. Soc.* **2004**, *126*, 4476; b) A. J. Cadby, S. H. Tolbert, *J. Phys. Chem. B* **2005**, *109*, 17879.
18. a) M. M. G. Krishna, *J. Phys. Chem. A* **1999**, *103*, 3589; b) J. L. Meinershagen, T. Bein, *J. Am. Chem. Soc.* **1999**, *121*, 448; c) G. Hungerford, J. A. Ferreira, *J. Lumin.* **2001**, *93*, 155; d) A. Cser, K. Nagy, L. Biczók, *Chem. Phys. Lett.* **2002**, *360*, 473; e) T. M. R. Viseu, G. Hungerford, A. F. Coelho, M. I. C. Ferreira, *J. Phys. Chem. B* **2003**, *107*, 13300.
19. D. Brühwiler, H. Frei, *J. Phys. Chem. B* **2003**, *107*, 8547.
20. H. Ritter, M. Nieminen, M. Karppinen, D. Brühwiler, *Microporous Mesoporous Mater.* **2009**, *121*, 79.
21. a) M. Weigele, S. L. DeBernardo, J. P. Tengi, W. Leimgruber, *J. Am. Chem. Soc.* **1972**, *94*, 5927; b) S. Udenfriend, S. Stein, P. Böhlen, W. Dairman, W. Leimgruber, M. Weigele, *Science* **1972**, *178*, 871.
22. Y. Kievsky, I. Sokolov, *IEEE Trans. Nanotechnol.* **2005**, *4*, 490.
23. N. Gartmann, D. Brühwiler, *Angew. Chem. Int. Ed.* **2009**, *48*, 6354.
24. N. Gartmann, C. Schütze, H. Ritter, D. Brühwiler, *J. Phys. Chem. Lett.* **2010**, *1*, 379.
25. H. Salmio, D. Brühwiler, *J. Phys. Chem. C* **2007**, *111*, 923.
26. N. Gartmann, D. Brühwiler, manuscript in preparation.
27. C. Ispas, I. Sokolov, S. Andreescu, *Anal. Bioanal. Chem.* **2009**, *393*, 543.
28. J. H. Ramm, N. Gartmann, D. Brühwiler, *J. Colloid Interf. Sci.* **2010**, *345*, 200.
29. G. A. Ozin, A. C. Arsenault, in *Nanochemistry*, RSC Publishing, 2005, p. 379.

2. Publication A

Postsynthetic functionalization of mesoporous silica

Dominik Brühwiler

Institute of Inorganic Chemistry, University of Zurich, Winterthurerstrasse 190, 8057 Zurich, Switzerland

Nanoscale 2 (2010) 887 – 892

Abstract. Functionalized mesoporous silica offers promising possibilities for numerous applications, including drug delivery, catalysis, and adsorption. This minireview focuses on recent developments related to the postsynthetic positioning of functional groups on mesoporous silica. After briefly introducing the reagents that are commonly used for this purpose, methods to control and to analyze the distribution of the grafted functional groups are discussed, with particular emphasis on concepts that allow the placement of the groups at specific distances from each other, as well as on approaches towards the selective functionalization of the external particle surface.

Introduction

Following a recommendation by IUPAC, porous materials are divided into three classes, namely microporous (with a pore diameter below 2 nm), mesoporous (2 – 50 nm), and macroporous (larger than 50 nm) materials.[1] Zeolites, the most prominent members of the microporous class, have a long history in terms of their synthesis,[2] beginning with the pioneering work of Barrer in the late 1940s.[3] Mesoporous silicas with ordered pores (hereafter referred to simply as mesoporous silica) are young by comparison, with first reports dating back to the early 1990s.[4] Since then, progress has been remarkable, leading to a rich palette of structure-directing agents (SDAs) and a variety of synthetic pathways.[5] The functionalization of mesoporous silica has attracted particular interest, mainly due to potential applications of these materials in catalysis,[6] drug delivery,[7] and adsorption.[8,9]

There are two general approaches towards the functionalization of mesoporous silica (Figure 1). In *co-condensation*, also termed *direct* or *one-pot synthesis*, a condensable precursor bearing the desired functional group is added to the mixture containing the components for the formation of the mesoporous silica. In most cases, silanes of the type R–Si(OR')$_3$ are used as precursors. The distribution of the functional groups in the final products is typically homogeneous, but the addition of organoalkoxysilanes can have a pronounced effect on the pore structure and morphology of the mesoporous material.[10] High functionalization degrees often lead to decreasing mesoscopic order. The SDA must ultimately be removed by extraction, as calcination would destroy the grafted organic moieties. Extending the co-condensation approach to bridged organosilica precursors of the type (R'O)$_3$Si–R–Si(OR')$_3$ yields Periodic Mesoporous Organosilicas (PMOs).[11] *Postsynthetic* methods (often referred to as *grafting*) introduce the functional groups after the formation of the mesoporous silica, either before or after removal of the SDA. This method exploits the abundant silanol groups present on the mesoporous silica surface.[12] Postsynthetic functionalization offers possibilities for functional group placement. Specific parts of the mesoporous silica surface (external surface, pore surface, pore entrances) can be modified and high functionalization degrees are feasible without compromising the mesoscopic order. This minireview focuses on recent progress in postsynthetic functionalization of mesoporous silica, with particular emphasis on the control and the analysis of the distribution of surface-anchored organic functionalities.

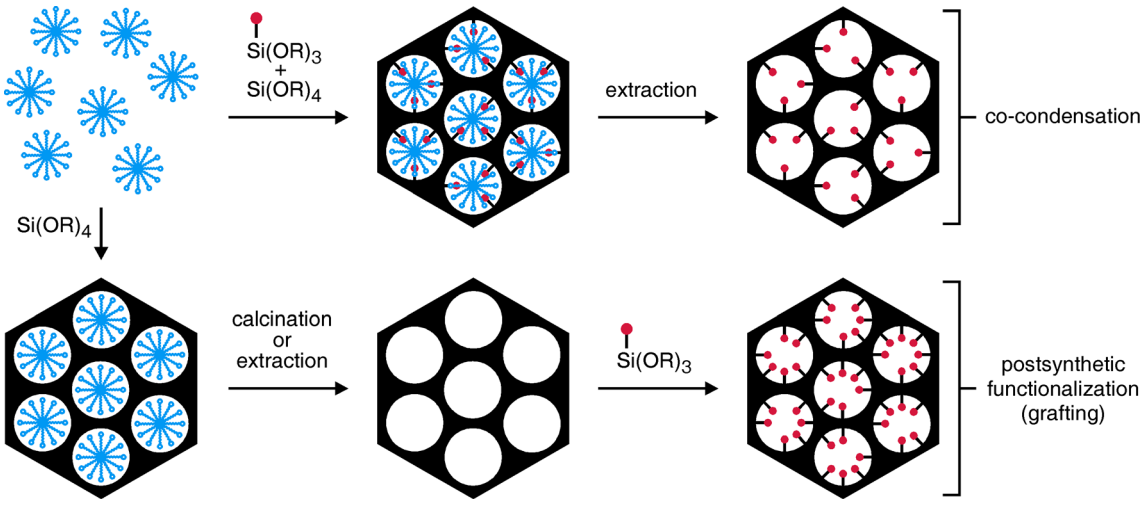

Figure 1. Functionalization of mesoporous silica by co-condensation and by postsynthetic treatment. A trialkoxysilane molecule bearing a functional moiety (red) is shown as an example of a precursor. The structure-directing agent (SDA) is represented by the blue micelles.

Anchoring of functional groups

Precursors for the postsynthetic functionalization of mesoporous silica are most often based on chlorosilanes or alkoxysilanes. Disilazane compounds of the type $HN(SiR'R''_2)_2$ have been reported as an interesting alternative.[13] A further possibility, resulting in the formation of a $Si_{surface}$–C bond instead of the more common attachment via siloxane bridges, is the use of Grignard reagents after esterification of the surface silanol groups.[14] Grignard reagents can also be employed in combination with a dehydroxylation of the silica surface. This postsynthetic modification route relies on the formation of strained siloxane bridges upon vacuum degassing at elevated temperatures, thereby generating electron deficient surface silicon atoms.[15] In addition to Grignard reagents, organolithium compounds can be used to functionalize mesoporous silica surfaces. Reactions are performed at relatively low temperatures compared to the classical alkoxysilane-based grafting techniques.[16] The concept of functionalization via metalorganic reagents has also been applied to colloidal suspensions containing mesoporous silica nanoparticles.[17]

The postsynthetic functionalization of mesoporous silica is usually performed in a solvent. In the case of 3-aminopropyltrimethoxysilane (APTMS), functionalization by deposition from the vapor phase has been reported, leading to materials that compare favorably with those prepared by deposition from toluene.[18] As a further alternative to the common solution-based reactions, materials containing $Si_{surface}$–NH_2 sites have been obtained by treatment of mesoporous silica with gaseous NH_3 at elevated temperatures.[19]

The effect of water on the functionalization of mesoporous silica with 3-aminopropyltriethoxysilane (APTES) was investigated by nitrogen sorption and confocal laser scanning microscopy (CLSM). It was observed that clustering of the silanes is promoted by the presence of water, leading to non-uniform distributions of the grafted amino groups with higher concentrations at the pore entrances.[20] If a uniform distribution of the amino groups is desired, the reaction of 3-aminopropyltrialkoxysilanes with mesoporous silica is therefore usually performed in an anhydrous solvent. It should, however, be mentioned that for the formation of self-assembled monolayers on mesoporous silica by reaction with 3-mercaptopropyltrimethoxysilane, the presence of water (approximately 2 monolayers) in the reaction mixture was found to be of critical importance for generating the respective hydroxysilane, which acts as the key species in the self-assembly process. Furthermore, a hydrated mesoporous silica surface provides the large number of silanol groups that is needed for the formation of self-assembled monolayers.[9,21]

A postsynthetic approach not explicitly shown in Figure 1 introduces functional groups by exchanging the SDA in the as-synthesized mesoporous material with suitable organosilanes. Functionalization according to this approach has for example been achieved by exchanging the cetyltrimethylammonium ions in as-synthesized MCM-41 with positively charged organoalkoxysilanes.[22] It has further been shown that any suitable organoalkoxy- or organochlorosilane is able to displace the SDA from as-synthesized MCM-41 and covalently bind to the pore surface in the process. By following this approach and conducting the reactions without additional solvent, high functionalization degrees were obtained.[23] It should, however, be noted that materials synthesized by methods based on such exchange processes usually contain residual amounts of non-exchanged SDA.

Many postsynthetic modification routes make use of additional reaction steps to convert grafted functional groups, including the oxidation of –SH to $–SO_3H$ by treatment with H_2O_2,[24] the cleavage of grafted disulfide species of the type $[Si](CH_2)_3SS(CH_2)_3[Si]$, leading to pairs of $–(CH_2)_3SH$ groups on the mesoporous silica surface,[25] or the hydrolysis of –CN to –COOH.[26] Countless possibilities exist for attaching further moieties to grafted functional groups. In the extreme case, a series of such steps can lead to highly complex structures, as demonstrated by the synthesis of melamine-based dendrimers in the pores of amino-functionalized mesoporous silica.[27]

Conventional spectroscopic techniques can be used to characterize grafted functional groups. To confirm the integrity of the anchored organic moieties, FTIR, Raman, and ^{13}C MAS NMR spectroscopy is most commonly applied,[13,17,25,28] whereas ^{29}Si MAS NMR data can provide evidence for the presence of Si–C bonds[14–16] and give information on the degree of organic functionalization.[28] The amount of grafted organic moieties is usually determined by elemental or thermogravimetric analysis.

Distribution of functional groups

It is often proposed that postsynthetic modification leads to preferential functionalization of the most readily accessible sites, i.e., sites on the external particle surface and sites on the pore surface close to the pore entrances. The degree of non-uniformity of the final functional group distribution strongly depends on the size of the grafting reagent relative to the pore diameter. Lim and Stein compared vinyl-functionalized MCM-41 samples prepared either by postsynthetic grafting or by co-condensation.[28] A kinetic study of the bromination of the samples revealed that the bromination rate of the postsynthetically functionalized sample was significantly faster than for the co-condensed material, despite a similar pore diameter. One possible explanation for this effect is based on the distribution of the vinyl groups. Contrary to the uniform distribution in the co-condensed sample, vinyl groups in the postsynthetically modified sample are present mainly on the external surface and on the pore surface close to the openings. This hypothesis was supported by X-ray photoelectron spectroscopy (XPS). As the escape depth of electrons is only a few nanometers, XPS emphasizes contributions from the external surface. Measurements on the brominated samples indeed indicated a higher bromine content for the postsynthetically modified sample, whereas bromine contents obtained from bulk chemical analysis were almost equal for co-condensed and postsynthetically functionalized samples. A similar comparison between the two synthesis methods was made by Yokoi et al., focusing on the functionalization with mono-, di-, and tri-amino-organoalkoxysilanes.[29] Adsorption of Co^{2+} and Fe^{3+} was significantly different for the co-condensed and postsynthetically modified samples. The results were explained by a non-uniform distribution of the amino groups in the postsynthetically modified sample, with higher concentrations on the external surface and on the pore surface near the openings. It should be noted that in these comparative studies, postsynthetic functionalization was performed by refluxing a dispersion of the mesoporous silica in toluene containing the respective trichloro- or trialkoxysilane. Several authors have found that in terms of obtaining a uniform distribution of surface-anchored amino groups, toluene is not an ideal solvent. Sharma et al. grafted 3-aminopropyl and *N*-(2-aminoethyl)-3-aminopropyl groups to MCM-41 using different solvents and analyzed the degree of aggregation of the surface-anchored functional groups colorimetrically with Cu^{2+} complexes.[30] Particularly in the case of *N*-(2-aminoethyl)-3-aminopropyl moieties, reaction in toluene produced clusters, whereas reaction in alcohols resulted in a higher degree of site isolation. We have made a similar observation for the reaction of bis(trimethoxysilylpropyl)amine with MCM-41.[31] While grafting in toluene caused an accumulation of anchored groups on the external surface and at the pore entrances, reaction in THF produced a significantly higher degree of site isolation and led to an increased tendency towards a more uniform functionalization of the pore surface. Such solvent effects are less pronounced in the case of weakly interacting silanes, such as APTMS,[30,31] but are nevertheless likely to play an important role in determining the properties of the functionalized products. A very distinct solvent effect was observed upon reaction of 3-aminopropyltris(methoxyethoxyethoxy)silane (APTMEES) with hexagonal MCM-41 type particles.[32] Fluorescent labeling of the grafted amino groups and subsequent analysis by CLSM showed that labeled amino groups were mainly present on the external particle surface and at the pore entrances when the grafting reaction was carried out in toluene or hexane, whereas a uniform distribution was obtained for ethanol or acetone. Using THF as a solvent led to an intermediate behavior, featuring a decrease of the concentration of labeled amino groups towards the center of the pores.

For catalytic applications of functionalized mesoporous silica, it is important to establish molecular scale structure-property relationships. This process is greatly facilitated if the grafted catalytically active groups experience similar environments and are isolated from each other. The molecular spacer approach, which is schematically shown in Figure 2, is very versatile in this regard. Obtaining site-isolated surface-grafted amino groups is particularly challenging, as they tend to interact with adjacent surface silanol groups or arrange in clusters with amine-amine hydrogen bonding. McKittrick and Jones have used a tritylimine patterning agent to control the minimum distance between the surface-anchored amino groups. After grafting of the tritylimine, the remaining silanol groups were capped with hexamethyldisilazane, and the tritylimine was hydrolyzed to yield the primary amino groups.[33] The use of a benzyl instead of a trityl protecting group led to higher grafting densities, approaching those of highly loaded amino-functionalized silicas synthesized by conventional techniques, while still retaining a high degree of site

isolation.[34] In an approach more direct than the concept outlined in Figure 2, site-isolated amino groups have also been obtained by reacting a mixture of APTMS and methyltrimethoxysilane with mesoporous silica.[35]

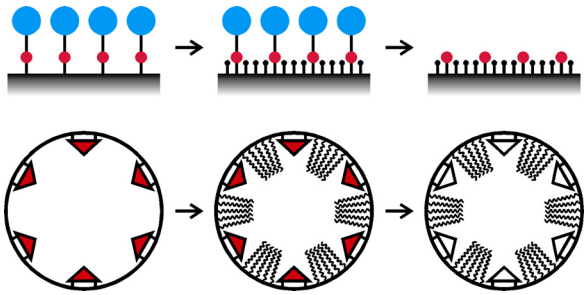

Figure 2. Top: Schematic illustration of the molecular spacer approach. A functional group (red) bearing a bulky protecting group (blue) is grafted to the pore surface. The remaining silanol groups are then capped to obtain the desired surface properties and the protecting groups are removed. The size of the protecting group determines the minimum distance between the functional groups. Bottom: Molecular imprinting approach for the creation of defined cavities in a pore surface coated monolayer.

Imprinting[36] and site pairing[37] methods have been applied to mesoporous silica to control the relative positioning of functional groups. A mesoporous silica coated by a molecular monolayer containing cavities of defined size and shape can be prepared by such an imprinting approach, as shown schematically in Figure 2. In this particular case, a triangular template molecule was grafted to the pore surface, followed by the reaction of the unoccupied surface with a long-chain alkyltrimethoxysilane. The template molecules were then removed to leave the desired cavities in the monolayer coating.[38] Interestingly, it was found that the accessibility of these cavities can be changed. In toluene, the long hydrocarbon chains assume an extended conformation, thus making the cavities accessible. In ethanol, on the other hand, the chains form a more compact conformation, resulting in a blocking of the cavities.[38]

Independent of the grafting method, the assessment of the degree of site isolation is a key issue. Amino-functionalized samples can be labeled with fluorescein isothiocyanate under mild conditions. The luminescence intensity of the labeled samples is a direct measure of the degree of site isolation, as short distances between the amine sites lead to self-quenching.[31] This method is particularly useful for samples with loadings on the order of 0.1 mmol/g. For higher amino loadings, the adsorption of 1-pyrenecarboxylic acid can provide information on site isolation.[34] Short distances between adsorbed pyrene moieties cause excimer emission, which can be easily identified by a broad band in the luminescence spectrum around 470 nm. A further method relies on the formation of Cu^{2+} complexes with grafted amino groups. The d-d absorption spectrum of these complexes allows conclusions regarding the number and arrangement of amine ligands on the Cu^{2+}.[30] Site isolation in amino-functionalized mesoporous silica has also been probed by reaction with terephthaloyl chloride.[33] A short distance between surface-anchored amino groups allows the formation of a bridged species by reaction with both acyl chloride functionalities on the terephthaloyl chloride, leading to two amide bonds. However, if the grafted amino groups are site-isolated, only one of the acyl chloride functionalities is expected to react. The materials were characterized by Raman spectroscopy to identify the relative amount of amide bonds.[33]

Selective functionalization

Functional groups on the external particle surface define the interaction of mesoporous silica particles with the surrounding medium. Regarding applications in the field of drug delivery, the selective functionalization of the external surface is an essential synthesis step to obtain multifunctional carriers. Regulation of the cellular uptake[39] or targeting[40] are examples of tasks that can be solved by functional groups on the external surface. Additionally, the internal surface needs to be functionalized independently, for example to enable high drug loading capacity and controlled release.[7]

One of the first reports of a site-directed surface derivatization of mesoporous silica was motivated by the potential of mesopore confinement effects in catalysis. To exclude binding of catalytic centers to external surface sites, Shephard et al. developed a method to passivate the external surface.[41] Based on the assumption that the most kinetically available silanol groups are those on the external surface, treatment of MCM-41 with small amounts of diphenyldichlorosilane (Ph_2SiCl_2, 20 µL/g) was expected to deactivate the

external surface for further reaction. Subsequent grafting of APTMS would then lead to an exclusive amino-functionalization of the pore surface. The position of the surface-grafted amino groups was determined by high-resolution transmission electron microscopy following acidification (to generate surface-anchored ammonium groups) and adsorption of a ruthenium cluster compound. Indeed, a sample without Ph_2SiCl_2 treatment showed strong contrast on the external surface of the particles, whereas for a passivated sample, ruthenium clusters were found in the mesopores.

A strategy for the differential functionalization of Acid-Prepared Mesoporous Spheres (3 nm average pore diameter, 5 μm particle size) employing diffusion-based deprotection was proposed by Cheng and Landry.[42] The material was first reacted with Fmoc-modified organosilanes, leading under certain conditions to a complete filling of the pores. As the cleavage of the Fmoc groups is much slower within the pores, the external surface groups could be deprotected selectively and modified further. CLSM can be used to visualize the spatial distribution of the functional groups after appropriate fluorescent labeling. Large particles of defined morphology are advantageous for this type of analysis. Arrays of silica nanochannels (ASNCs)[43] and large spherical mesoporous silica particles[42,44] are examples for materials that are ideally suited for such studies.

Grafting of 3-aminopropyltrialkoxysilanes to as-synthesized mesoporous silica, i.e., before the removal of the SDA, is a straightforward method for external surface modification. Intuitively, one would assume that the SDA blocks the pores and therefore prevents the silane molecules from grafting to the pore surface (Figure 3). Following this approach, we found that the degree of pore surface grafting strongly depends on the organosilane. In case of the frequently used APTES, significant derivatization of the pore surface was found for ASNCs (MCM-41 type material, 2.9 nm average pore diameter) and SBA-15 type spheres (5.5 nm average pore diameter) despite the presence of the respective SDA in the pores. APTMEES, on the other hand, grafted preferentially to external surface sites (Figure 3). The mesopores remained accessible for further modification after functionalization of the external surface with APTMEES.[32]

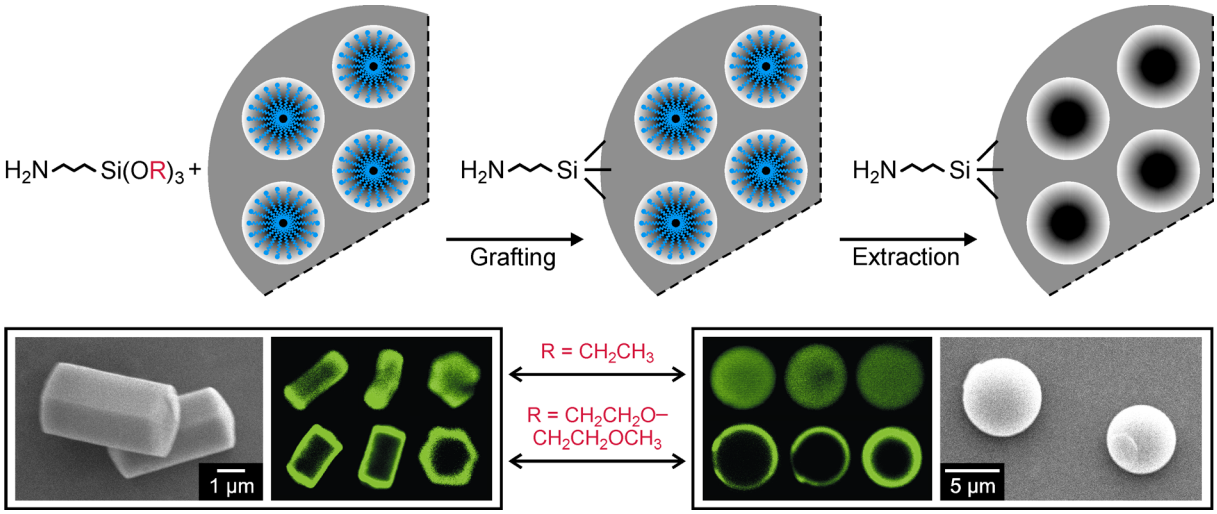

Figure 3. Top: Schematic representation of external surface functionalization by grafting to as-synthesized mesoporous silica. Bottom: Scanning electron microscopy images of ASNCs (left) and mesoporous silica spheres (right). The corresponding CLSM images taken after fluorescent labeling of the amino groups indicate that the degree of pore surface grafting strongly depends on the type of silane. Three particles are shown for each silane/silica combination. Optical slices in the center of the particles were selected.[32]

The concept of reacting alkoxysilanes with mesoporous silica still containing the SDA has been utilized to attach molecular gates at the pore entrances, enabling controlled uptake and release.[45] The positioning of molecules at the channel entrances of mesoporous silica is a challenging task. In the case of zeolite L, a microporous aluminosilicate, a wide variety of molecules has been developed that can be selectively adsorbed or covalently attached to the channel entrances.[46] As this approach typically relies on a moiety that is just slightly too bulky to enter the zeolite L channels, direct application to the much larger pore openings of mesoporous materials is hardly possible. However, the recent development of molecular nanovalves based on redox-switchable bistable rotaxanes shows that highly sophisticated materials can be prepared by carefully controlling the location of functional moieties on the mesoporous silica surface.[47]

Studies on the selective functionalization of external surfaces are usually conducted with micrometer-sized mesoporous silica particles, allowing for example the visualization of the functional group distribution by CLSM. It should, however, be noted that procedures developed for such particles are not necessarily successful when working with nanometer-sized mesoporous silica particles. As a consequence of the shorter channels, the overall accessibility of the pore surface sites is much higher in nanometer-sized particles than in micrometer-sized particles having the same pore diameter.[48] For mesoporous silica nanoparticles, a sequential co-condensation approach has been proposed as an alternative to postsynthetic routes. It has been shown that functional groups can be concentrated in parts of the mesopores, or exclusively placed on the external surface, by adding the respective functionalized triethoxysilane during a specific time of the particle growth.[49]

Depending on the synthesis conditions, mesoporous silica of the SBA-15 type[50] exhibits a significant amount of disordered micropores.[51] There is evidence for the preferential adsorption of APTMS in the intrawall micropores of SBA-15.[48] In fact, micropores in SBA-15 can be functionalized independently from the primary mesopores by first cleaving and removing the accessible part of the SDA, thus exposing the mesopore surface. The latter is then functionalized and the material is heated to vacate the micropores. In a final step the open micropores are modified to yield a bifunctional material.[52]

Conclusions

Given the variety of reagents for the postsynthetic modification of mesoporous silica, including alkoxysilanes, chlorosilanes, disilazanes, organolithium and Grignard reagents, the possibilities for preparing mesoporous materials with specific functionalities are enormous. For many potential applications of these materials, a controlled functional group placement is crucial. Grafting methods that position functional groups in a defined environment or at specific distances from each other are of particular interest for the development of catalysts and sensors, whereas the selective functionalization of specific regions of the mesoporous silica surface (external surface, pore surface, pore entrances) constitutes an integral part of the concept of using these materials as drug delivery devices. Recent years have seen significant progress in this regard, in part due to the application of sophisticated methods for the analysis of the spatial distribution of the grafted functional groups. Considering the wide pore size and particle size range covered by mesoporous silica, the development of generally applicable methods for the selective functionalization of mesoporous silica surfaces remains a challenge.

Acknowledgements

Our work in the field of functionalized silicate-based porous materials is financially supported by the Swiss National Science Foundation (Project 200020-117591), the Swiss Commission of Technology and Innovation (KTI/CTI, Project 9231.2 PFNM-NM), and the European Commission through the Human Potential Programme (Marie-Curie RTN Nanomatch, Grant No. MRTN-CT-2006-035884).

References

1 J. Rouquerol, D. Avnir, C. W. Fairbridge, D. H. Everett, J. H. Haynes, N. Pernicone, J. D. F. Ramsay, K. S. W. Sing and K. K. Unger, *Pure & Appl. Chem.*, 1994, **66**, 1739.

2 C. S. Cundy and P. A. Cox, *Microporous Mesoporous Mater.*, 2005, **82**, 1.

3 R. M. Barrer, *J. Chem. Soc.*, 1948, 127.

4 T. Yanagisawa, T. Shimizu, K. Kuroda and C. Kato, *Bull. Chem. Soc. Jpn.*, 1990, **63**, 988; C. T. Kresge, M. E. Leonowicz, W. J. Roth, J. C. Vartuli and J. S. Beck, *Nature*, 1992, **359**, 710; J. S. Beck, J. C. Vartuli, W. J. Roth, M. E. Leonowicz, C. T. Kresge, K. D. Schmitt, C. T.-W. Chu, D. H. Olson, E. W. Sheppard, S. B. McCullen, J. B. Higgins and J. L. Schlenker, *J. Am. Chem. Soc.*, 1992, **114**, 10834.

5 Y. Wan and D. Zhao, *Chem. Rev.*, 2007, **107**, 2821; V. Meynen, P. Cool and E. F. Vansant, *Microporous Mesoporous Mater.*, 2009, **125**, 170.

6 A. Taguchi and F. Schüth, *Microporous Mesoporous Mater.*, 2005, **77**, 1; J. H. Clark, D. J. Macquarrie and S. J. Tavener, *Dalton Trans.*, 2006, 4297.

7 M. Vallet-Regí, F. Balas and D. Arcos, *Angew. Chem. Int. Ed.*, 2007, **46**, 7548; I. I. Slowing, J. L. Vivero-Escoto, C.-W. Wu and V. S.-Y. Lin, *Adv. Drug Deliv. Rev.*, 2008, **60**, 1278.

8 H. Yoshitake, *New J. Chem.*, 2005, **29**, 1107.

9 G. E. Fryxell, S. V. Mattigod, Y. Lin, H. Wu, S. Fiskum, K. Parker, F. Zheng, W. Yantasee, T. S. Zemanian, R. S. Addleman, J. Liu, K. Kemner, S. Kelly and X. Feng, *J. Mater. Chem.*, 2007, **17**, 2863.

10 S. Huh, J. W. Wiench, B. G. Trewyn, S. Song, M. Pruski and V. S.-Y. Lin, *Chem. Commun.*, 2003, 2364; S. Huh, J. W. Wiench, J.-C. Yoo, M. Pruski and V. S.-Y. Lin, *Chem. Mater.*, 2003, **15**, 4247; S. Sadasivan, D. Khushalani and S. Mann, *J. Mater. Chem.*, 2003, **13**, 1023; J. L. Blin, C. Gérardin, L. Rodehüser, C. Selve and M. J. Stébé, *Chem. Mater.*, 2004, **16**, 5071; C. Yang, Y. Wang, B. Zibrowius and F. Schüth, *Phys. Chem. Chem. Phys.*, 2004, **6**, 2461; R. P. Hodgkins, A. E. Garcia-Bennett and P. A. Wright, *Microporous Mesoporous Mater.*, 2005, **79**, 241; K. Möller, J. Kobler and T. Bein, *J. Mater. Chem.*, 2007, **17**, 624; F. O. M. Gaslain, C. Delacôte, A. Walcarius and B. Lebeau, *J. Sol-Gel Sci. Technol.*, 2009, **49**, 112.

11 T. Asefa, C. Yoshina-Ishii, M. J. MacLachlan and G. A. Ozin, *J. Mater. Chem.*, 2000, **10**, 1751; B. Hatton, K. Landskron, W. Whitnall, D. Perovic and G. A. Ozin, *Acc. Chem. Res.*, 2005, **38**, 305; F. Hoffmann, M. Cornelius, J. Morell and M Fröba, *Angew. Chem. Int. Ed.*, 2006, **45**, 3216; T. Tani, N. Mizoshita and S. Inagaki, *J. Mater. Chem.*, 2009, **19**, 4451.

12 J. Chen, Q. Li, R. Xu and F. Xiao, *Angew. Chem. Int. Ed.*, 1995, **34**, 2694.

13 R. Anwander, I. Nagl, M. Widenmeyer, G. Engelhardt, O. Groeger, C. Palm and T. Röser, *J. Phys. Chem. B*, 2000, **104**, 3532.

14 K. Yamamoto and T. Tatsumi, *Microporous Mesoporous Mater.*, 2001, **44–45**, 459.

15 J. E. Lim, C. B. Shim, J. M. Kim, B. Y. Lee and J. E. Yie, *Angew. Chem. Int. Ed.*, 2004, **43**, 3839.

16 S. Angloher, J. Kecht and T. Bein, *Chem. Mater.*, 2007, **19**, 3568.

17 J. Kecht and T. Bein, *Langmuir*, 2008, **24**, 14209.

18 H. Ritter, M. Nieminen, M. Karppinen and D. Brühwiler, *Microporous Mesoporous Mater.*, 2009, **121**, 79.

19 Y. Inaki, Y. Kajita, H. Yoshida, K. Ito and T. Hattori, *Chem. Commun.*, 2001, 2358.

20 N. Gartmann, C. Schütze, H. Ritter and D. Brühwiler, *J. Phys. Chem. Lett.*, 2010, **1**, 379.

21 J. Liu, X. Feng, G. E. Fryxell, L.-Q. Wang, A. Y. Kim and M. Gong, *Adv. Mater.*, 1998, **10**, 161.

22 A. B. Bourlinos, T. Karakostas and D. Petridis, *J. Phys. Chem. B*, 2003, **107**, 920.

23 V. Antochshuk and M. Jaroniec, *Chem. Mater.*, 2000, **12**, 2496.

24 D. Das, J.-F. Lee and S. Cheng, *Chem. Commun.*, 2001, 2178.

25 V. Dufaud and M. E. Davis, *J. Am. Chem. Soc.*, 2003, **125**, 9403.

26 K. Y. Ho, G. McKay and K. L. Yeung, *Langmuir*, 2003, **19**, 3019.

27 E. J. Acosta, C. S. Carr, E. E. Simanek and D. F. Shantz, *Adv. Mater.*, 2004, **16**, 985; S. Yoo, J. D. Lunn, S. Gonzalez, J. A. Ristich, E. E. Simanek and D. F. Shantz, *Chem. Mater.*, 2006, **18**, 2935.

28 M. H. Lim and A. Stein, *Chem. Mater.*, 1999, **11**, 3285.

29 T. Yokoi, H. Yoshitake and T. Tatsumi, *J. Mater. Chem.*, 2004, **14**, 951.

30 K. K. Sharma, A. Anan, R. P. Buckley, W. Ouellette and T. Asefa, *J. Am. Chem. Soc.* 2008, **130**, 218.

31 H. Salmio and D. Brühwiler, *J. Phys. Chem. C*, 2007, **111**, 923.

32 N. Gartmann and D. Brühwiler, *Angew. Chem. Int. Ed.*, 2009, **48**, 6354.

33 M. W. McKittrick and C. W. Jones, *Chem. Mater.*, 2003, **15**, 1132.

34 J. C. Hicks and C. W. Jones, *Langmuir*, 2006, **22**, 2676; J. C. Hicks, R. Dabestani, A. C. Buchanan and C. W. Jones, *Chem. Mater.*, 2006, **18**, 5022.

35 M. Luechinger, R. Prins and G. D. Pirngruber, *Microporous Mesoporous Mater.*, 2005, **85**, 111.

36 S. Dai, M. C. Burleigh, Y. Shin, C. C. Morrow, C. E. Barnes and Z. Xue, *Angew. Chem. Int. Ed.*, 1999, **38**, 1235; J. D. Bass and A. Katz, *Chem. Mater.*, 2006, **18**, 1611.

37 E. L. Margelefsky, R. K. Zeidan and M. E. Davis, *Chem. Soc. Rev.*, 2008, **37**, 1118.

38 Y. Shin, J. Liu, L.-Q. Wang, Z. Nie, W. D. Samuels, G. E. Fryxell and G. J. Exarhos, *Angew. Chem. Int. Ed.*, 2000, **39**, 2702.

39 I. Slowing, B. G. Trewyn and V. S.-Y. Lin, *J. Am. Chem. Soc.*, 2006, **128**, 14792.

40 C.-P. Tsai, C.-Y. Chen, Y. Hung, F.-H. Chang and C.-Y. Mou, *J. Mater. Chem.*, 2009, **19**, 5737; J. M. Rosenholm, A. Meinander, E. Peuhu, R. Niemi, J. E. Eriksson, C. Sahlgren and M. Lindén, *ACS Nano*, 2009, **3**, 197.

41 D. S. Shephard, W. Zhou, T. Maschmeyer, J. M. Matters, C. L. Roper, S. Parsons, B. F. G. Johnson and M. J. Duer, *Angew. Chem. Int. Ed.*, 1998, **37**, 2719.

42 K. Cheng and C. C. Landry, *J. Am. Chem. Soc.*, 2007, **129**, 9674.

43 Y. Kievsky and I. Sokolov, *IEEE Trans. Nanotechnol.* 2005, **4**, 490.

44 A. Katiyar and N. G. Pinto, *Small*, 2006, **2**, 644; J. B. S. Ng, P. Kamali-Zare, M. Sörensen, H. Brismar, N. Hedin and L. Bergström, *Langmuir*, 2010, **26**, 466.

45 N. K. Mal, M. Fujiwara and Y. Tanaka, *Nature*, 2003, **421**, 350; N. K. Mal, M. Fujiwara, Y. Tanaka, T. Taguchi and M. Matsukata, *Chem. Mater.*, 2003, **15**, 3385; Q. Yang, S. Wang, P. Fan, L. Wang, Y. Di, K. Lin and F.-S. Xiao, *Chem. Mater.*, 2005, **17**, 5999.

46 D. Brühwiler, G. Calzaferri, T. Torres, J. H. Ramm, N. Gartmann, L.-Q. Dieu, I. Lopez-Duarte and M. V. Martinez-Diaz, *J. Mater. Chem.*, 2009, **19**, 8040.

47 T. D. Nguyen, Y. Liu, S. Saha, K. C.-F. Leung, J. F. Stoddart and J. I. Zink, *J. Am. Chem. Soc.* 2007, **129**, 626; M. Liong, S. Angelos, E. Choi, K. Patel, J. F. Stoddart and J. I. Zink, *J. Mater. Chem.*, 2009, **19**, 6251.

48 H. Ritter and D. Brühwiler, *J. Phys. Chem. C*, 2009, **113**, 10667.

49 J. Kecht, A. Schlossbauer and T. Bein, *Chem. Mater.*, 2008, **20**, 7207.

50 D. Zhao, J. Feng, Q. Huo, N. Melosh, G. H. Fredrickson, B. F. Chmelka and G. D. Stucky, *Science*, 1998, **279**, 548; D. Zhao, Q. Huo, J. Feng, B. F. Chmelka and G. D. Stucky, *J. Am. Chem. Soc.*, 1998, **120**, 6024.

51 M. Kruk, M. Jaroniec, C. H. Ko and R. Ryoo, *Chem. Mater.*, 2000, **12**, 1961; M. Impéror-Clerc, P. Davidson and A. Davidson, *J. Am. Chem. Soc.*, 2000, **122**, 11925; R. Ryoo, C. H. Ko, M. Kruk, V. Antochshuk and M. Jaroniec, *J. Phys. Chem. B*, 2000, **104**, 11465; A. Galarneau, H. Cambon, F. Di Renzo, R. Ryoo, M. Choi and F. Fajula, *New J. Chem.*, 2003, **27**, 73.

52 C.-M. Yang, H.-A. Lin, B. Zibrowius, B. Spliethoff, F. Schüth, S.-C. Liou, M.-W. Chu and C.-H. Chen, *Chem. Mater.*, 2007, **19**, 3205.

3. Publication B

A comparative study of the functionalization of mesoporous silica MCM-41 by deposition of 3-aminopropyltrimethoxysilane from toluene and from the vapor phase

Hanna Ritter[a], Minna Nieminen[b], Maarit Karppinen[b], Dominik Brühwiler[a,*]

[a] Institute of Inorganic Chemistry, University of Zurich, Winterthurerstrasse 190, CH-8057 Zurich, Switzerland

[b] Laboratory of Inorganic Chemistry, Department of Chemistry, Helsinki University of Technology, P.O. Box 6100, FI-02015 TKK, Finland

Microporous Mesoporous Mater. 121 (2009) 79 – 83

Abstract. The postsynthetic functionalization of mesoporous silica MCM-41 by vapor phase deposition of 3-aminopropyltrimethoxysilane is investigated as an alternative to the common practice of depositing from toluene. Particular emphasis is given to the possibility of eliminating the influence of trace water upon deposition from the vapor phase. The comparative study of samples prepared by different deposition methods requires identical degrees of functionalization. To obtain reliable information on the amount of surface-grafted aminopropyl groups, we have developed an analysis procedure based on the fluorogenic amine-derivatization reaction of fluorescamine.

B.1. Introduction

Aminopropyltrialkoxysilanes are among the most frequently used precursors for the modification of mesoporous silica surfaces, allowing subsequent coupling to a variety of functional groups, such as isothiocyanate or sulfonyl chloride.[1] Amino-functionalized mesoporous silica furthermore plays an important role in the development of materials for a wide range of potential applications, including adsorption of metal ions,[2] protein sequestration and release,[3] enzyme immobilization,[4] drug delivery,[5] and catalysis.[6] Despite considerable progress in the development of advanced methods for the one-pot synthesis of functionalized mesoporous silica,[7] approaches based on post-synthetic functionalization remain popular due to the fact that the separation of the silica synthesis and functionalization steps allows an independent and more straightforward control of pore size, periodicity, particle size, and particle morphology.

The reaction of surface silanol groups with aminopropylalkoxysilanes is usually conducted by refluxing in toluene. Due to the high accessibility of the sites on the external particle surface and on the pore surface close to the channel entrances, the distribution of anchored amino groups in the final product is typically inhomogeneous.[8] We have recently shown that aminopropylmonoalkoxysilanes produce a more homogeneous distribution than the corresponding trialkoxysilanes.[9] The presence of only one reactive group increases the mobility of the silane on the silica surface, while excluding the possibility of cross-linking.

It is difficult to avoid hydrolysis and cross-linking when depositing trialkoxy- or trichlorosilanes from a solvent. Even when working in dry solvents, trace water is efficiently adsorbed on the silica surface such that hydrolysis becomes possible.[10] It has been proposed that the employment of vapor phase deposition techniques might facilitate the elimination of silane cross-linking, thus minimizing clustering and multilayer formation.[11] In the case of mesoporous silica, this should ultimately lead to a more uniform distribution of the grafted moieties, resulting in a well-defined pore size of the functionalized material. In order to assess the validity of this hypothesis, we have in the present contribution investigated the postsynthetic functionalization of mesoporous silica MCM-41 with 3-aminopropyltrimethoxysilane (APTMS) by deposition from toluene and from the vapor phase. In the latter case, the atomic layer deposition (ALD) technique based on self-limiting surface reactions was employed, which is known to enable the deposition of vaporized precursor molecules in a highly reproducible and homogeneous manner.[11]

B.2. Experimental

B.2.1. Synthesis of MCM-41

As large batch sizes are required for comparative studies, we have used a scale-up friendly room temperature procedure based on the synthesis reported in Ref. 12. Briefly, 17.6 g of the structure directing agent CTAB (hexadecyltrimethylammonium bromide, Fluka, purum, ≥ 96 %) was dissolved under slight warming in a mixture of 416 mL of distilled H_2O and 192 mL of aqueous ammonia (25 % NH_3, Fluka). To this clear solution, 80 mL of TEOS (tetraethoxysilane, Fluka, puriss., ≥ 99 %) was slowly added under stirring. After further stirring for 3 h, the gel was aged at room temperature for 24 h in a closed container. The product was obtained by filtration, washed with copious amounts of distilled H_2O, and dried in air at room temperature. The structure directing agent was removed by first heating at 300 °C for 2 h and then calcining in air at 550 °C for 16 h. Heating rates of ~2 °C/min were used. The procedure yielded 19.3 g of calcined MCM-41.

B.2.2. Vapor phase deposition

Reactions were performed in an ALD reactor (F-120 ASM Microchemistry) at a pressure of 35–50 mbar. A 2.0 g sample of calcined MCM-41 was pretreated in the ALD reactor in nitrogen atmosphere at 180 °C for 3 h to remove physisorbed water.[13] An amount of 2.5 mL (14.2 mmol) of APTMS (Fluka, purum, ≥ 97 %) was subsequently vaporized at 100 °C and deposited onto the MCM-41 bed during 3 h at a selected reaction temperature in the range of 110–300 °C. Finally, physisorbed APTMS molecules were purged from the surface by flowing nitrogen for 2 h. Amino group analysis (see below) yielded a final amino loading of 1.2 mmol per gram of parent MCM-41. A further increase of the amount of vaporized APTMS did not lead to an increase in the final amino group content, indicating that the value of 1.2 mmol/g corresponds to the maximum loading which could be achieved by this deposition method.

B.2.3. Deposition from toluene

In a typical experiment, 0.5 g of calcined MCM-41 was pretreated at 180 °C for 2 h and dispersed in 30 mL of

dry toluene (Fluka, puriss., H_2O ≤ 50 ppm). After the addition of a calculated amount of APTMS (160 µL for the targeted functionalization degree of 1.2 mmol/g of parent MCM-41), the suspension was refluxed for 3 h. The functionalized product was recovered by filtration, washed with 100 mL of ethanol, and oven-dried at 80 °C for 1 h.

B.2.4. Amino group analysis

15 mg of amino-functionalized MCM-41 was stirred in 30 mL of a 0.02 M aqueous solution of NaOH until completely dissolved. 100 µL of this solution was transferred into a quartz cuvette and 2 mL of phosphate buffer (0.2 M, pH 8.0) was added. After the addition of 1 mL of fluorescamine (Sigma, > 97 %) solution (1 mM in acetone), the fluorescence spectrum was measured with a Perkin-Elmer LS50B spectrofluorometer by excitation at 366 nm. The emission intensity at 480 nm was taken as the datum point. A calibration line was prepared accordingly by using 100 µL aliquots of differently concentrated solutions of APTMS in 30 mL of 0.02 M aqueous NaOH (containing 15 mg of dissolved parent MCM-41).

B.2.5. Characterization

Nitrogen sorption isotherms were collected at 77 K using a Quantachrome NOVA 2200 surface area and pore size analyzer. Samples were vacuum-degassed at 80 °C for 5 h. The total surface area was calculated by the BET method,[14] whereas the external surface area and the primary mesopore volume (the volume of the uniform mesopores) were determined from the linear part of the α_S-plot (α_S > 1).[15] Mesopore size distributions were evaluated from the desorption branches of the nitrogen isotherms by means of the BJH method.[16] In order to obtain a more reliable estimate of the pore size of the parent MCM-41, the NLDFT method developed for silica exhibiting cylindrical pore geometry was also applied (NOVAWin2 software, Version 2.2, Quantachrome Instruments).[17] In this case, the adsorption branch was used for the calculations.[18] The total pore volume was calculated from the amount of nitrogen adsorbed at a relative pressure of 0.95. All samples exhibited type IV isotherms[19] and condensation in the primary mesopores was not accompanied by hysteresis. Diffuse reflectance infrared Fourier transform spectroscopy (DRIFTS) was performed using a Nicolet Magna IR 750 spectrometer equipped with a Spectra Tech diffuse reflectance accessory. Spectra were collected in the 400–4000 cm^{-1} range at a 2 cm^{-1} resolution over 64 scans. The spectrum obtained from a steel mirror was used as a background. Powder X-ray diffraction (XRD) measurements were performed on a STOE STADI P with CuKα_1 radiation, a 2θ step size of 0.1°, and a counting time of 30 s per step.

B.3. Results and discussion

B.3.1. Parent MCM-41

Fig. 1 shows the nitrogen sorption isotherms, pore size distribution (PSD), and XRD pattern of a typical mesoporous silica MCM-41 synthesized at room temperature. The four XRD peaks, which can be indexed on a hexagonal lattice (*hk*0 reflections only), are indicative of well ordered MCM-41 type materials.[20] Due to its narrow PSD and the fact that the material can be made available in relatively large batches without necessitating costly lab equipment, we have found this material to be ideal for comparative studies such as the present one.

The standard BJH analysis is known to underestimate the absolute pore size.[18] A more reliable estimate is obtained by the DFT method[17] (d_{DFT} = 3.54 nm vs. d_{BJH} = 2.47 nm, Fig. 1) or by using the geometrical approach proposed by Kruk et al.[21] Based on the latter formalism, our parent MCM-41 is characterized by an average pore diameter of 3.41 nm and an average wall thickness of 0.93 nm. Typical values for BET surface area and total pore volume are 910 m^2/g and 0.71 cm^3/g (with a primary mesopore volume of 0.58 cm^3/g), respectively. The external surface area accounts for ~12 % of the total surface area. The particle size ranges from 0.5 to 2 µm with irregular morphology.

B.3.2. Amino group analysis

In order to compare different deposition techniques, it is essential to work under conditions which yield a defined degree of functionalization. This calls for a method that is capable of providing accurate information on the amount of grafted amino groups. Analytical data obtained with ninhydrin (Kaiser test[22]) were found to be unsatisfactory and difficult to reproduce. Samples with identical amounts of amino groups but different distributions of grafting sites (external surface vs. pore surface) produced different results in terms of the actual amount of detected amino groups. We believe that the reason for this discrepancy is the diminished accessibility of the sites deep inside the pores. Problems of this kind are common for analytical meth-

ods employing mesoporous silica with intact pore structure. Methods based on the elemental analysis of amino groups obviously do not suffer from this drawback, however, sufficient precision can only be expected for samples featuring high grafting densities.[23] We have, therefore, developed a method that affords a reliable determination of the amount of grafted amino groups independent of the pore size and grafting site distribution, while covering a wide range of functionalization degrees. The key reaction of this method is based on the fluorometric quantitation of primary amines with fluorescamine.[24] To eliminate the effect of the grafting site distribution, the mesoporous framework is decomposed prior to the addition of fluorescamine. Reaction of the intrinsically non-fluorescent fluorescamine with the now fully accessible primary amines yields a fluorescent derivative. The fluorescence intensity is then used to determine the initial amino group content by means of a calibration line (Fig. 2).

B.3.3. Deposition temperature

Previous studies on the vapor phase deposition of 3-aminopropyltriethoxysilane (APTES) on silica have shown that the deposition temperature is an important parameter in terms of determining the binding mode of the silane to the silica surface, revealing that unwanted secondary reactions involving the formation of Si–N bonds occur at temperatures higher than 150 °C.[25] We observed a similar effect in our preliminary vapor phase depositions of APTMS on MCM-41 carried out at selected temperatures (see Fig. 3 for the DRIFT spectra of these samples). Stretching frequencies of the primary amino groups are observed at 3305 and 3373 cm^{-1}. Additional bands at 3437 and 3470 cm^{-1} assigned to Si–NH–C moieties develop at deposition temperatures higher than 150 °C. The contribution of Si–NH–C binding modes is significant already at 250 °C. In order to avoid the reaction of amino groups with surface silanol groups or strained siloxane bridges, as well as with the methoxysilyl groups of other APTMS molecules, the deposition temperature was fixed at 150 °C for the final experiments. Under these conditions, the reaction of methanol, which is formed upon grafting of APTMS, with surface silanol groups is unlikely.[11,26] No secondary reactions involving the formation of Si–N bonds occurred upon deposition of APTMS from toluene under reflux.

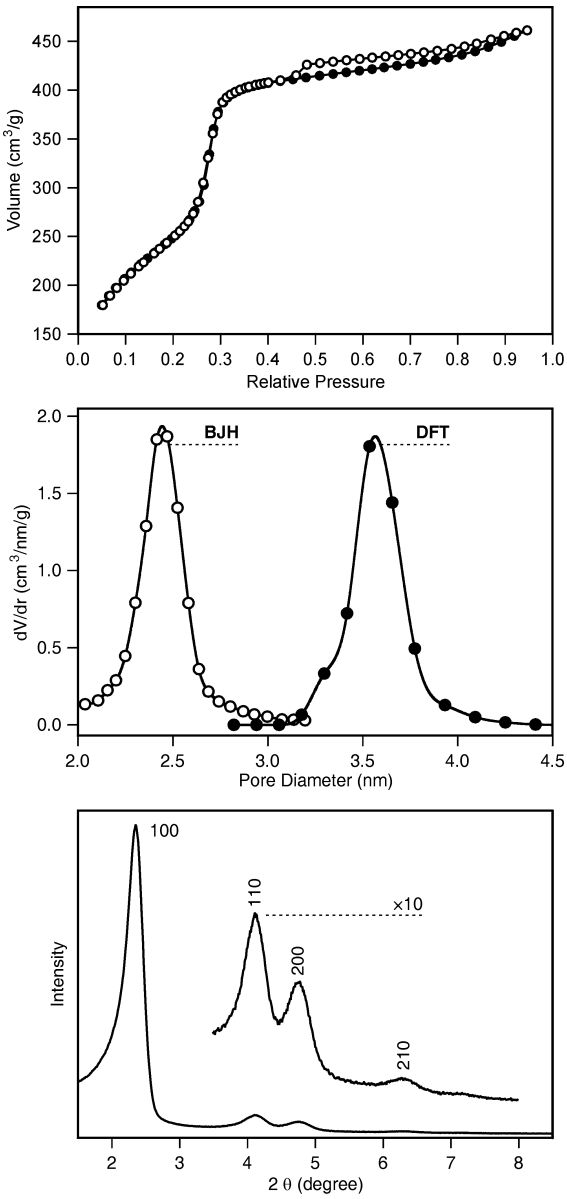

Fig. 1. Characterization data of calcined mesoporous silica MCM-41 synthesized at room temperature. Top: Nitrogen adsorption (solid circles) and desorption (empty circles) isotherm. The high pressure hysteresis loop is due to secondary mesoporosity. Middle: Pore size distributions calculated by BJH and DFT methods. Bottom: XRD pattern.

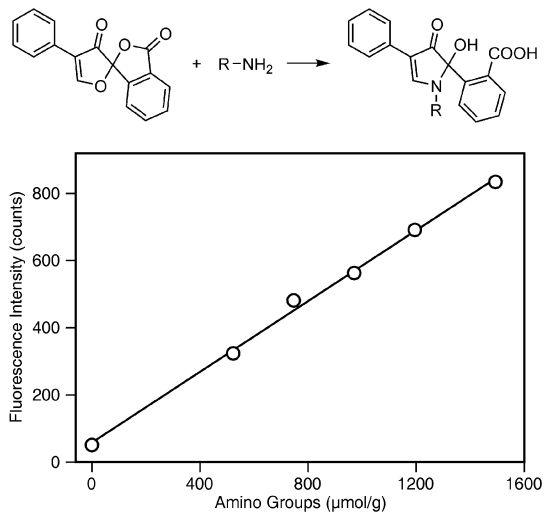

Fig. 2. Fluorogenic amine-derivatization reaction of fluorescamine and a corresponding calibration line prepared with APTMS.

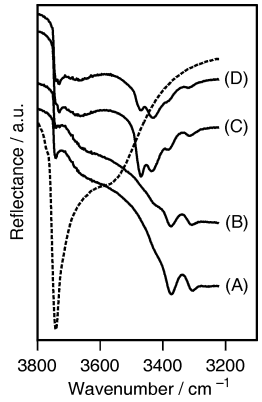

Fig. 3. DRIFT spectra of MCM-41 after vapor phase deposition of APTMS at 110 °C (A), 150 °C (B), 250 °C (C), and 300 °C (D). The dashed curve represents the spectrum of calcined MCM-41 before APTMS deposition.

B.3.4. Comparison of the deposition methods

It is worth mentioning at this point that the investigated samples, assuming a homogeneous distribution and an initial BET surface area of 910 m^2/g, were synthesized with a surface coverage of 0.79 $–NH_2$ per nm^2 (corresponding to a functionalization degree of 1.2 mmol/g). Fig. 4A compares the PSDs of MCM-41 after deposition of APTMS from the vapor phase (sample Vap-APTMS) and from toluene (sample Tol-APTMS), the former producing a material with a narrower PSD (full width at half maximum FWHM = 0.30 nm, compared to FWHM = 0.42 nm for Tol-APTMS). To remove potential APTMS oligomers, we have repeated the deposition from toluene using freshly vacuum distilled APTMS (sample Tol-APTMS-d). As can be seen from Fig. 4B, the PSD of the resulting functionalized MCM-41 is slightly more uniform and narrower (FWHM = 0.37 nm) compared to the sample prepared without distillation.

The differences between the PSD of Vap-APTMS and Tol-APTMS seem minor at first sight. However, it should be noted that the samples contain the same amount of surface-grafted amino groups. The differences can therefore be attributed to different surface distributions of the functional groups, as we have recently shown for amino-functionalized samples prepared with various aminosilane precursors.[9] Interestingly, there is a considerable contribution of relatively large pores to the PSD of the samples grafted in toluene. This is most likely a consequence of pore blocking due to cross-linking of APTMS. If clustering of APTMS occurs close to the entrance of a given pore, diffusion of additional APTMS molecules into this pore is hindered, leaving part of the pore surface unmodified. In the PSD derived from nitrogen sorption, such a partially blocked pore is consequently recorded with a comparatively large pore diameter.

Upon deposition from the vapor phase, the primary mesopore volume decreased by 0.31 cm^3/g, whereas a less pronounced reduction of 0.25 cm^3/g was observed after deposition from toluene (1.2 mmol/g of grafted amino groups for each sample). The accompanying changes of the BET surface area (–419 m^2/g for Vap-APTMS, –306 m^2/g for Tol-APTMS, and –287 m^2/g for Tol-APTMS-d) support the conclusion that different distributions of grafted amino groups were obtained. A recent study by Asefa and co-workers[6b] has shown that the deposition of APTMS from toluene produced aggregated grafted groups, while Tatsumi and co-workers[8a] found that the surface-bound amino groups were concentrated near the pore entrances and on the external surface. Our results indicate that the tendency towards aggregation and external surface grafting is less pronounced in the vapor phase deposition method. In this context, it is worth mentioning that toluene is not an ideal solvent for producing site isolation of grafted amino groups. Less aggregation and increased site isolation has for example been obtained upon deposition from alcohols[6b] or THF.[9]

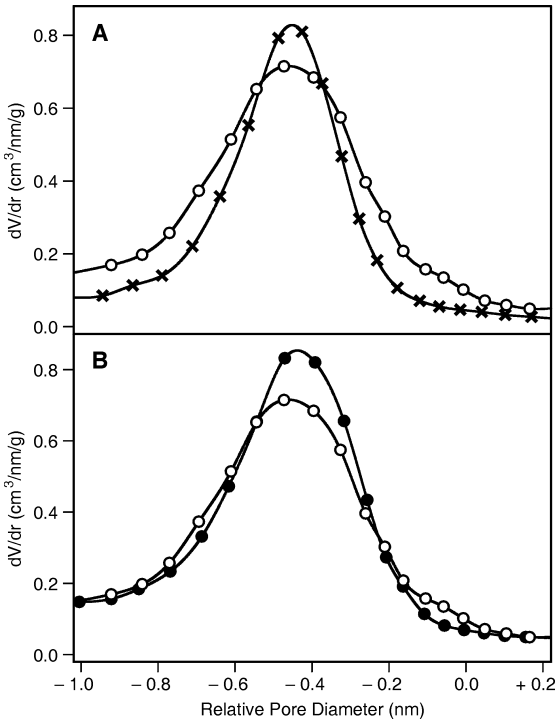

Fig. 4. A: PSD of MCM-41 after deposition of APTMS from the vapor phase (Vap-APTMS, crosses) compared to the PSD of MCM-41 after deposition of APTMS from toluene (Tol-APTMS, empty circles). **B**: PSD of MCM-41 after deposition of APTMS from toluene without (Tol-APTMS, empty circles) and with prior vacuum distillation of APTMS (Tol-APTMS-d, solid circles). Pore diameters are given relative to the average pore diameter of the parent MCM-41. Amino group contents are 1.2 mmol/g for each sample.

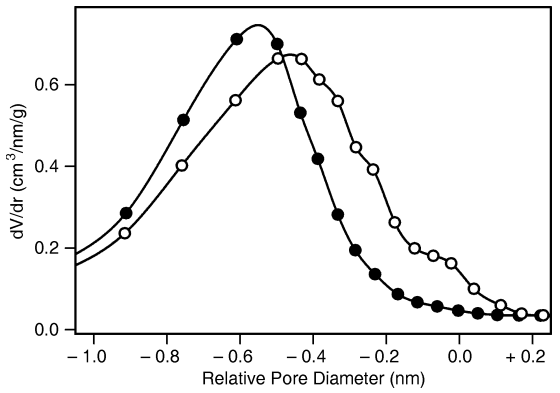

Fig. 5. PSD of MCM-41 after deposition of APTMS from toluene containing approximately 400 ppm of H_2O (empty circles) and less than 50 ppm of H_2O (solid circles). Pore diameters are given relative to the average pore diameter of the parent MCM-41. Amino group contents are 1.2 mmol/g.

B.3.5. Influence of trace water

To investigate the influence of water on the degree of pore blocking, we conducted the following experiment: A 0.5 g sample of calcined MCM-41 was dispersed in 30 mL of toluene containing different amounts of H_2O. After short ultrasonication and additional stirring for 15 min, 160 µL of APTMS was added. Reaction, recovery, and analysis were performed as described above. The resulting PSDs of two representative samples are shown in Fig. 5. While the water content seems to have no effect on the yield of grafted amino groups, the PSDs are clearly different. Pore blocking is obviously strongly promoted by the presence of trace water. This is in agreement with an earlier study by Walcarius et al.[27] observing slower proton and metal uptake of aminopropyl-grafted MCM-41 prepared by postsynthetic functionalization with APTES (deposited from toluene) in the presence of trace water. The effect shown in Fig. 5 occurs already at relatively low water contents. Under our experimental conditions, a water content of 400 ppm results in a H_2O/APTMS ratio of ~0.6. Assuming complete surface adsorption of H_2O with an area of 0.1 nm^2 per molecule, a water content of 400 ppm corresponds to only about 1/13 of a monolayer. We can therefore conclude that the presence of small quantities of water in toluene considerably affects the grafting behavior of APTMS by promoting cross-linking of silane molecules. To obtain a narrow PSD and a high fraction of pore surface grafting, it is therefore crucial to work with dry toluene.

B.4. Conclusion

Functionalization of mesoporous silica by vapor phase deposition of APTMS is a viable alternative to reactions carried out in solvents. The use of vapor phase deposition eliminates trace water-induced silane cross-linking and subsequent pore blocking. As the separation of APTMS monomers from potential oligomers present in liquid APTMS is an inherent property of the vapor phase deposition method, distillation of APTMS prior to the grafting reaction is not necessary. Furthermore, the vapor phase deposition method is of interest for economical and ecological reasons, especially concerning large scale syntheses, as it avoids the use of (dry) solvents. In future work, the vapor phase deposition of APTMS needs to be examined in terms of its potential to provide site isolation, specifically in relation to optimized solvent based deposition techniques.[28] Such comparative studies

are particularly meaningful when samples of similar functionalization degree are examined. This requires an analysis method which yields accurate and reproducible results for a wide range of grafting densities independent of the distribution of the functional groups on the mesoporous silica surface. The determination of the amino groups by reaction with fluorescamine after decomposition of the mesoporous framework provides a sound basis for further research in this field.

Acknowledgments. Financial support was provided by the European Commission through the Human Potential Program (Marie-Curie RTN Nanomatch, Grant No. MRTN-CT-2006-035884) and by the Swiss National Science Foundation (Project 200020-117591).

References

1. (a) Y. Rohlfing, D. Wöhrle, J. Rathouský, A. Zukal, M. Wark, Stud. Surf. Sci. Catal. 142 (2002) 1067; (b) V. Antochshuk, O. Olkhovyk, M. Jaroniec, I.-S. Park, R. Ryoo, Langmuir 19 (2003) 3031; (c) E. J. Acosta, C. S. Carr, E. E. Simanek, D. F. Shantz, Adv. Mater. 16 (2004) 985; (d) I. Slowing, B. G. Trewyn, V. S.-Y. Lin, J. Am. Chem. Soc. 128 (2006) 14792.
2. A. M. Liu, K. Hidajat, S. Kawi, D. Y. Zhao, Chem. Commun. (2000) 1145.
3. Y.-J. Han, G. D. Stucky, A. Butler, J. Am. Chem. Soc. 121 (1999) 9897.
4. J. F. Díaz, K. J. Balkus, J. Mol. Catal. B: Enzym. 2 (1996) 115.
5. F. Balas, M. Manzano, P. Horcajada, M. Vallet-Regi, J. Am. Chem. Soc. 128 (2006) 8116.
6. (a) K. K. Sharma, T. Asefa, Angew. Chem. Int. Ed. 46 (2007) 2879; (b) K. K. Sharma, A. Anan, R. P. Buckley, W. Ouellette, T. Asefa, J. Am. Chem. Soc. 130 (2008) 218; (c) X. Wang, K. S. K. Lin, J. C. C. Chan, S. Cheng, J. Phys. Chem. B 109 (2005) 1763; (d) D. J. Macquarrie, D. B. Jackson, Chem. Commun. (1997) 1781; (e) A. Cauvel, G. Renard, D. Brunel, J. Org. Chem. 62 (1997) 749; (f) D. Brunel, Microporous Mesoporous Mater. 27 (1999) 329.
7. F. Hoffmann, M. Cornelius, J. Morell, M. Fröba, Angew. Chem. Int. Ed. 45 (2006) 3216.
8. (a) T. Yokoi, H. Yoshitake, T. Tatsumi, J. Mater. Chem. 14 (2004) 951; (b) M. H. Lim, A. Stein, Chem. Mater. 11 (1999) 3285.
9. H. Salmio, D. Brühwiler, J. Phys. Chem. C 111 (2007) 923.
10. (a) C. P. Tripp, M. L. Hair, Langmuir 11 (1995) 1215; (b) S. M. Kanan, W. T. Y. Tze, C. P. Tripp, Langmuir 18 (2002) 6623.
11. S. Ek, E. I. Iiskola, L. Niinistö, Langmuir 19 (2003) 3461.
12. D. Brühwiler, H. Frei, J. Phys. Chem. B 107 (2003) 8547.
13. S. Ek, A. Root, M. Peussa, L. Niinistö, Thermochim. Acta 379 (2001) 201.
14. S. Brunauer, P. H. Emmett, E. Teller, J. Am. Chem. Soc. 60 (1938) 309.
15. M. Kruk, M. Jaroniec, R. Ryoo, J. M. Kim, Microporous Mater. 12 (1997) 93.
16. E. P. Barrett, L. G. Joyner, P. P. Halenda, J. Am. Chem. Soc. 73 (1951) 373.
17. P. I. Ravikovitch, S. C. O. Domhnaill, A. V. Neimark, F. Schüth, K. K. Unger, Langmuir 11 (1995) 4765.
18. P. I. Ravikovitch, A. V. Neimark, Colloid Surf. A: Physicochem. Eng. Aspect 187-188 (2001) 11.
19. K. S. W. Sing, D. H. Everett, R. A. W. Haul, L. Moscou, R. A. Pierotti, J. Rouquerol, T. Siemieniewska, Pure Appl. Chem. 57 (1985) 603.
20. (a) C. T. Kresge, M. E. Leonowicz, W. J. Roth, J. C. Vartuli, J. S. Beck, Nature 359 (1992) 710; (b) J. S. Beck, J. C. Vartuli, W. J. Roth, M. E. Leonowicz, C. T. Kresge, K. D. Schmitt, C. T.-W. Chu, D. H. Olson, E. W. Sheppard, S. B. McCullen, J. B. Higgins, J. L. Schlenker, J. Am. Chem. Soc. 114 (1992) 10834.
21. M. Kruk, M. Jaroniec, A. Sayari, J. Phys. Chem. B 101 (1997) 583.
22. E. Kaiser, R. L. Colescott, C. D. Bossinger, P. I. Cook, Anal. Biochem. 34 (1970) 595.
23. S. Ek, E. I. Iiskola, L. Niinistö, J. Vaittinen, T. T. Pakkanen, J. Keränen, A. Auroux, Langmuir 19 (2003) 10601.
24. (a) M. Weigele, S. L. DeBernardo, J. P. Tengi, W. Leimgruber, J. Am. Chem. Soc. 94 (1972) 5927; (b) S. Udenfriend, S. Stein, P. Böhlen, W. Dairman, W. Leimgruber, M. Weigele, Science 178 (1972) 871.
25. S. Ek, E. I. Iiskola, L. Niinistö, T. T. Pakkanen, A. Root, Chem. Commun. (2003) 2032.
26. E. A. Wovchko, J. C. Camp, J. A. Glass, J. T. Yates, Langmuir 11 (1995) 2592.
27. A. Walcarius, M. Etienne, B. Lebeau, Chem. Mater. 15 (2003) 2161.
28. (a) K. K. Sharma, R. P. Buckley, T. Asefa, Langmuir 24 (2008) 14306; (b) J. C. Hicks, R. Dabestani, A. C. Buchanan III, C. W. Jones, Chem. Mater. 18 (2006) 5022; (c) J. C. Hicks, C. W. Jones, Langmuir 22 (2006) 2676; (d) M. W. McKittrick, C. W. Jones, Chem. Mater. 15 (2003) 1132.

4. Publication C

Distribution of amino groups on a mesoporous silica surface after submonolayer deposition of aminopropylsilanes from an anhydrous liquid phase

Hanna Salmio and Dominik Brühwiler*

Institute of Inorganic Chemistry, University of Zurich, Winterthurerstrasse 190, 8057 Zurich, Switzerland

J. Phys. Chem. C 111 (2007) 923 – 929

Abstract. The reaction of mesoporous silica MCM-41 with various aminopropylsilanes was investigated. The distribution of grafted amino groups after submonolayer deposition from anhydrous toluene was probed by fluorescein labeling in conjunction with photoluminescence spectroscopy and pore size analysis. Monoalkoxysilanes generally distributed more uniformly than monopodal and dipodal trialkoxysilanes. The outcome of the grafting reaction additionally depended on the nature of the amino group. Secondary amines grafted more efficiently than their primary analogues. Moreover, it was found that the polarity of the solvent strongly affects the distribution of the amino groups in the case of strongly interacting aminopropylsilanes.

C.1. Introduction

Since the discovery of the remarkable features of the M41S mesoporous silica family,[1] considerable effort has been directed toward functionalization of these materials. Catalysis,[2] optical sensing,[3] photonics,[4] adsorption,[5] and drug delivery[6] are fields in which functionalized mesoporous silica opens new prospects. For many potential applications based on mesoporous silica, a homogeneous distribution of site-isolated functional groups is desired. From this perspective, co-condensation would be the method of choice, as postsynthetic modification often leads to preferential functionalization of the most readily accessible sites (external surface and pore entrances).[7] However, postsynthetic grafting provides various advantages: Through passivation of the external surface, the internal surface can be selectively functionalized (and vice versa).[8] High densities of functional groups can be achieved without unfavorable effects on the stability and the periodic ordering of the mesoporous silica framework. Site isolation can be obtained even for dense grafting by a molecular spacer approach.[9] Control of the pore size and particle morphology is straightforward, and hierarchic structures can be produced by postsynthetic molecular imprinting.[10]

Aminopropylsilanes are among the most widely used precursors for the modification of silica surfaces. In anhydrous media, reaction with surface hydroxyl groups proceeds via exchange of the silane alkoxy group (usually methoxy or ethoxy) for the silanol oxygen with concurrent loss of the corresponding alcohol. It is shown in this study, that the choice of the aminopropylsilane precursor is essential for controlling the amount, the distribution, and the stability of the grafted aminopropyl moieties on the mesoporous silica surface.

C.2. Experimental Section

Synthesis of MCM-41. Purely siliceous mesoporous silica MCM-41 was synthesized as follows:[11] A 2.20-g amount of CTAB (hexadecyltrimethylammonium bromide, Fluka) was dissolved under slight warming in a mixture of 52 mL of distilled H_2O and 24 mL of aqueous ammonia (28 %, Fluka). After the solution had been cooled to room temperature, 10 mL of TEOS (tetraethoxysilane, Fluka) was slowly added under stirring to the clear solution, and the resulting gel was further stirred for 3 h at room temperature. The mixture was then transferred to a Teflon-lined autoclave and heated at 110 °C for 48 h. The product was obtained by filtration, washed with copious amounts of distilled H_2O (at least 800 mL) and dried in air at room temperature. The template was removed by first heating at 300 °C for 2 h and then calcination in air at 550 °C for 16 h. Heating rates of approximately 2 °C/min were applied.

Grafting of Aminopropylsilanes. (3-Aminopropyl)dimethylmethoxysilane (APDMMS, Acros), (3-aminopropyl)diisopropylethoxysilane (APDIPES, Gelest), (3-aminopropyl)trimethoxysilane (APTMS, Fluka), [3-(methylamino)propyl]trimethoxysilane (MAPTMS, Gelest), (3-aminopropyl)triethoxysilane (APTES, Fluka), bis(trimethoxysilylpropyl)amine (BTMSPA, Fluka), bis(triethoxysilylpropyl)amine (BTESPA, Gelest), and [3-(methylamino)propyl]methyldimethoxysilane (MAPMDMS, Gelest) were used as received. Polymerization of the liquid aminopropylsilanes is initiated by the presence of water, leading to hydrolysis and cross-linking. All aminopropylsilanes were therefore kept under inert atmosphere. Experiments with freshly vacuum-distilled aminopropylsilanes showed that polymerization was not a concern under our storage conditions. In a typical grafting experiment, an amount of 500 mg of calcined MCM-41 was oven-dried at 80 °C for 1 h and dispersed in 30 mL of dry toluene (puriss., $H_2O \leq 0.005$ %). After the addition of a calculated amount of a specific aminopropylsilane, the suspension was heated to 125 °C over a period of 15 min, refluxed for 3 h, and subsequently allowed to cool for 30 min. The functionalized product was recovered by filtration, washed with 100 mL of ethanol, and oven-dried at 80 °C for 1 h.

Fluorescein Labeling. A 250-mg amount of amino-functionalized mesoporous silica was dispersed in 25 mL of absolute ethanol containing an at least 1.5-fold excess of FITC (fluorescein 5-isothiocyanate, isomer I, Fluka). The amount of FITC was calculated assuming quantitative grafting of the respective aminopropylsilane (15 mg of FITC for a batch prepared with a theoretical aminopropylsilane loading of 100 µmol per gram of MCM-41). After the suspension had been stirred in the dark at room temperature for 24 h, the colored product was recovered by filtration and washed with 50 mL of ethanol. Prolongation of the FITC coupling time did not lead to further fluorescein binding, indicating that complete labeling of the amino groups was obtained after 24 h. To ensure removal of unreacted FITC, the product was redis-

persed in 50 mL of ethanol and stirred for 15 min at room temperature. After filtration and washing with 50 mL of ethanol, the product was finally oven-dried at 80 °C for 1 h. To determine the amount of coupled fluorescein, a weighed quantity (typically 15–30 mg) of the product was dispersed in 25 mL of a 0.2 M aqueous solution of NaOH and stirred for 3 h at room temperature. After dissolution of the silica, the clear solution was diluted with water, and the fluorescein concentration was determined by measuring the absorption spectrum (λ = 490 nm, ε = 88000 $Lmol^{-1}cm^{-1}$).

Characterization. Powder X-ray diffraction (XRD) measurements were performed on a Siemens D-500 diffractometer with Cu Kα radiation, a 2θ step size of 0.05°, and a counting time of 3 s per step. Photoluminescence (PL) spectra were recorded with a Perkin Elmer LS50B spectrofluorometer equipped with a front surface accessory for the measurement of powdered samples. Nitrogen sorption isotherms were collected at 77 K using a Quantachrome NOVA2200 surface area and pore size analyzer. Samples were vacuum-degassed at 353 K for 5 h. The total surface area was obtained using the standard BET method for adsorption data in a relative pressure range from 0.05 to 0.20.[12] The total pore volume was estimated from the amount of nitrogen adsorbed at a relative pressure of 0.95. The primary mesopore volume, V_p (the volume of the uniform mesopores), was determined by the α_S-plot method.[13] Mesopore size distributions were evaluated from the desorption branches of the nitrogen isotherms using the BJH method and are plotted relative to the maximum pore diameter of the corresponding parent MCM-41.[14] All samples exhibited type IV isotherms, and condensation in primary mesopores was not accompanied by hysteresis. It should be noted that the standard BJH method underestimates the absolute pore size. To obtain a more reliable estimate, the method proposed by Kruk et al. was applied:[15]

$$w = 1.2125 \cdot d_{100}\left(\frac{\rho V_p}{1+\rho V_p}\right)^{1/2} \quad (1)$$

The lattice spacing d_{100} was obtained from XRD data. The density of the pore walls, ρ, was set to be equal to the density of amorphous silica (2.2 g/cm^3).

C.3. Results and Discussion

Blank Test. The investigation of submonolayer coverages requires the evaluation of subtle variations in the pore size distribution (PSD). It is therefore crucial to analyze the pore size changes under the applied reaction conditions without the addition of any aminopropylsilane. We observed a minor shift of the PSD to smaller pore size up to the point of FITC coupling (refluxing in toluene, washing, drying), and a similar shift under FITC coupling conditions (stirring for 24 h in an ethanolic solution of FITC, washing, drying). No fluorescein was detected in the samples at this stage, indicating that binding of FITC occurs only on aminopropylsilane-modified MCM-41. The total shift of the PSD of the blank samples was typically 0.04 nm (diameter), with the distribution retaining its width and symmetrical shape. This minor change can be attributed to a slight esterification of the surface during the washing treatments in ethanol and subsequent drying.[16]

General Tendencies. We have investigated the reaction of various commercial aminopropylsilanes with calcined MCM-41 in toluene. Structures and abbreviations are given in Figure 1. The pore diameter of our parent MCM-41 was calculated to be 3.6 nm using eq 1, resulting in a pore wall thickness of 0.8 nm. BET surface areas varied slightly from batch to batch in the range of 810–890 m^2/g. An external surface area (secondary mesopores and macropores) of approximately 65 m^2/g was estimated from the high pressure part of the α_S-plots. Although the preparation of MCM-41 proved to be well reproducible in terms of the PSD, comparative studies were only conducted on samples synthesized from the same batch of parent MCM-41.

It is instructive to investigate the grafting behavior of a monomethoxysilane, a trimethoxysilane, and a dipodal silane featuring two trimethoxysilyl groups. Taking into account a surface silanol concentration of approximately 3 mmol/g,[17] a charge of 100 µmol of aminopropylsilane per gram of MCM-41 ensures an excess of silanol groups. Figure 2 shows the PSDs of MCM-41 after reaction with 100 µmol/g APDMMS, APTMS, or BTMSPA. A shift toward smaller pore size is observed for all samples. However, the extent of this shift strongly depends on the type of silane. For the dipodal silane BTMSPA, the PSD maximum is only slightly shifted relative to that of the parent MCM-41. Shifts of similar magnitude were observed for the blank samples. The distinctive tail extending toward

smaller pore size suggests a nonuniform distribution of the amine sites. The monomethoxysilane APDMMS, on the other hand, grafts more uniformly to the mesoporous silica surface, resulting in a larger shift and a symmetrical PSD. The APTMS-grafted sample features properties lying between those two extremes.

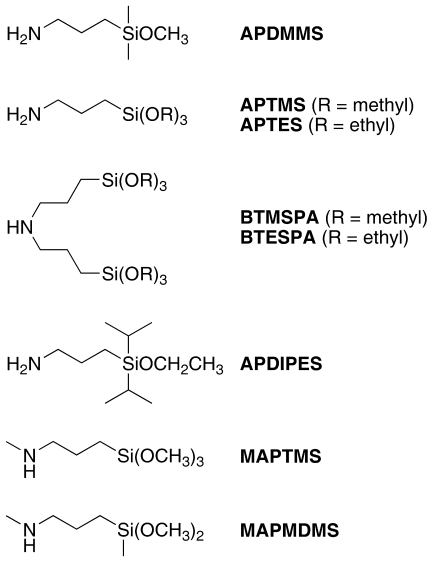

Figure 1. Structures and abbreviations of aminopropylsilanes.

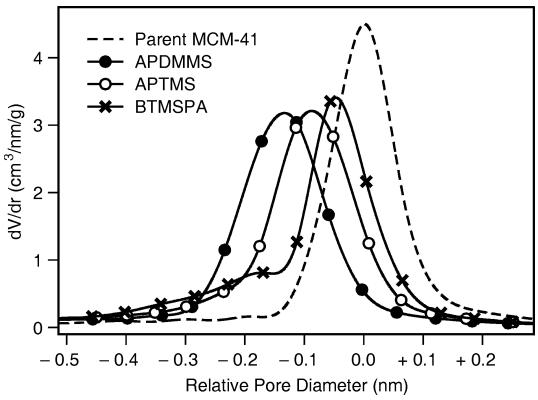

Figure 2. PSDs of MCM-41 after reaction with 100 µmol/g of APDMMS, APTMS, or BTMSPA.

FITC is one of the most popular labeling reagents, forming a thiourea upon reaction with an amine (see Figure 3). Apart from being used to modify proteins, peptides, synthetic oligonucleotides, and other biomolecules, FITC has recently been applied in the preparation of mesoporous thin films with pH-sensing abilities.[18] Coupling of FITC is expected to amplify the differences between the APDMMS-, APTMS-, and BTMSPA-grafted samples. The reaction of FITC with amino groups located on the internal surface changes the PSD, whereas the coupling of FITC to amino groups anchored to the external surface has no effect in this regard. In the case of the APDMMS-grafted sample, the PSD is further shifted to smaller pore size. This is in contrast to the BTMSPA-grafted sample, for which a significantly smaller shift of the maximum pore diameter is observed (see Figure 4). Shifts of this magnitude also occurred for blank samples. The PSD of the BTMSPA-grafted material remains unsymmetrical, with uneven contributions of smaller pore sizes. Again, intermediate behavior was found for APTMS. The relatively large pore size shift of the APDMMS-grafted sample is surprising considering the fluorescein contents, which amounted to 20 µmol/g for APDMMS, 36 µmol/g for APTMS, and 52 µmol/g for BTMSPA. These results clearly indicate that BTMSPA preferably binds to sites on or close to the external surface. The distinct tail of the PSD suggests clustering of BTMSPA at pore entrance sites. For APTMS and APDMMS, increased grafting in the pores is observed, with APDMMS yielding the most homogeneous distribution of grafting sites.

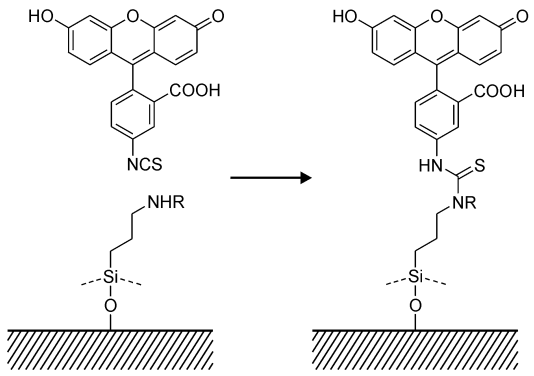

Figure 3. Coupling of FITC to surface-bound primary (R=H) and secondary aminopropylsilanes. The number of possible siloxane bonds depends on the type of silane.

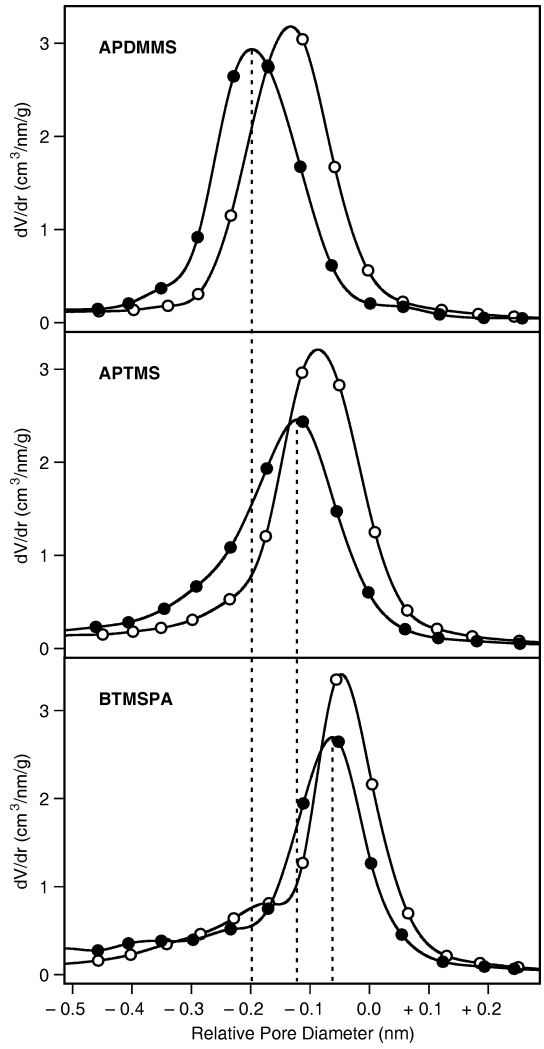

Figure 4. PSDs of APDMMS-, APTMS-, and BTMSPA-grafted samples before (open circles) and after (filled circles) FITC coupling. Fluorescein contents are 20 µmol/g (APDMMS), 36 µmol/g (APTMS), and 52 µmol/g (BTMSPA). The samples were prepared from the same batch of MCM-41 by reaction with 100 µmol/g of the corresponding aminopropylsilane.

Table 1. N_2 Adsorption Data after FITC Coupling.[a,b]

silane	V_{tot} (cm^3/g)	V_p (cm^3/g)	S_{BET} (m^2/g)
BTMSPA	0.635	0.567	780
APTMS	0.625	0.557	770
APDMMS	0.601	0.536	746

[a] V_{tot} = total pore volume, V_p = primary mesopore volume, S_{BET} = BET surface.
[b] Fluorescein content = (20.0 ± 1.0) µmol/g.

Further information on the distribution of the amine sites was obtained by examining the photoluminescence of the FITC-coupled samples. To allow for comparison of the luminescence intensities, samples containing equal amounts of fluorescein were synthesized by adjusting the aminopropylsilane concentration in the reaction mixtures. The resulting luminescence spectra and PSDs are shown in Figure 5. Additional nitrogen adsorption analysis data are compiled in Table 1. At this point, it is helpful to briefly discuss the pH dependence of the fluorescein luminescence in solution.[19] Three different fluorescence spectra are typically observed in H_2O when the pH is varied. The cation emission (λ_{max} = 475 nm) appears only in strongly acidic solution. The state of ionization of the carboxyl group (pK_a = 4.4) has no influence on the fluorescence spectrum. As a consequence, the spectrum of the monoanion (pK_a = 6.7) is essentially the same as that of the neutral molecule. The emission maximum is found between 510 and 520 nm, with prominent shoulders around 555 and 595 nm. The fluorescence spectrum of the dianion features the same maximum, but is narrowed compared to the spectrum of the monoanionic and neutral species. Furthermore, the dianion exhibits a higher fluorescence yield (0.93)[20] than the neutral/monoanionic species (0.20–0.35).[19] Inspecting the luminescence spectra in Figure 5, we can immediately rule out the presence of cationic fluorescein species. To ensure that the intensity differences of the samples are not due to varying ratios of neutral, monoanionic, and dianionic fluorescein, PL measurements were performed on toluene suspensions that were titrated with triethylamine until maximum luminescence intensity was observed. Addition of triethylamine leads to narrowing of the luminescence bands, yielding samples containing exclusively dianionic fluorescein. For both dry samples and toluene/triethylamine suspensions, the luminescence intensity increases in the order BTMSPA < APTMS < APDMMS. These remarkably different luminescence intensities are attributed to various degrees of self-quenching. The self-quenching of fluorescein is due to resonance energy transfer between fluorescein molecules, with a Förster distance of 42 Å.[21] Efficient self-quenching therefore implies short distances between the grafted amine sites. Because the investigated coverages lie well within the submonolayer regime, a diminished luminescence intensity suggests clustering of amine sites.

Methoxy vs. Ethoxy. Methoxysilanes are generally more reactive than ethoxysilanes.[22] On the other hand, ethoxysilanes are more bulky than the corresponding methoxysilanes. The comparison of the grafting behavior of BTMSPA/BTESPA and APTMS/APTES revealed only minor differences. The yields of FITC coupling were similar for the BTMSPA/BTESPA and APTMS/APTES pairs. However, the tendency to graft to the internal surface was slightly more pronounced in the case of the ethoxysilanes. This difference, although reproducible, is admittedly subtle and much smaller than what we observed when comparing APDMMS, APTMS, and BTMSPA. After FITC coupling, the materials grafted with APTES and BTESPA also showed slightly stronger luminescence compared to the materials grafted with the corresponding methoxysilanes, suggesting a lower degree of clustering.

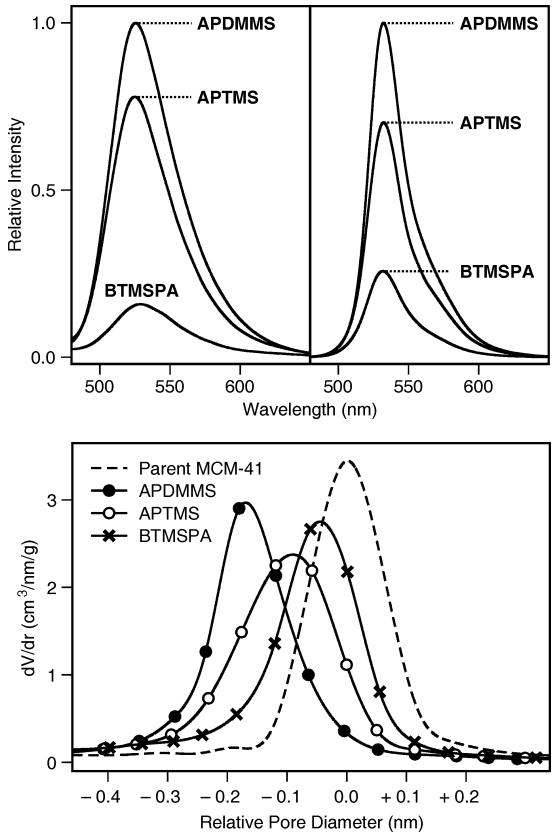

Figure 5. Top: PL spectra of FITC-coupled samples grafted with different aminopropylsilane precursors (excitation at 450 nm). The spectra in the left panel were measured on dry samples. The right panel shows the corresponding spectra measured on equally concentrated suspensions in toluene/triethylamine. Bottom: PSDs of the same samples. Fluorescein contents are (20.0 ± 1.0) µmol/g.

APDMMS vs. APDIPES. Our results so far indicate that, in terms of obtaining a homogeneous distribution of grafting sites, APDMMS is superior to APTMS and BTMSPA. On the negative side, APDMMS-grafted samples suffer from reduced stability against solvolysis.[23] Stirring a APDMMS-grafted sample (30 mg, 20 µmol/g of coupled fluorescein) in 0.2 M sodium phosphate buffer (20 mL, pH 7.5) for 24 h at room temperature resulted in a loss of (53 ± 3) % of fluorescein. This problem is solved by replacing APDMMS with APDIPES. APDIPES-grafted samples feature pore sizes resembling those of the corresponding APDMMS grafted samples (see Figure 6). Taking into account the similar luminescence properties of FITC-coupled APDMMS and APDIPES samples, we can conclude that an equally homogeneous distribution of amine sites is obtained. Moreover, APDIPES-grafted samples are as stable as their APTMS counterparts. Under the hydrolysis conditions described above, leaching of only (18 ± 3) % of fluorescein was observed. Apparently, the bulky isopropyl groups protect the single siloxane link. This is in agreement with the improved low-pH hydrolytic stability of common bonded-phase silicas treated with monofunctional silanes containing bulky groups at the silicon atom.[24] It is interesting to note that, despite being more bulky than APTMS, APDIPES is able to bind to less accessible sites on the internal surface and thus produces a more uniform distribution of grafted amino groups.

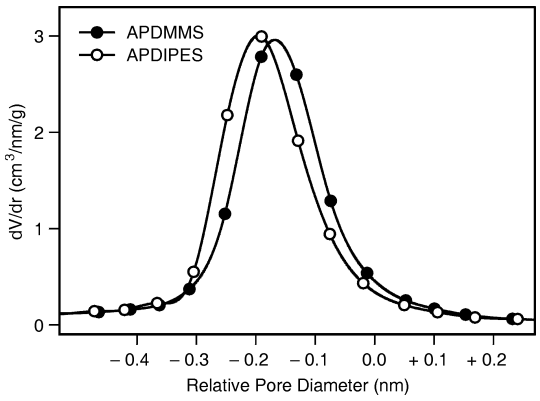

Figure 6. PSDs of APDMMS- and APDIPES-grafted samples after FITC coupling. Fluorescein contents are (20.0 ± 1.0) µmol/g.

Primary vs. Secondary Amines. To study the role of the amino functionality in the grafting process, it is instructive to compare the reactivities of APTMS and MAPTMS. Despite the fact that both molecules are trimethoxysilanes, the grafting of MAPTMS was found to be considerably more efficient. The reaction of 50 µmol of the respective silane with 500 mg of MCM-41 and subsequent FITC coupling resulted in fluorescein contents of 52 µmol/g for MAPTMS and 36 µmol/g for APTMS. In terms of grafting efficiency, MAPTMS apparently resembles BTMSPA, emphasizing the important role of the amino functionality in the self-catalyzed grafting process.[25] However, when compared to BTMSPA, MAPTMS showed a higher tendency to graft to the internal surface, although not surpassing that of the APTMS-grafted samples of the same loading (see Figure 7). The luminescence properties of MAPTMS-grafted samples after FITC coupling are comparable to those of APTMS-grafted samples of the same fluorescein content. Under identical reaction conditions, the degree of clustering therefore seems to be determined mainly by the number of methoxy groups per molecule.

Grafting Mechanism. Apparently, there is a correlation between the tendency to yield a homogeneous distribution of grafting sites and the number of alkoxy groups (methoxy or ethoxy) per aminopropylsilane molecule. Furthermore, secondary amines give higher grafting yields (estimated from the amount of coupled fluorescein) than primary amines. In view of these results, the following mechanism for the reaction of aminopropylsilanes with mesoporous silica is proposed: In a first step, the aminopropylsilane is adsorbed on the mesoporous silica surface, forming hydrogen bonds with surface silanol groups. The amino groups thereby function as hydrogen-bond acceptors. There is evidence in the case of APTES that this first step reaches an equilibrium within 1 min.[25] This initial adsorption concerns accessible silanols, that is, sites on the external surface and sites close to the pore entrances. Note that we have used maximum aminopropylsilane amounts of 100 µmol per gram of MCM-41. Adsorption of a submonolayer is therefore possible even without access to the entire MCM-41 surface. BTMSPA and BTESPA exhibit the strongest interactions with the surface, because their secondary amines are better acceptors for hydrogen bonds than the primary amines of APTMS, APTES, APDMMS, and APDIPES. Additionally, six alkoxy groups per molecule are available for siloxane bond formation. On the other hand, the monoalkoxysilanes (APDMMS and APDIPES) are more mobile because of a weaker interaction with the surface and are thus able to reach less accessible sites located in the pores. Furthermore, silanes with more than one alkoxy group per molecule have the tendency to form aminopropylsilane islands. This contributes to a nonuniform distribution of the grafting sites, manifesting itself in low luminescence intensities after FITC coupling.

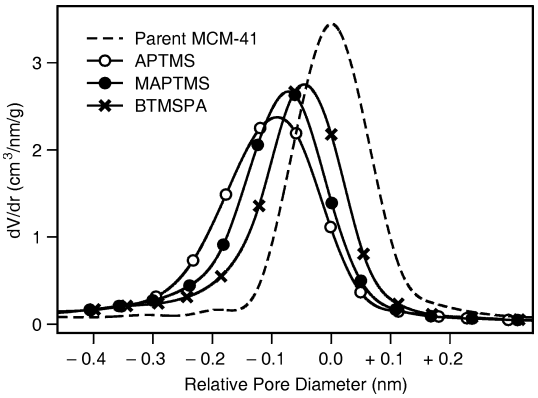

Figure 7. PSDs of APTMS-, MAPTMS-, and BTMSPA-grafted samples after FITC coupling. Fluorescein contents are (20.0 ± 1.0) µmol/g.

The mechanism leading to the formation of aminopropylsilane islands is subject to speculation. The activation of surface silanols by hydrogen-bonded aminopropylsilanes might advance the formation of islands,[25] especially in regions of high silanol density on the rough MCM-41 surface.[26] Cross-linking between aminopropylsilane molecules is also expected to promote clustering. However, this process requires the presence of water for the preceding hydrolysis step. The actual amount of water on a silica surface depends on the thermal pretreatment.[27] To provide reproducible conditions, all of our calcined MCM-41 materials were treated at 80 °C before use. This temperature was chosen because of its compatibility with organic modifications introduced by postsynthetic grafting or co-condensation. Total release of physisorbed water usually requires temperatures above 100 °C.[27] The solvent is another potential source of trace water, regardless of careful dehydration treatments. This problem is associated with the fact that

silica behaves as a drying agent, adsorbing even minute quantities of water.[28] We can therefore conclude that traces of water are present and that cross-linking most likely contributes to the clustering of the dipodal and (to a smaller extent) the monopodal trialkoxysilanes. Previous studies on the reaction of APTES with silica gel have shown that hydrolysis and cross-linking take place on the silica surface, that is, after the initial adsorption of the silane monomers.[29] Small amounts of water thereby not only promote cross-linking of adsorbed aminopropylsilanes, but also enhance the reactivity of the silanes toward surface silylation.[30] To minimize cross-linking, complete dehydration of MCM-41 would be necessary. This requires temperatures at which dehydroxylation occurs simultaneously[27] and decomposition of organic functionalities introduced into the MCM-41 framework becomes an issue. As will be shown below, clustering of aminopropylsilanes on the MCM-41 surface can be conveniently minimized by increasing the polarity of the solvent used for the grafting reaction.

The relatively large size of the BTMSPA and BTESPA molecules might contribute to a nonuniform distribution by partial pore blocking. Considering the initial pore diameter of 3.6 nm and the low aminopropylsilane loadings, we expect that such effects are of minor importance under our conditions. This is supported by the observation that APDIPES distributes more uniformly than the less bulky APTMS. Further evidence that the grafting reactions are not governed by pore blocking was obtained by substituting MCM-41 with fumed silica, which is essentially nonporous but still features a large surface area (200 m^2/g). Grafting of BTMSPA, APTMS, and APDMMS to fumed silica and subsequent FITC coupling resulted in fluorescein contents comparable to those of analogous samples based on MCM-41. More importantly, the luminescence properties of the FITC-coupled fumed silica samples resembled those of the corresponding MCM-41 materials.

Prediction of Grafting Behavior. Our interpretation of the results can be tested by attempting to predict the grafting behavior of MAPMDMS (see Figure 1). Because it is a secondary amine, we anticipate a high grafting yield. In accordance with our expectation, fluorescein contents similar to those of MAPTMS-grafted samples were observed. The presence of only two methoxy groups should lead to an increased mobility of MAPMDMS when compared to MAPTMS. The PSDs of the FITC-coupled samples indeed support this hypothesis (see Figure 8). However, when compared to APTMS, the ability of MAPMDMS to graft to internal surface sites is less pronounced, emphasizing the strong interaction of the secondary amino group with the silica surface. Clustering of the MAPMDMS molecules is less likely than clustering of the trimethoxysilanes APTMS and MAPTMS. The strong luminescence of FITC-coupled samples grafted with MAPMDMS effectively provides evidence for a low tendency to form islands (see Figure 8). Comparison of the relative luminescence intensities in Figures 5 and 8 indicates similarities between MAPMDMS- and APDMMS-grafted samples. We can therefore conclude that clustering in MAPMDMS-grafted samples is virtually absent.

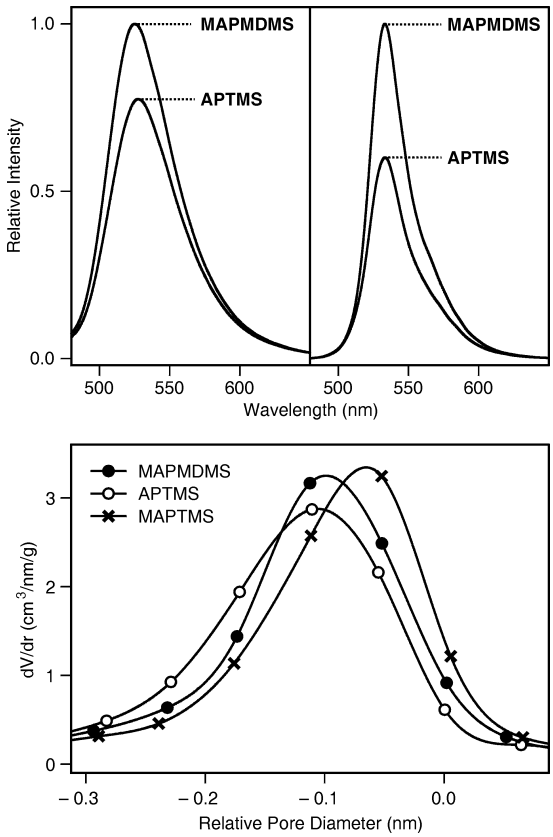

Figure 8. Top: PL spectra of FITC-coupled samples grafted with APTMS and MAPMDMS (excitation at 450 nm). The spectra in the left panel were measured on dry samples. The right panel shows the corresponding spectra measured on equally concentrated suspensions in toluene/triethylamine. PSDs are given in the bottom panel. Fluorescein contents are (20.0 ± 1.0) µmol/g.

Solvent Effects. As a further implication of the proposed grafting mechanism, it is to be expected that the use of a more polar solvent than toluene will generate a more uniform distribution of grafting sites by increasing the mobility of the aminopropylsilane molecules. We have tested this hypothesis by comparing the grafting behaviors of BTMSPA in toluene and THF. The results are shown in Figure 9. Whereas the grafting yield remains essentially unchanged when THF is used as the solvent, the strong luminescence of the FITC-coupled BTMSPA/THF sample suggests decreased clustering. Furthermore, the PSD of the BTMSPA/THF sample is shifted to smaller pore size by a considerable amount, comparable to that observed for APTMS/toluene samples.

The inhibition of clustering in polar solvents entails important consequences. Site-isolated grafting is favored, and the formation of multilayer coverages becomes less likely in the case of excess silane. The latter was observed for the room temperature functionalization of an external zeolite surface with APTES.[31] For a given aminopropylsilane, it is therefore possible to tune the distribution of the grafting sites and the degree of silane clustering by choosing an appropriate solvent. Such solvent effects are less distinct in the case of weakly interacting aminopropylsilanes, that is, primary aminopropylsilanes with small numbers of alkoxy groups.

C.4. Conclusions

The structure of an aminopropylsilane determines its grafting behavior. Grafting yields strongly depend on the type of amine, whereas the uniformity of the amine site distribution on the mesoporous silica surface is mainly determined by the number of alkoxy groups. Consequently, the brightness of FITC-coupled samples can be maximized by employing monoalkoxysilanes, instead of the widely used trialkoxysilanes, as postsynthetically applied surface anchors. Dipodal trialkoxysilanes react preferably with sites on the external surface and at the pore entrances and are therefore candidates for selective external surface modification. Finally, the polarity of the solvent is essential for controlling the grafting site distribution and the degree of clustering. Clustering is minimized with increasing polarity, whereas the distribution becomes more uniform as the aminopropylsilane molecules are able to reach less accessible sites on the internal surface. Means to control the distribution of grafting sites on mesoporous silica are essential for a variety of potential applications. Optical sensing and cell marking applications rely on a high brightness of the luminescent silica particles, thus requiring site-isolated chromophores.[18,32] On the other hand, the accumulation of grafted molecules on the external surface and at the pore entrances is of interest for the design of advanced drug-delivery systems.[6c]

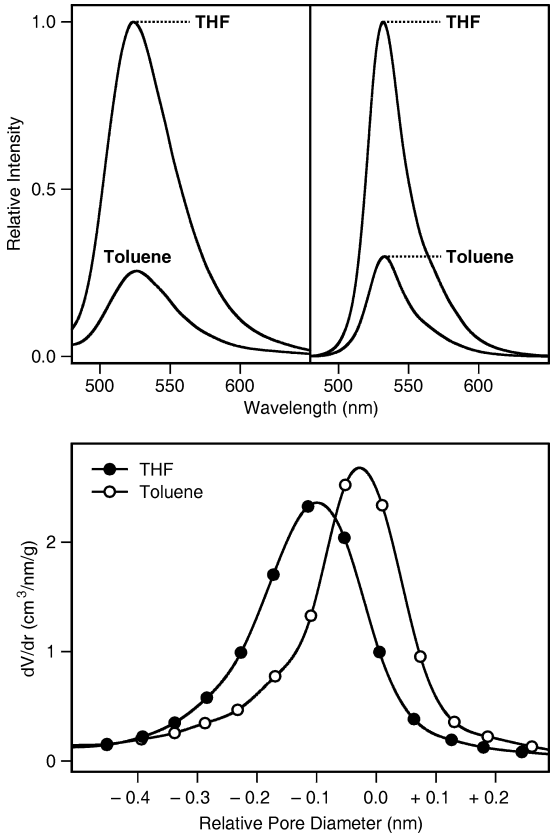

Figure 9. Top: PL spectra of FITC-coupled samples grafted with BTMSPA in THF and toluene, respectively (excitation at 450 nm). The spectra in the left panel were measured on dry samples. The right panel shows the corresponding spectra measured on equally concentrated suspensions in toluene/triethylamine. PSDs are given in the bottom panel. Fluorescein contents are (20.0 ± 1.0) μmol/g.

Acknowledgment. Financial support was provided by the Swiss National Science Foundation (Project 200021-109185).

References

(1) Beck, J. S.; Vartuli, J. C.; Roth, W. J.; Leonowicz, M. E.; Kresge, C. T.; Schmitt, K. D.; Chu, C. T. W.; Olson, D. H.; Sheppard, E. W.; McCullen, S. B.; Higgins, J. B.; Schlenker, J. L. *J. Am. Chem. Soc.* **1992**, *114*, 10834.

(2) (a) Taguchi, A.; Schüth, F. *Microporous Mesoporous Mater.* **2005**, *77*, 1. (b) De Vos, D. E.; Dams, M.; Sels, B. F.; Jacobs, P. A. *Chem. Rev.* **2002**, *102*, 3615.

(3) Wark, M.; Rohlfing, Y.; Altindag, Y.; Wellmann, H. *Phys. Chem. Chem. Phys.* **2003**, *5*, 5188.

(4) Scott, B. J.; Wirnsberger, G.; Stucky, G. D. *Chem. Mater.* **2001**, *13*, 3140.

(5) (a) Yoshitake, H.; Yokoi, T.; Tatsumi, T. *Chem. Mater.* **2002**, *14*, 4603. (b) Liu, J.; Feng, X.; Fryxell, G. E.; Wang, L.-Q.; Kim, A. Y.; Gong, M. *Adv. Mater.* **1998**, *10*, 161.

(6) (a) Lai, C.-Y.; Trewyn, B. G.; Jeftinija, D. M.; Jeftinija, K.; Xu, S.; Jeftinija, S.; Lin, V. S.-Y. *J. Am. Chem. Soc.* **2003**, *125*, 4451. (b) Muñoz, B.; Rámila, A.; Pérez-Pariente, J.; Diaz, I.; Vallet-Regi, M. *Chem. Mater.* **2003**, *15*, 500. (c) Mal, N. K.; Fujiwara, M.; Tanaka, Y. *Nature* **2003**, *421*, 350.

(7) (a) Yokoi, T.; Yoshitake, H.; Tatsumi, T. *J. Mater. Chem.* **2004**, *14*, 951. (b) Lim, M. H.; Stein, A. *Chem. Mater.* **1999**, *11*, 3285. (c) Singh, U. G.; Williams, R. T.; Hallam, K. R.; Allen, G. C. *J. Solid State Chem.* **2005**, *178*, 3405.

(8) Shephard, D. S.; Zhou, W.; Maschmeyer, T.; Matters, J. M.; Roper, C. L.; Parsons, S.; Johnson, B. F. G.; Duer, M. J. *Angew. Chem. Int. Ed.* **1998**, *37*, 2719.

(9) Hicks, J. C.; Jones, C. W. *Langmuir* **2006**, *22*, 2676.

(10) Shin, Y.; Liu, J.; Wang, L.-Q.; Nie, Z.; Samuels, W. D.; Fryxell, G. E.; Exarhos, G. J. *Angew. Chem. Int. Ed.* **2000**, *39*, 2702.

(11) Brühwiler, D.; Frei, H. *J. Phys. Chem. B* **2003**, *107*, 8547.

(12) Brunauer, S.; Emmett, P. H.; Teller, E. *J. Am. Chem. Soc.* **1938**, *60*, 309.

(13) Kruk, M.; Jaroniec, M.; Ryoo, R.; Kim, J. M. *Microporous Mater.* **1997**, *12*, 93.

(14) Barrett, E. P.; Joyner, L. G.; Halenda, P. P. *J. Am. Chem. Soc.* **1951**, *73*, 373.

(15) Kruk, M.; Jaroniec, M.; Sayari, A. *J. Phys. Chem. B* **1997**, *101*, 583.

(16) Kimura, T.; Kuroda, K.; Sugahara, Y.; Kuroda, K. *J. Porous Mater.* **1998**, *5*, 127.

(17) Zhao, X. S.; Lu, G. Q.; Whittaker, A. K.; Millar, G. J.; Zhu, H. Y. *J. Phys. Chem. B* **1997**, *101*, 6525.

(18) Wirnsberger, G.; Scott, B. J.; Stucky, G. D. *Chem. Commun.* **2001**, 119.

(19) Martin, M. M.; Lindqvist, L. *J. Lumin.* **1975**, *10*, 381.

(20) Weber, G.; Teale, F. W. J. *Trans. Faraday Soc.* **1958**, *54*, 640.

(21) Kawski, A. *Photochem. Photobiol.* **1983**, *38*, 487.

(22) Brand, M.; Frings, A.; Jenkner, P.; Lehnert, R.; Metternich, H. J.; Monkiewicz, J.; Schram, J. *Z. Naturforsch., B: Chem. Sci.* **1999**, *54*, 155.

(23) Waddell, T. G.; Leyden, D. E.; DeBello, M. T. *J. Am. Chem. Soc.* **1981**, *103*, 5303.

(24) Kirkland, J. J.; Glajch, J. L.; Farlee, R. D. *Anal. Chem.* **1989**, *61*, 2.

(25) Vrancken, K. C.; Possemiers, K.; van der Voort, P.; Vansant, E. F. *Colloids Surf. A* **1995**, *98*, 235.

(26) Sonwane, C. G.; Jones, C. W.; Ludovice, P. J. *J. Phys. Chem. B* **2005**, *109*, 23395.

(27) Ek, S.; Root, A.; Peussa, M.; Niinistö, L. *Thermochim. Acta* **2001**, *379*, 201.

(28) Kanan, S. M.; Tze, W. T. Y.; Tripp, C. P. *Langmuir* **2002**, *18*, 6623.

(29) Vrancken, K. C.; van der Voort, P.; Gillis-D'Hamers, I.; Vansant, E. F.; Grobet, P. *J. Chem. Soc. Faraday Trans.* **1992**, *88*, 3197.

(30) Caravajal, G. S.; Leyden, D. E.; Quinting, G. R.; Maciel, G. E. *Anal. Chem.* **1988**, *60*, 1776.

(31) Brühwiler, D.; Calzaferri, G. *C. R. Chim.* **2005**, *8*, 391.

(32) Lin, Y.-S.; Tsai, C.-P.; Huang, H.-Y.; Kuo, C.-T.; Hung, Y.; Huang, D.-M.; Chen, Y.-C.; Mou, C.-Y. *Chem. Mater.* **2005**, *17*, 4570.

5. Publication D

Accessibility of amino groups in postsynthetically modified mesoporous silica

Hanna Ritter and Dominik Brühwiler*

Institute of Inorganic Chemistry, University of Zurich, Winterthurerstrasse 190, 8057 Zurich, Switzerland

J. Phys. Chem. C 113 (2009) 10667 – 10674

Abstract. The accessibility of amino groups in postsynthetically functionalized mesoporous silica MCM-41, MCM-48, and SBA-15 is investigated by reaction with fluorescein isothiocyanate (FITC). The quantitative analysis of the surface-grafted amino groups in relation to the amount of coupled FITC over a wide range of loadings affords information about potential pore blocking. In the pore diameter domain of 3 – 4 nm, the actual pore size of materials with a one-dimensional channel system (MCM-41) strongly affects the FITC coupling yield and the distribution of the anchored fluorescein moieties. In the case of SBA-15 (7.6 nm pore diameter), the accessibility of the grafted amino groups is similar to what is expected for a material with a completely open surface. However, grafting in the intrawall micropores of SBA-15 leads to a substantial fraction of inaccessible amino groups. As a direct consequence of short channel lengths and large external surface area, excellent accessibility is also observed for nanometer-sized MCM-41 (3.2 nm pore diameter).

D.1. Introduction

Grafting of a functional group and subsequent coupling of an organic moiety exhibiting the desired property (such as luminescence, sensing, metal coordination) is a popular method for the modification of mesoporous silicas.[1-4] Postsynthetic functionalization techniques are preferably employed when the molecule to be introduced is not sufficiently stable under the conditions of the mesoporous silica synthesis, therefore excluding approaches based on co-condensation, or when a narrow pore size distribution (PSD) is required. The latter is typically more difficult to obtain by means of co-condensation, especially when high functionalization degrees are desired. A recent study by Rosenholm and Lindén compares the accessibility of amino groups in functionalized SBA-15 prepared by co-condensation, postsynthetic grafting with various amino-silanes, and surface polymerization of a polyethyleneimine, with the important result that the postsynthetic functionalization techniques are superior to co-condensation in terms of producing a large amount of accessible amino groups.[5]

The accessibility of the binding sites is the key to uniform postsynthetic surface functionalization. Depending on the relation between the pore diameter of the mesoporous material and the size of the moiety to be grafted, steric hindrance can limit the access to sites deep inside the pores. To evaluate to what extent such pore blocking effects depend on the pore diameter and the dimensionality of the channel system, we have investigated the reaction of fluorescein isothiocyanate (FITC) with amino-functionalized mesoporous silica MCM-41 (one-dimensional channel system),[6,7] MCM-48 (three-dimensional channel system),[6,7] and SBA-15 (one-dimensional channel system, larger pore size than MCM-41, microporous channel walls).[8,9] FITC coupling yields, which are obtained as a result of the combination of a fluorometric quantitation of the grafted amino groups[10] and a UV-Vis spectroscopic detection of the coupled FITC,[11] afford information about the accessibility. The accessibility of functional groups on the surface of mesoporous silicas is not only essential for further functionalization by coupling reactions, but also for potential applications such as catalysis[12,13] and adsorption-based separation.[14-19]

D.2. Experimental Section

D.2.1. Synthesis of Mesoporous Silicas

MCM-41(16) was prepared according to ref 20. Briefly, 2.20 g of hexadecyltrimethylammonium bromide (CTAB, Fluka) was dissolved under slight warming (approximately 35 °C) in a mixture of 52 mL of H_2O and 24 mL of aq ammonia (28 %, Fluka). An amount of 10 mL of tetraethoxysilane (TEOS, Fluka) was slowly added under stirring, and the resulting gel was further stirred for 3 h at room temperature. The mixture was transferred to a Teflon-lined autoclave and heated at 110 °C for 48 h. The product was obtained by filtration, washed with at least 800 mL of H_2O, and dried overnight in air at room temperature. The structure directing agent (SDA) was removed by first heating at 300 °C for 2 h and subsequent calcination in air at 550 °C for 16 h. Heating rates of 2 °C/min were applied. The X-ray diffraction (XRD) pattern was in agreement with the pattern reported in ref 20. MCM-41(12) was prepared accordingly, using 1.86 g of dodecyltrimethylammonium bromide (Fluka) instead of CTAB. The use of a SDA with a shorter alkyl chain reduces the pore size and shifts the XRD pattern toward larger angles (Figure 1).

MCM-48 was synthesized following a previously reported procedure.[21] An amount of 8.80 g of CTAB was dissolved under slight warming (approximately 35 °C) in 80 mL of H_2O. After the addition of 10 mL of 2 M aq NaOH, 10 mL of TEOS was added dropwise under stirring. After further stirring for 30 min, the mixture was transferred to a Teflon-lined autoclave and heated at 100 °C for 72 h. The product was recovered by filtration, washed with at least 1 L of H_2O, and oven-dried overnight at 80 °C. The SDA was removed by first heating at 300 °C for 2 h and subsequent calcination in air at 550 °C for 8 h. Heating rates of 2 °C/min were applied.

SBA-15 was prepared according to ref 9. Briefly, 2.20 g of Pluronic P123 ($EO_{20}PO_{70}EO_{20}$, M_{av} = 5800, Aldrich) was dissolved in a mixture of 49 mL of H_2O and 31 mL of 4 M aq HCl. To this clear solution, 5 mL of TEOS was slowly added under stirring. After further stirring for 20 h at approximately 35 °C, the mixture was transferred to a Teflon-lined autoclave and heated at 100 °C for 24 h. The product was obtained by filtration and washed with at least 1 L of H_2O. After drying the material overnight in air at room temperature, the SDA was removed by heating in air at 500 °C for 16 h. A heating rate of 1 °C/min was applied.

Nanoparticles of MCM-41 (nano-MCM-41) were synthesized as follows:[22] First, a clear solution of 2.60 g of hexadecyltrimethylammonium chloride (Fluka) and 2.00 g of Pluronic F-127 (Sigma) in 30 mL of 0.25 M aq HCl was prepared. After the dropwise addition of

3.7 mL of TEOS, the mixture was stirred for 20 h at room temperature. Finally, 3.7 mL of aq ammonia (28 %, Fluka) was added and the resulting gel was aged without stirring for 24 h. The product was oven-dried at 70 °C for 72 h and subsequently calcined at 600 °C for 3 h with a heating rate of 3 °C/min.

Fumed silica (Sigma, 14 nm primary particle size) was used as received.

D.2.2. Reaction with APTMS

For the functionalization with 3-aminopropyltrimethoxysilane (APTMS, Fluka), 500 mg of fumed silica, or calcined mesoporous silica was dispersed in 30 mL of dry toluene (Fluka, puriss., $H_2O \leq 0.005$ %). After the addition of a calculated amount of APTMS (between 0.05 and 1.20 mmol, taking into account the surface area of the employed silica), the suspension was refluxed for 3 h. The functionalized product was recovered by filtration, washed with 100 mL of ethanol, and cured at 80 °C for 1 h. Amino group analysis (Part D.2.4.) showed that within the error margin of the method, grafting of APTMS was quantitative in the above mentioned range. Samples with low amino content are denoted by A-*x*, where *x* identifies the type of silica. Samples with intermediate and high amino content are identified by B-*x* and C-*x*, respectively. Three independent syntheses were carried out for each data point.

To ensure reproducible and comparable conditions, all of our calcined mesoporous silica materials as well as fumed silica were treated for 1 h at 80 °C before use. This temperature was chosen because of its compatibility with potential organic modifications. It should be noted that the total release of physisorbed water usually requires temperatures above 100 °C. Such temperatures are, however, often not applicable when systems with multiple functional groups are desired, as this typically requires consecutive modification steps, such as co-condensation and subsequent post-synthetic grafting. Experiments conducted with MCM-41(16) dried at 180 °C produced results that were consistent with those obtained for samples dried at 80 °C.

D.2.3. FITC Coupling

Labeling with fluorescein 5-isothiocyanate (FITC, Fluka) was carried out according to ref 11. A calculated amount of FITC (1.5-fold excess relative to the amount of grafted amino groups) was dissolved in 25 mL of absolute ethanol. After the addition of 250 mg of amino-functionalized silica, the suspension was stirred for 24 h at room temperature. The yellow product was recovered by filtration and washed with 50 mL of ethanol. After redispersion in 50 mL of fresh ethanol and stirring for 15 min, the final product was recovered by filtration, washed with 50 mL of ethanol, and oven-dried at 80 °C for 1 h. The amount of coupled FITC was determined by dissolving the sample (typically 15 – 30 mg) in 25 mL of 0.2 M aq NaOH and measuring the UV-Vis absorption spectrum of the resulting clear solution after appropriate dilution. Repeated analysis of the same sample gave an average relative error of 3 % (for FITC contents in the range of 0.01–0.4 mmol/g). The extinction coefficient which was used in the calculations (ε = 75000 $M^{-1}cm^{-1}$ at λ_{max} = 490 nm) was determined based on a stock solution prepared as follows: FITC was coupled to APTMS in a 1:1 molar ratio by stirring in ethanol for 15 h at room temperature. After removal of the solvent by evaporation, a weighed amount of the dry residue was dissolved in 50 mL of 0.2 M aq NaOH containing 50 mg of dissolved silica.

D.2.4. Amino Group Analysis

An amount of 15 mg of amino-functionalized silica was stirred in 30 mL of 0.02 M aq NaOH until completely dissolved. A 100 µL aliquot of this solution was transferred into a cuvette (d = 1 cm) and 2 mL of phosphate buffer (0.2 M, pH 8.0) was added. After the addition of 1 mL of fluorescamine (Sigma) solution (1 mM in acetone), the fluorescence spectrum was measured by excitation at 366 nm. The emission intensity at 480 nm was taken as the data point. A calibration line was prepared accordingly by using 100 µL aliquots of differently concentrated solutions of APTMS in 30 mL of 0.02 M aq NaOH (containing 15 mg of the respective dissolved parent silica).[10] Repeated analysis of the same sample gave an average relative error of 8 % (for amino contents in the range of 0.09–2.4 mmol/g). To allow comparison between materials with different surface area, the amino content was further calculated in units of µmol/m^2 by assuming a homogeneous distribution over the entire BET surface area of the parent material. Curves depicting the FITC coupling yield as a function of the amino content were additionally verified with at least three control samples per curve.

To check the accuracy of this method for the quantitative analysis of surface-grafted amino groups, results were compared to values obtained by means of ele-

mental (CHN) analysis. The latter method is expected to provide reliable results for samples with high amino group contents. Values obtained by elemental analysis were in good agreement with the results of the fluorescamine based analysis, as shown for the following representative C-samples (in units of mmol/g; values of the fluorescamine based analysis in parentheses): 1.72 for MCM-41(12) (1.81), 1.80 for MCM-41(16) (1.75), 1.38 for SBA-15 (1.41), 1.89 for MCM-48 (1.97), and 1.33 for nano-MCM-41 (1.36).

D.2.5. Physical Measurements

Nitrogen sorption isotherms were collected at 77 K using a Quantachrome NOVA 2200 surface area and pore size analyzer. Samples were vacuum-degassed at 80 °C for 3 h. The total surface area S_{BET} was calculated by the BET method[23] whereas the external surface area S_{Ext} was determined from the high-pressure linear part of the α_S-plot.[24,25] Pore size distributions (PSDs) were calculated by means of a NLDFT model developed for silica exhibiting cylindrical pore geometry[26] (NOVAWin2 software, Version 2.2, Quantachrome Instruments). Adsorption branches were used for the calculations.[27] PSDs of the functionalized materials are used for comparative purposes only, as the employed NLDFT kernel is not strictly valid for silica materials with modified surfaces. The total pore volume V_{tot} was estimated from the amount of nitrogen adsorbed at a relative pressure of 0.95. The primary mesopore volume V_p (volume of the uniform mesopores) was determined by the α_S-plot method.[24] The de Boer equation was employed for calculating the statistical film thickness *t*.[28] A Perkin-Elmer LS50B spectrofluorometer was used for the fluorescamine assays, and UV-Vis spectra were measured with a Cary 1E spectrophotometer. Powder diffraction patterns were collected on a STOE StadiP diffractometer operating with monochromatized $CuK\alpha_1$ radiation. Scanning electron microscopy (SEM) was performed with a LEO 440. A LECO CHNS-932 was used for elemental (CHN) analysis.

D.3. Results and Discussion

D.3.1. Properties of the Starting Materials

Figures 1 and 2 show the PSDs of the investigated mesoporous silicas. Except for MCM-41(12), the materials were synthesized according to published procedures (see Experimental Section) and the XRD patterns corresponded well to those reported in the respective references. The XRD pattern of MCM-41(12) is given in Figure 1. As expected, the reflexes are shifted to larger angles compared to MCM-41(16). The presence of the (110) and (200) reflexes is indicative of a well-ordered MCM-41 type material.[6] Further properties of the unmodified materials are summarized in Table 1.

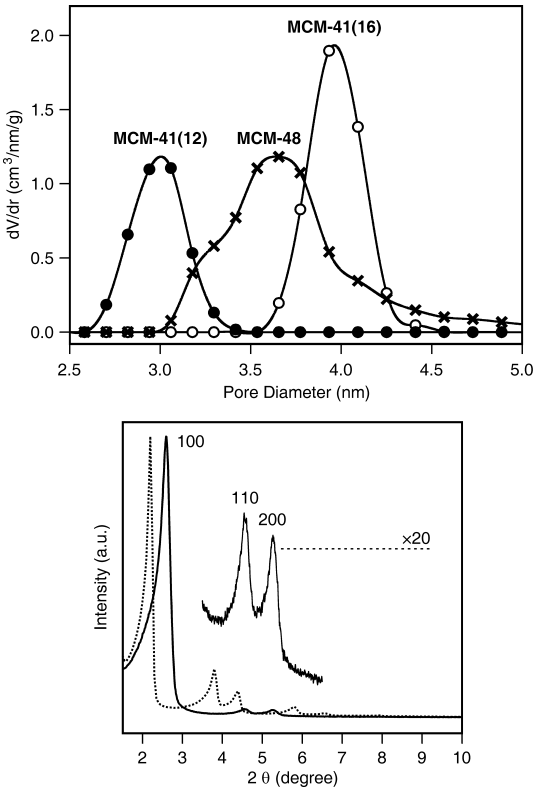

Figure 1. Top: PSD of unmodified MCM-41(12), MCM-41(16), and MCM-48. Bottom: XRD pattern of MCM-41(12) (solid lines) and MCM-41(16) (dashed line). The patterns have been scaled to the same maximum intensity.

D.3.2. FITC Coupling Yields and Accessibility

There are several reasons why FITC is an ideal molecule to probe the accessibility of surface-grafted amino groups: Isothiocyanates are moderately reactive and form robust thioureas with amines, whereas no reaction occurs with surface silanol groups under mild conditions.[11] As the fluorescein moiety is rather bulky (Figure 3), coupled FITC molecules can, depending on the pore size and pore system dimensionality, induce pore blocking, thereby rendering amino groups anchored in areas deep inside the pores inaccessible. Upon dissolution of the silica framework in 0.2 M aq NaOH, the fluorescein moiety is stable and

forms the strongly colored dianion,[29] affording an accurate and convenient determination of the FITC coupling yield by UV-Vis spectroscopy. The FITC coupling yield, which we define as the amount of coupled FITC divided by the amount of grafted amino groups, is a direct measure for the overall accessibility.

When investigating the effect of the pore size on the accessibility, it is important to keep in mind that reactions also occur on the external surface of the particles. Analysis of the high-pressure linear parts of the α_S-plots of the investigated mesoporous silicas reveals that the external surface area typically accounts for less than 15 % of the total BET surface area (Table 1). The nanometer-sized MCM-41 sample (nano-MCM-41) is an obvious exception. Because of the small particle size, the external surface is dominant.

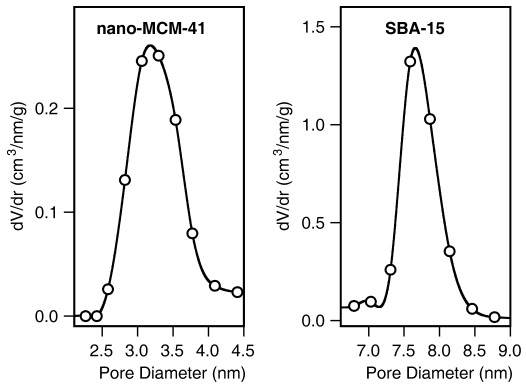

Figure 2. PSD of unmodified nano-MCM-41 and SBA-15.

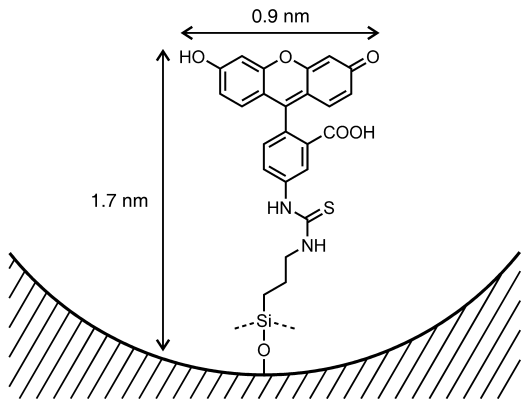

Figure 3. FITC-labeled grafted amino group. The curvature of the surface corresponds to a circular pore with a diameter of 3.5 nm. The anchored fluorescein moieties are most likely present in various protonation states (neutral, monoanion, dianion).[11]

It is instructive to first examine the FITC coupling yields of a nonporous high external surface area sample such as fumed silica. As can be seen in Figure 4, the FITC coupling yield remains relatively constant with increasing amino content. The slight overall decrease of the yield can be explained based on the simple model of two adjacent surface-grafted amino groups. As the distance between the amino groups decreases, the probability increases that, for steric reasons, only one of the two groups can be labeled with FITC. Note that an amino content of 1.7 μmol/m^2 corresponds to roughly one amino group per nm^2, assuming uniform distribution.

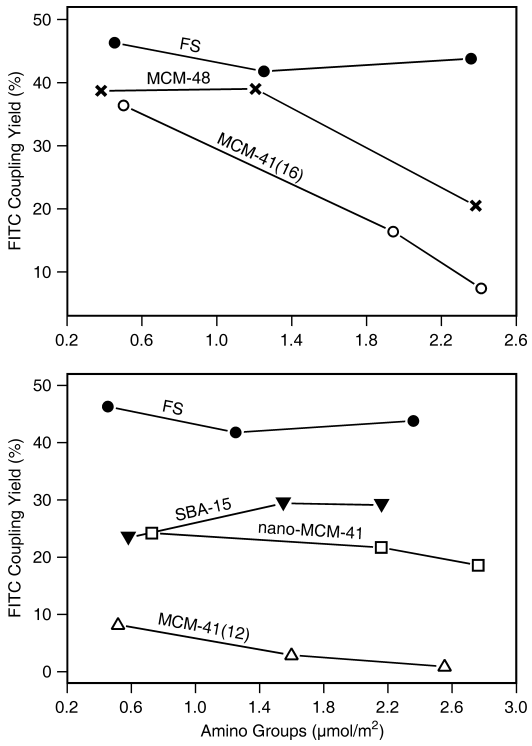

Figure 4. FITC coupling yield as a function of the amino content for fumed silica (FS), MCM-48, MCM-41(16), SBA-15, nano-MCM-41, and MCM-41(12). Each data point corresponds to the average of three independent syntheses.

Table 1. Properties of the investigated silica materials.

	d_{DFT}[a] [nm]	Particle Size[b]	S_{BET} [m^2/g]	S_{Ext} [m^2/g]	V_{tot} (V_p) [cm^3/g]
fumed silica	–	14 nm[c]	200	200	– (–)
nano-MCM-41	3.18	20 – 50 nm[d]	590	380	0.81 (0.17)
MCM-41(12)	3.06	1 – 2 µm	820	40	0.48 (0.44)
MCM-41(16)	3.93	1 – 2 µm	870	70	0.74 (0.67)
MCM-48	3.67	1 – 2 µm	1100	160	0.86 (0.75)
SBA-15	7.59	1 – 2 µm	860	50	1.21 (1.09[e])

[a] Average pore diameter determined by the NLDFT method. [b] Estimated by SEM unless noted otherwise. [c] Average size of primary particles, which form branched, chain-like aggregates a few tenths of a micrometer long (information provided by the supplier). [d] Reference 22. [e] Micropore volume V_μ = 0.09 cm^3/g.

Compared to the almost constant FITC coupling yield of the fumed silica samples, the values for MCM-41(16) strongly depend on the amount of grafted amino groups. As MCM-41 features one-dimensional channels, coupling of FITC to amino groups located close to the pore entrances can render large portions of the pore surface inaccessible. MCM-48 of similar pore size exhibits a less pronounced decrease of the FITC coupling yield with increasing amino content. The three-dimensional channel system obviously offers access to a large fraction of the pore surface despite potential pore blocking. MCM-48 and MCM-41(16) feature similar accessibility for amino loadings below 0.5 µmol/m^2.

Apart from the dimensionality of the pore system, the pore size plays an important role in defining the access to the amino groups. MCM-41(12) features FITC coupling yields of less than 10 %, indicative of strong pore blocking effects. SBA-15, on the other hand, exhibits FITC coupling yields larger than 20 % (Figure 4). Contrary to the MCM-41 type materials, the FITC coupling yield does not decrease with increasing amino content in the case of the SBA-15 samples. We can thus assume that virtually no pore blocking due to FITC labeling occurs at an average pore diameter of 7.59 nm. However, while the FITC coupling yield is almost constant for amino-functionalized SBA-15, the absolute amount of coupled FITC is much lower than in the case of fumed silica. This observation is discussed in more detail in Chapter D.3.3.

MCM-41(12) and MCM-41(16) feature significantly different FITC coupling yields despite their relatively small pore diameter difference (Δd_{DFT} = 0.87 nm). This is best illustrated by inspecting the A-samples, i.e., the samples with the lowest amino content (0.5 µmol/m^2, corresponding in this case to approximately 0.4 mmol/g). Whereas 1.0 g of the amino-functionalized MCM-41(16) sample is able to bind 0.13 mmol of FITC, the corresponding MCM-41(12) sample binds only 0.03 mmol, leading to the conclusion that in the latter case, FITC predominantly reacts with amino groups anchored to the external surface. This is in agreement with nitrogen sorption data of the samples before and after FITC coupling (Figure 5, Table 2). In the case of A-MCM-41(12), grafting of 0.4 mmol/g of APTMS led to a reduction of the pore volume but only to a slight accompanying decrease of the pore diameter, thus indicating preferential functionalization at the pore entrances and a scarcely functionalized pore body. The same observation is made for the MCM-41(12) samples with higher amino contents. It is interesting to note that upon FITC coupling, the pore volume and BET surface area increase in the case of A-MCM-41(12). This effect is most likely due to the removal of small amounts of grafted aminopropylsilanes upon stirring in ethanol for 24 h. As the amount of coupled FITC is small and presumably accumulated on the external particle surface of MCM-41(12), the loss of pore surface-grafted amino groups is not compensated by intrapore coupling of FITC. For MCM-41(16), on the other hand, a significant reduction of the pore volume was observed over the entire range of investigated amino contents, confirming that even at high amino content (C-MCM-41(16)), FITC is able to couple to amino groups located on the pore surface. However, the PSDs before and after FITC coupling (Figure 5) suggest that with increasing amino content, FITC couples predomi-

nantly to pore entrance sites of MCM-41(16), leading to a reduction of the pore volume while retaining a relatively large pore diameter.

The binding of FITC to pore entrance sites of amino-functionalized MCM-41(16) causes pore blocking with increasing amino content, thereby reducing the FITC coupling yield (Figure 4). It has recently been shown that the functionalization of MCM-41 by postsynthetic grafting of APTMS leads to a nonuniform distribution of amino groups with high concentrations on the external surface and at the pore entrances.[30] A high density of amino groups at the pore openings promotes pore blocking upon FITC coupling. Figure 5 also shows the PSDs of the corresponding SBA-15 samples, which illustrate the expected outcome of a comparatively more uniform distribution of amino groups and coupled FITC. Narrow PSDs are obtained for amino-functionalized and for FITC-coupled samples even in the case of high loadings (C-SBA-15). This is in contrast to the comparatively broad PSDs of the highly loaded MCM-41 type samples. We have recently shown that broadened PSDs are a direct consequence of nonuniform distributions of surface-grafted moieties.[11]

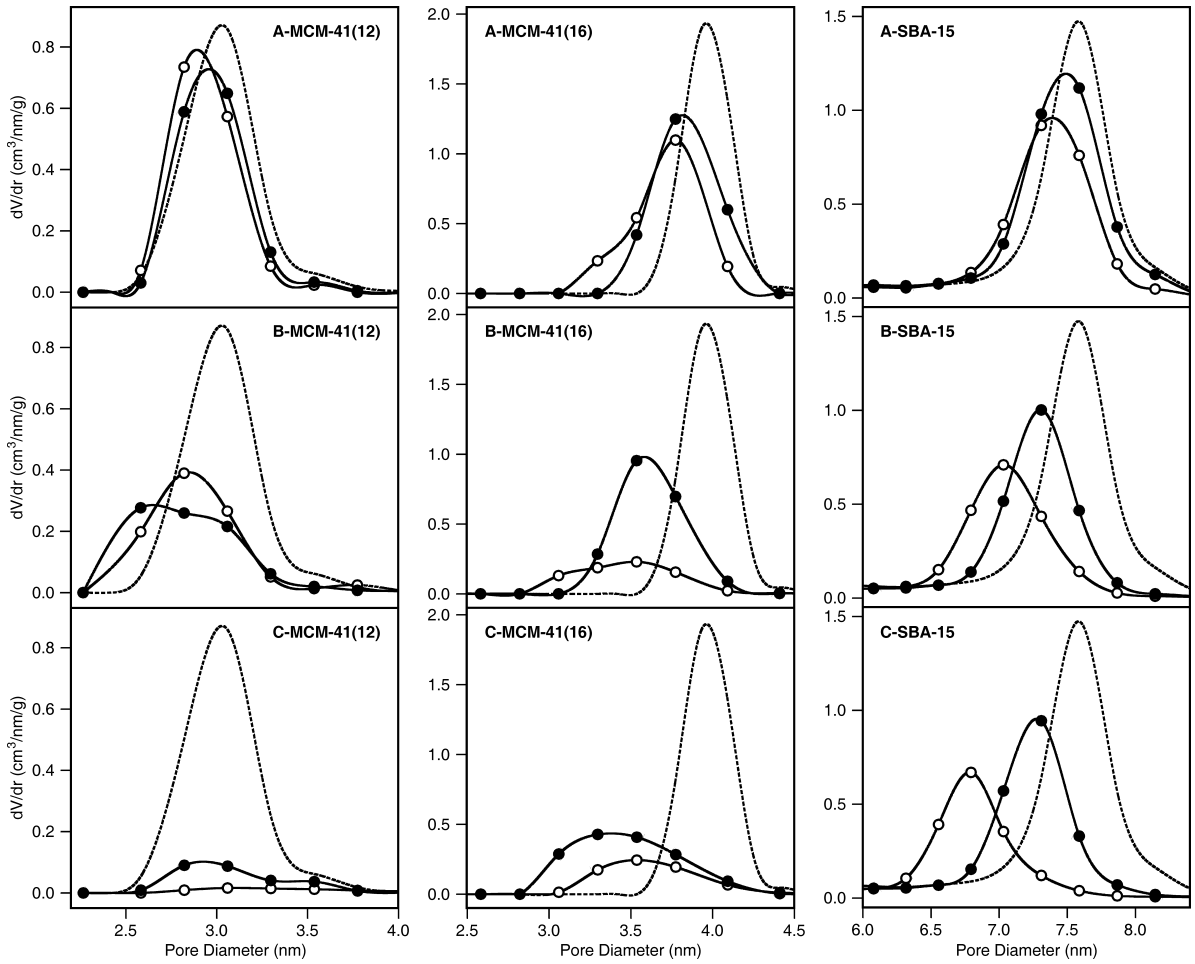

Figure 5. PSDs of selected amino-functionalized MCM-41(12), MCM-41(16), and SBA-15 samples before (filled circles) and after (empty circles) FITC coupling. The dashed lines represent the PSDs of the respective unmodified parent materials. The amino content increases from the A- to the C-samples. Additional characterization data is compiled in Table 2.

Table 2. Structural data of selected amino-functionalized samples.

	n [mmol/g]		S_{BET} [m^2/g]		V_{tot} (V_p) [cm^3/g]	
	–NH_2[a]	FITC[b]	–NH_2[c]	FITC[d]	–NH_2[c]	FITC[d]
A-MCM-41(12)	0.38	0.03	665	717	0.38 (0.34)	0.40 (0.36)
B-MCM-41(12)	1.09	0.03	464[e]	464[e]	0.22 (0.18)	0.25 (0.22)
C-MCM-41(12)	1.81	0.01	130[e]	39[e]	0.08 (0.07)	0.04 (0.01)
A-MCM-41(16)	0.40	0.13	810	740	0.66 (0.59)	0.57 (0.50)
B-MCM-41(16)	1.43	0.26	664	284[e]	0.51 (0.45)	0.22 (0.17)
C-MCM-41(16)	1.75	0.10	560	268[e]	0.40 (0.36)	0.21 (0.17)
A-SBA-15	0.40	0.09	716	569	1.08 (1.00)	0.86 (0.80)
B-SBA-15	1.02	0.31	541	407	0.79 (0.73)	0.62 (0.57)
C-SBA-15	1.41	0.34	437	316	0.70 (0.64)	0.49 (0.45)

[a] Amount of amino groups determined by fluorescamine analysis. [b] Amount of coupled FITC. [c] Amino-functionalized sample. [d] Amino-functionalized sample after FITC coupling. [e] Isotherm shows broad hysteresis extending into the BET region.

Inspection of the nitrogen sorption isotherms reveals that in some specific cases, the desorption isotherm does not close at lower relative pressure. Such broad hysteresis has been reported for mesoporous organosilicas and has been interpreted as a consequence of bottlenecking of pore openings, although the existence of a pronounced hysteresis at low relative pressure is not clearly understood.[31,32] Interestingly, we have observed such broad hysteresis for samples where the FITC coupling yields as well as the PSDs indicate strong pore blocking. For MCM-41(16), hysteresis was only observed for B- and C-samples after FITC coupling, whereas the sorption isotherms of MCM-41(12) featured a broad hysteresis already after reaction with APTMS (B- and C-samples, Figure 6), suggesting a highly nonuniform distribution of the grafted amino groups with increased concentration at the pore entrances. SBA-15 samples exhibited the typical H1 hysteresis loops, closing at a relative pressure above 0.5, irrespective of the amino and FITC content.

D.3.3. The Role of Microporosity

It is well-known that SBA-15 contains intrawall pores, which may constitute up to 30 % of the total porosity.[33] These intrawall pores include micropores,[34-36] which provide connectivity between the primary mesopores.[37] Grafting of APTMS obviously also occurs in these smaller pores. Along the same line of reasoning, one can expect that a high degree of surface roughness leads to a larger fraction of inaccessible amino groups. It has recently been proposed that SBA-15 features a higher degree of pore surface roughness and a larger amount of surface defects than MCM-41.[38-40] Grafting of APTMS in the intrawall pores of SBA-15 is one possible explanation for the comparatively low overall FITC coupling yields. It is worth mentioning that at very low amino content (0.1 μmol/m^2) the FITC coupling yield dropped to 15 % (compared to close to 40 % for a corresponding MCM-41(16) sample). This is most likely a consequence of preferential intrawall micropore adsorption of APTMS.

The presence of micropores in SBA-15 leads to various problems in the determination of textural properties. A large micropore volume renders the standard BET analysis unreliable. Galarneau et al. proposed that in such cases the actual surface areas are much lower than what is obtained by BET analysis.[41] Regarding the results shown in Figure 4, this would imply a higher grafting density for the SBA-15 samples. However, we obtained a C_{BET} value of 120, which is well within the normal range of values expected for silica adsorbents and confirms that the system is in the field of application of the BET equation.[41,42]

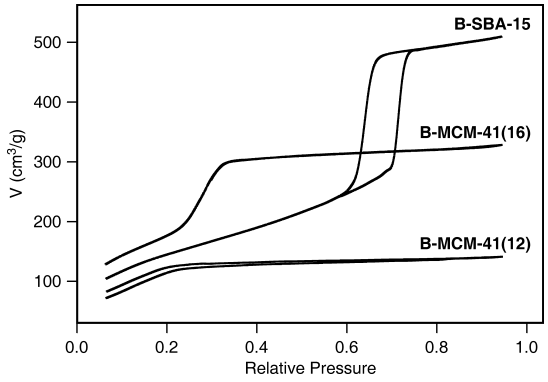

Figure 6. Nitrogen sorption isotherms of selected amino-functionalized B-samples. In the case of B-MCM-41(12), the desorption isotherm lies above the adsorption isotherm at low relative pressure.

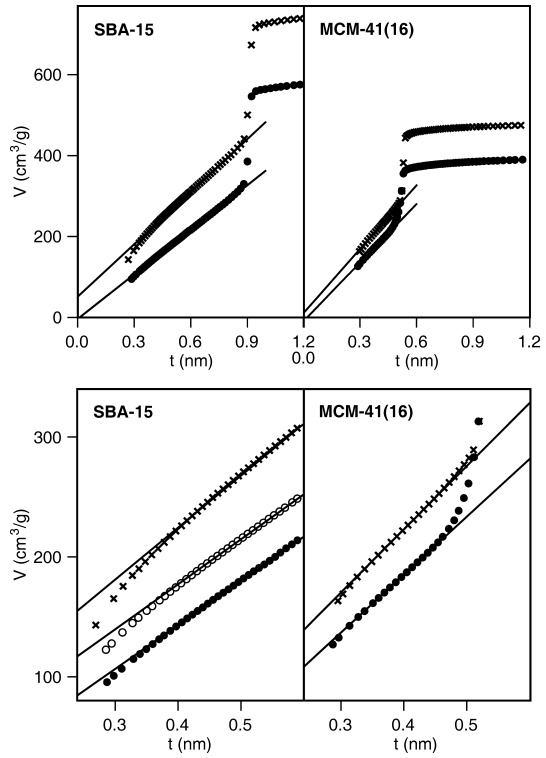

Figure 7. *t*-Plots of SBA-15 and MCM-41(16) before (crosses) and after (solid circles) reaction with APTMS. The amino contents are 0.5 μmol/m^2. The bottom panels show a magnified view of the low pressure region. The empty circles represent a SBA-15 sample with an amino content of 0.1 μmol/m^2.

Comparison of the *t*-curves of the unmodified SBA-15 and a corresponding amino-functionalized sample (A-SBA-15) reveals that the positive intercept of the *t*-curve of the parent SBA-15, which is an indication of microporosity, is no longer observed after APTMS grafting (Figure 7, top left). A distinct deviation from linearity at low *t*-values provides additional evidence for the presence of micropores in the parent SBA-15. Improved *t*-curve linearity is obtained after APTMS grafting. This effect can already be observed for a relatively low amino content of 0.1 μmol/m^2 (Figure 7, bottom left). In the case of analogous MCM-41(16) samples, the initial linear parts of the *t*-curves approach the origin independent of amino-functionalization, showing only a minor deviation from linearity (Figure 7, right). This is the expected behavior of a purely mesoporous material.

D.3.4. Nanoparticles of MCM-41

Functionalized mesoporous silica nanoparticles are of interest for medical and biological applications, such as cell labeling and magnetic resonance imaging,[43-45] as well as intracellular controlled-release delivery.[46-51] Because of the short channel lengths and the major contribution of the external surface to the total surface (Table 1), the postsynthetic functionalization behavior of mesoporous silica nanoparticles is substantially different from their micrometer-sized counterparts. Only a small fraction of the total pore volume is attributed to the primary mesopores. The comparatively large value for V_{tot} is mainly due to interparticle spaces.[22] As can be seen from Figure 4, the overall accessibility of the grafted amino groups is excellent in the case of the MCM-41 nanoparticles, decreasing only slightly with increasing amino content.

The FITC coupling yields of fumed silica, SBA-15, MCM-41(12), and nano-MCM-41 remain virtually constant in the investigated range of amino contents (Figure 4). The absolute values of the respective yields are, however, significantly different. In the case of SBA-15, we have attributed the lower absolute yield to the presence of intrawall micropores. In the case of nano-MCM-41, part of the surface is concave, thereby reducing the overall accessibility compared to the nonporous fumed silica samples. Interestingly, the absolute FITC coupling yields are much lower for MCM-41(12) than for nano-MCM-41, despite their almost identical average pore diameter (Δd_{DFT} = 0.12 nm). This is most likely a consequence of the much smaller external surface area and longer channels of MCM-41(12).

D.4. Conclusions

Our conclusions concerning the accessibility of amino groups in the one-dimensional channel systems of MCM-41(12), MCM-41(16), and SBA-15 are illustrated by the schematic snapshots shown in Figure 8.

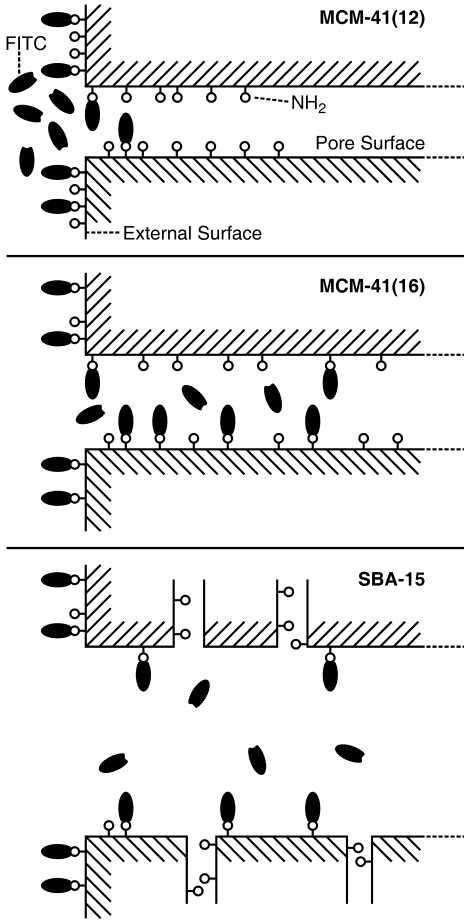

Figure 8. Schematic snapshots illustrating the labeling of functional groups grafted to MCM-41(12), MCM-41(16), and SBA-15.

The small pore diameter of MCM-41(12) facilitates the formation of blocked pores upon coupling of FITC to amino groups located at the pore entrances. The nonuniform distribution of the amino groups obtained after postsynthetic functionalization with APTMS further promotes pore blocking upon FITC coupling. A slightly larger pore diameter (MCM-41(16)) provides higher FITC coupling yields, which are, however, extremely sensitive to the total amount of grafted amino groups. High amino contents increase the probability of bottleneck formation by coupling of FITC to densely grafted amino groups at the pore entrances. This effect can be exploited to obtain a selective functionalization of the external surface and of the pore surface close to the channel entrances.

The accessibility of the amino groups grafted to the mesopore walls of SBA-15 is comparable to the accessibility on an open surface. The large pore diameter provides access to sites deep inside the pores irrespective of the total amino content. However, the microporosity and surface roughness of SBA-15 renders a considerable fraction of amino groups inaccessible. As expected, increased accessibility is observed for materials with short channels or three-dimensional pore systems.

When carrying out multistep functionalization reactions, such as grafting a precursor and subsequent coupling of a further functional moiety, the relationship between the amount of grafted precursor and the accessibility has to be taken into account. This is especially critical when the size of the moiety to be coupled is similar to or larger than half the pore diameter.

Acknowledgments. Financial support was provided by the European Commission through the Human Potential Programme (Marie-Curie RTN Nanomatch, grant No. MRTN-CT-2006-035884) and by the Swiss National Science Foundation (project 200020-117591). We would like to thank Stefan Ritter (Paul Scherrer Institute) for SEM measurements and Nando Gartmann for the determination of extinction coefficients.

References

(1) Rohlfing, Y.; Wöhrle, D.; Rathouský, J.; Zukal, A.; Wark, M. *Stud. Surf. Sci. Catal.* **2002**, *142*, 1067.

(2) Antochshuk, V.; Olkhovyk, O.; Jaroniec, M.; Park, I.-S.; Ryoo, R. *Langmuir* **2003**, *19*, 3031.

(3) Acosta, E. J.; Carr, C. S.; Simanek, E. E.; Shantz, D. F. *Adv. Mater.* **2004**, 16, 985.

(4) Descalzo, A. B.; Jimenez, D.; Marcos, M. D.; Martínez-Máñez, R.; Soto, J.; El Haskouri, J.; Guillém, C.; Beltrán, D.; Amorós, P.; Borrachero, M. V. *Adv. Mater.* **2002**, *14*, 966.

(5) Rosenholm, J. M.; Lindén, M. *Chem. Mater.* **2007**, *19*, 5023.

(6) Beck, J. S.; Vartuli, J. C.; Roth, W. J.; Leonowicz, M. E.; Kresge, C. T.; Schmitt, K. D.; Chu, C. T.-W.; Olson, D. H.; Sheppard, E. W.; McCullen, S. B.; Higgins, J. B.; Schlenker, J. L. *J. Am. Chem. Soc.* **1992**, *114*, 10834.

(7) Kresge, C. T.; Leonowicz, M. E.; Roth, W. J.; Vartuli, J. C.; Beck, J. S. *Nature* **1992**, *359*, 710.

(8) Zhao, D.; Feng, J.; Huo, Q.; Melosh, N.; Fredrickson, G. H.; Chmelka, B. F.; Stucky, G. D. *Science* **1998**, *279*, 548.

(9) Zhao, D.; Huo, Q.; Feng, J.; Chmelka, B. F.; Stucky, G. D. *J. Am. Chem. Soc.* **1998**, *120*, 6024.
(10) Ritter, H.; Nieminen, M.; Karppinen, M.; Brühwiler, D. *Microporous Mesoporous Mater.* **2009**, *121*, 79.
(11) Salmio, H.; Brühwiler, D. *J. Phys. Chem. C* **2007**, *111*, 923.
(12) Taguchi, A.; Schüth, F. *Microporous Mesoporous Mater.* **2005**, 77, 1.
(13) Clark, J. H.; Macquarrie, D. J.; Tavener, S. J. *Dalton Trans.* **2006**, 4297.
(14) Cides da Silva, L. C.; dos Santos, L. B. O.; Abate, G.; Cosentino, I. C.; Fantini, M. C. A.; Masini, J. C.; Matos, J. R. *Microporous Mesoporous Mater.* **2008**, *110*, 250.
(15) Fryxell, G. E.; Mattigod, S. V.; Lin, Y.; Wu, H.; Fiskum, S.; Parker, K.; Zheng, F.; Yantasee, W.; Zemanian, T. S.; Addleman, R. S.; Liu, J.; Kemner, K.; Kelly, S.; Feng, X. *J. Mater. Chem.* **2007**, *17*, 2863.
(16) Yoshitake, H. *New J. Chem.* **2005**, *29*, 1107.
(17) Ho, K. Y.; McKay, G.; Yeung, K. L. *Langmuir* **2003**, 19, 3019.
(18) Nooney, R. I.; Kalyanaraman, M.; Kennedy, G.; Maginn, E. J. *Langmuir* **2001**, *17*, 528.
(19) Liu, A. M.; Hidajat, K.; Kawi, S.; Zhao, D. Y. *Chem. Commun.* **2000**, 1145.
(20) Brühwiler, D.; Frei, H. *J. Phys. Chem. B* **2003**, *107*, 8547.
(21) Xu, J.; Luan, Z.; He, H.; Zhou, W.; Kevan, L. *Chem. Mater.* **1998**, *10*, 3690.
(22) Suzuki, K.; Ikari, K.; Imai, H. *J. Am. Chem. Soc.* **2004**, *126*, 462.
(23) Brunauer, S.; Emmett, P. H.; Teller, E. *J. Am. Chem. Soc.* **1938**, *60*, 309.
(24) Kruk, M.; Jaroniec, M.; Ryoo, R.; Kim, J. M. *Microporous Mater.* **1997**, *12*, 93.
(25) Sayari, A.; Liu, P.; Kruk, M.; Jaroniec, M. *Chem. Mater.* **1997**, *9*, 2499.
(26) Ravikovitch, P. I.; Domhnaill, S. C. O.; Neimark, A. V.; Schüth, F.; Unger, K. K. *Langmuir* **1995**, *11*, 4765.
(27) Ravikovitch, P. I.; Neimark, A. V. *Colloid Surf. A* **2001**, *187-188*, 11.
(28) Lippens, B. C.; de Boer, J. H. *J. Catal.* **1965**, *4*, 319.
(29) Martin, M. M.; Lindqvist, L. *J. Lumin.* **1975**, *10*, 381.
(30) Yokoi, T.; Yoshitake, H.; Tatsumi, T. *J. Mater. Chem.* **2004**, *14*, 951.
(31) Li, C.; Yang, J.; Shi, X.; Liu, J.; Yang, Q. *Microporous Mesoporous Mater.* **2007**, *98*, 220.
(32) Burleigh, M. C.; Markowitz, M. A.; Spector, M. S.; Gaber, B. P. *J. Phys. Chem. B* **2001**, *105*, 9935.
(33) Ravikovitch, P. I.; Neimark, A. V. *J. Phys. Chem. B* **2001**, *105*, 6817.
(34) Ryoo, R.; Ko, C. H.; Kruk, M.; Antochshuk, V.; Jaroniec, M. *J. Phys. Chem. B* **2000**, *104*, 11465.
(35) Impéror-Clerc, M.; Davidson, P.; Davidson, A. *J. Am. Chem. Soc.* **2000**, *122*, 11925.
(36) Galarneau, A.; Cambon, H.; Di Renzo, F.; Ryoo, R.; Choi, M.; Fajula, F. *New J. Chem.* **2003**, *27*, 73.
(37) Jun, S.; Joo, S. H.; Ryoo, R.; Kruk, M.; Jaroniec, M.; Liu, Z.; Ohsuna, T.; Terasaki, O. *J. Am. Chem. Soc.* **2000**, *122*, 10712.
(38) Ravikovitch, P. I.; Neimark, A. V. *Langmuir* **2006**, *22*, 11171.
(39) Shenderovich, I. G.; Buntkowsky, G.; Schreiber, A.; Gedat, E.; Sharif, S.; Albrecht, J.; Golubev, N. S.; Findenegg, G. H.; Limbach, H.-H. *J. Phys. Chem. B* **2003**, *107*, 11924.
(40) Fenelonov, V. B.; Derevyankin, A. Y.; Kirik, S. D.; Solovyov, L. A.; Shmakov, A. N.; Bonardet, J.-L.; Gedeon, A.; Romannikov, V. N. *Microporous Mesoporous Mater.* **2001**, *44-45*, 33.
(41) Galarneau, A.; Cambon, H.; Di Renzo, F.; Fajula, F. *Langmuir* **2001**, *17*, 8328.
(42) Rouquerol, F.; Rouquerol, J.; Sing, K. *Adsorption by powders & porous solids*; Academic Press, San Diego, CA, 1999.
(43) Wu, S.-H.; Lin, Y.-S.; Hung, Y.; Chou, Y.-H.; Hsu, Y.-H.; Chang, C.; Mou, C.-Y. *ChemBioChem* **2008**, *9*, 53.
(44) Taylor, K. M. L.; Kim, J. S.; Rieter, W. J.; An, H.; Lin, W.; Lin, W. *J. Am. Chem. Soc.* **2008**, *130*, 2154.
(45) Lin, Y.-S.; Tsai, C.-P.; Huang, H.-Y.; Kuo, C.-T.; Hung, Y.; Huang, D.-M.; Chen, Y.-C.; Mou, C.-Y. *Chem. Mater.* **2005**, *17*, 4570.
(46) Lu, J.; Liong, M.; Zink, J. I.; Tamanoi, F. *Small* **2007**, *3*, 1341.
(47) Torney, F.; Trewyn, B. G.; Lin, V. S.-Y.; Wang, K. *Nat. Nanotechnol.* **2007**, *2*, 295.
(48) Slowing, I.; Trewyn, B. G.; Lin, V. S.-Y. *J. Am. Chem. Soc.* **2007**, *129*, 8845.
(49) Slowing, I.; Trewyn, B. G.; Giri, S.; Lin, V. S.-Y. *Adv. Funct. Mater.* **2007**, *17*, 1225.
(50) Lu, J.; Liong, M.; Sherman, S.; Xia, T.; Kovochich, M.; Nel, A. E.; Zink, J. I.; Tamanoi, F. *Nanobiotechnology* **2007**, *3*, 89.
(51) Slowing, I.; Trewyn, B. G.; Lin, V. S.-Y. *J. Am. Chem. Soc.* **2006**, *128*, 14792.

6. Publication E

Controlling and imaging the functional-group distribution on mesoporous silica

Nando Gartmann and Dominik Brühwiler*

Institute of Inorganic Chemistry, University of Zurich, Winterthurerstrasse 190, 8057 Zurich, Switzerland

Angew. Chem. Int. Ed. 48 (2009) 6354 – 6356

Angew. Chem. 121 (2009) 6472 – 6475 (german version)

In, out, shake it all about: The distribution of fluorescence-labeled amino groups on mesoporous silica is imaged by confocal laser scanning microscopy. The mobility of the aminosilane precursor determines the degree of external vs. pore surface functionalization. This observation was used to develop a simple and general method for the modification of external mesoporous silica surfaces.

The control of the distribution of functional groups on mesoporous silica is essential for applications of these materials in various fields including catalysis,[1] drug delivery,[2] and sensing.[3] In order to define the interaction of the mesoporous silica particles with their surrounding medium, the selective modification of the external surface is of particular importance. Externally grafted functional groups can, for example, regulate the cellular uptake[4] or provide targeting ability[5] of mesoporous-silica-based drug-delivery systems.

The introduction of functional groups by grafting to a preformed mesoporous material (often referred to as *postsynthetic functionalization*) is a versatile modification method, as the desired pore-size distribution, pore system dimensionality, particle size, and particle morphology can be obtained in a straightforward manner. However, the control of the functional-group distribution poses a particular challenge. A recently reported concept employs fluorenylmethoxycarbonyl-(Fmoc)-modified organosilanes which are grafted to the external and internal (pore) surfaces of mesoporous silica. Under certain reaction conditions, the external surface groups can be deprotected selectively and subsequently functionalized further, whereas the groups located on the pore surface remain protected by Fmoc.[6] A frequently used general method for modifying the external surface is based on the reaction of chloro-, methoxy-, or ethoxysilanes with as-synthesized mesoporous silica, in other words, mesoporous silica still containing the structure-directing agent (SDA). We show herein that considerable grafting to the pore surface can occur despite the presence of the SDA, and we describe a convenient post-synthetic functionalization method with a high selectivity for the external surface.

Confocal laser scanning microscopy (CLSM) has been used to visualize the spatial distribution of fluorescent guests in mesoporous and microporous host materials.[7] The distribution of functional groups covalently bound to mesoporous silica can be similarly imaged after coupling with appropriate fluorescent labels. Large particles of defined morphology are ideal for this purpose. We have been working with hexagonal particles, also known as arrays of silica nanochannels (ASNCs),[8] as well as with spherical particles of the SBA-15 type (SBA-s)[9] featuring a less ordered pore system and a larger average pore size than the ASNCs (Figure 1, Table 1). In both cases, functionalization reactions were carried out either before or after removal of the SDA.

Tab. 1. Structural properties of the parent materials.

	ASNCs	SBA-s
Average Pore Diameter [nm]	2.9	ca. 5.5
BET Surface Area [m^2/g]	1120	795
External Surface Area [m^2/g]	37	10
Total Pore Volume [cm^3/g]	0.62	0.74

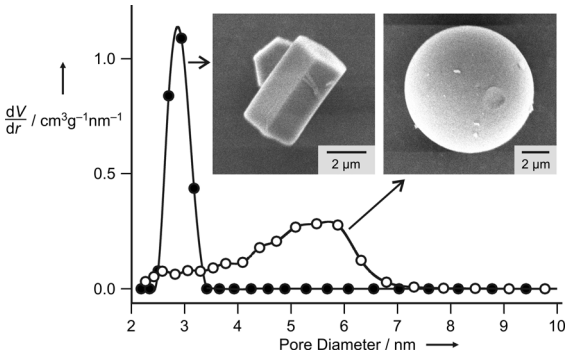

Figure 1. Pore-size distribution of ASNCs (●) and SBA-s (○). The well-defined morphology of the particles is evident in the corresponding electron micrographs. The image of the ASNCs shows two particles (one particle is standing on its hexagonal base).

Apart from the frequently employed 3-aminopropyltriethoxysilane (APTES), 3-aminopropyltris(methoxyethoxyethoxy)silane (APTMEES) and bis(triethoxysilylpropyl)amine (BTESPA) were used as reactants (Figure 2). The surface-grafted amino groups were subsequently labeled with fluorescein isothiocyanate (FITC) or Texas Red sulfonyl chloride (TR). Room temperature deposition of the silanes from hexane and curing at 80 °C led to the remarkably different distributions shown in Figure 2. The following can be concluded: 1) As a result of the comparatively large pore diameter, reaction with calcined SBA-s leads to a high degree of pore-surface grafting for all investigated silanes. The uniformity of the functional-group distribution decreases in the series APTES > BTESPA > APTMEES. As a consequence of the narrower channels, this tendency is more pronounced when grafting to calcined ASNCs. In the case of APTMEES, excellent selectivity for the external surface is obtained. The observation that BTESPA produces a less uniform distribution than APTES is in agreement with results obtained from a systematic study of the pore-size distributions and luminescence intensities of re-

spective FITC coupled, MCM-41-based samples.[10] 2) Despite the presence of the SDA, grafting of APTES to as-synthesized SBA-s and ASNCs leads to significant pore-surface derivatization. The reaction of APTES with as-synthesized mesoporous materials of the MCM-41 (alkyltrimethylammonium ions as SDA) and SBA-15 type (poly(alkylene oxide) block copolymer as SDA) is a frequently used procedure for the functionalization of the external surface. Our results show, however, that this method is not ideal. A similar result is obtained with BTESPA, despite its larger size and higher reactivity. The ability of ethoxy-, methoxy-, and chlorosilanes to displace the SDA from MCM-41-type materials can, in fact, be exploited to functionalize the pore surface.[11] 3) High selectivity for the external surface is observed upon grafting of APTMEES to as-synthesized materials.

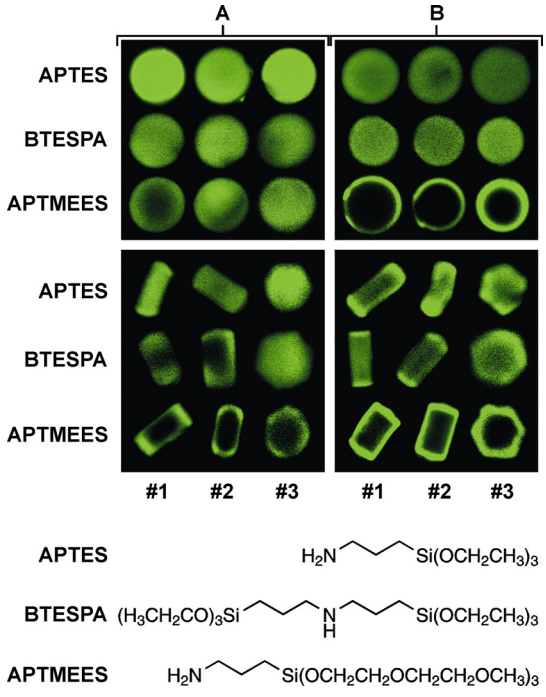

Figure 2. CLSM images (after FITC labeling) of SBA-s (top panels) and ASNCs (bottom panels) functionalized with APTES, BTESPA, or APTMEES. Three particles are shown for each silane/silica combination. In the case of the as-synthesized samples, the SDA was extracted after FITC labeling (B). The samples in (A) were calcined before the functionalization. Particles of ASNCs depicted in (A,#3) and (B,#3) are standing on their hexagonal base.

Analysis of the amount of surface-grafted amino groups by the fluorogenic derivatization reaction with fluorescamine[12] revealed quantitative adsorption of the respective silanes on calcined ASNCs and SBA-s. Exclusive grafting to the external surface would therefore give rise to an amino group density of 1.6 nm^{-2} for ASNCs and 6.0 nm^{-2} for SBA-s. As such high densities are unlikely, we assume that partial grafting to the pore surface occurs even in the case of APTMEES, although apparently predominantly at sites close to the pore entrances.

The question remains whether the pronounced tendency of APTMEES to graft to the external surface is a consequence of pore blocking. To exclude this possibility, we conducted the following experiment. As-synthesized SBA-s and ASNCs were functionalized with APTMEES as described above. After FITC labeling and extraction of the SDA, APTES was deposited from ethanol (3 h, RT), coupled to TR, and cured at 80 °C. The samples were washed repeatedly until the washing solution became colorless. Figure 3 shows that the bulky TR labels have entered the channels despite the presence of FITC-labeled amino groups on the external surface. This indicates that the pores are indeed accessible after external surface functionalization with APTMEES.

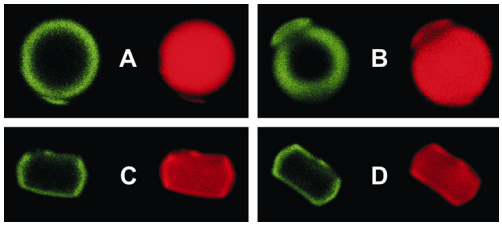

Figure 3. CLSM images of SBA-s (A and B) and ASNCs (C and D) after external-surface functionalization with APTMEES and labeling with FITC, followed by reaction with APTES in ethanol and labeling with TR. The left (green) images of each panel show the luminescence of the coupled FITC labels, whereas the right (red) images are obtained upon selective excitation of the TR labels.

Deposition of aminopropylalkoxysilanes on silica at room temperature results in the formation of hydrogen bonds between the amino groups and the surface silanols. There is evidence in the case of APTES that this adsorption step reaches an equilibrium within

1 min (in toluene).[13] Deprotonation of silanol groups by the amines can lead to electrostatic interactions. The formation of siloxane bonds prior to the curing step has been observed in the APTES/silica system.[13] The distribution of a given aminosilane is determined by its mobility on the mesoporous silica surface, and, in the case of as-synthesized materials, its ability to penetrate the SDA-filled channels. Our results suggest that APTMEES is significantly less mobile than BTESPA and APTES.

It is reasonable to assume that polar solvents lead to increased mobility. This concept has been used previously to control the site isolation of amino groups on mesoporous silica.[10,14] The combination of APTMEES deposition and CLSM imaging can be used to directly visualize the effect of the solvent on the functional-group distribution. As can be seen in Figure 4, the uniformity of the functional-group distribution increases in the series toluene(≈hexane) < THF < acetone ≈ ethanol.

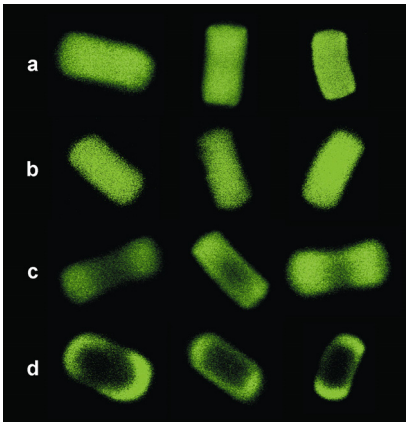

Figure 4. CLSM images of calcined ASNCs after functionalization with APTMEES in ethanol (a), acetone (b), THF (c), toluene (d), and subsequent FITC labeling. The amino content of the samples is close to 100 μmol/g.

In summary, we have shown that the deposition of APTMEES from hexane leads to excellent selectivity for the external surface of mesoporous silica. In case of small mesopore sizes, a high degree of external surface modification is obtained even for calcined samples. In work with as-synthesized samples, APTMEES is superior to the frequently used APTES in terms of its tendency to graft to the external particle surface. The mesopores remain accessible after external surface functionalization with APTMEES.

Experimental Section

Spherical SBA-15 particles (SBA-s) were synthesized as follows:[9] A solution of hexadecyltrimethylammonium bromide (0.465 g; Fluka) in H_2O (20 mL) was added to a solution of Pluronic P123 (3.10 g; EO_{20}-$PO_{70}EO_{20}$, M_{av} = 5800, Aldrich) in 1.5 M aqueous HCl (45.9 mL). After the addition of ethanol (7.8 mL), the mixture was stirred vigorously and tetraethoxysilane (10 mL; TEOS, Fluka) was added dropwise. Following further stirring for 2 h at RT, the mixture was transferred to a Teflon-lined autoclave and kept at 78 °C for 72 h. The product was obtained by filtration, washed with H_2O (50 mL), and dried at RT. Calcination was performed at 500 °C for 16 h with a heating rate of 1.2 K/min. As an alternative to calcination, the structure directing agent (SDA) was removed by Soxhlet extraction with ethanol during 24 h.[15]

ASNCs were prepared by a procedure similar to the one reported by Kievsky and Sokolov.[8] Hexadecyltrimethylammonium chloride (4.85 g; Acros) was dissolved in a mixture of doubly distilled H_2O (76 mL) and 32 % aqueous HCl (60 mL) by stirring for 1 min at ca. 1000 rpm in a polypropylene beaker. The solution was subsequently cooled to 0° C for 15 min without stirring, followed by the slow addition of cold TEOS (2 mL; Aldrich, 99.999 %) and further stirring for 30 s. The resulting mixture was kept at 0 °C under quiescent conditions for 3 h. The product was collected by filtration and washed with H_2O (250 mL). The SDA was removed by first heating at 300 °C for 2 h and calcining at 550 °C for 12 h. Heating rates of 2 K/min were applied. Alternatively, the SDA was extracted by dispersing 200 mg of the as-synthesized ASNCs in a solution of ammonium nitrate (90 mg) in ethanol (45 mL), and stirring the mixture at 60 °C for 15 min. For complete extraction, this step was repeated twice.[16] For both ASNCs and SBA-s, removal of the SDA by extraction was performed after aminosilane grafting and FITC coupling. Extraction of the SDA before FITC coupling led to the same results in terms of the distribution of the labels.

Amino groups were grafted to the mesoporous silica materials as follows: calcined or as-synthesized ASNCs or SBA-s (200 mg) was dispersed in hexane (10 mL) and APTES, APTMEES, or BTESPA (ABCR) (20 μmol) was added. After the mixture had been stirred for 10 min, the functionalized mesoporous

silica was recovered by filtration and cured in an oven at 80 °C for 16 h.

The samples were labeled by stirring in ethanol containing 3 equivalents (relative to the amount of the respective silane) of FITC (fluorescein 5-isothiocyanate, isomer I, Fluka) or TR (Texas Red sulfonyl chloride, mixed isomers, Molecular Probes) for 16 h at RT. The labeled samples were washed repeatedly with ethanol until the washing solution became colorless.

Nitrogen sorption isotherms were collected at 77 K using a Quantachrome NOVA 2200. Samples were vacuum-degassed at 80 °C for 3 h. The total surface area was calculated by the BET method, whereas the external surface area was determined from the high-pressure linear part of the α_S-plot ($\alpha_S > 1$).[17] Size distributions of the mesopores were evaluated by the NLDFT method developed for silica exhibiting cylindrical pore geometry (NOVAWin2 software, Version 2.2, Quantachrome).[18] The adsorption branch of the respective isotherm was used for the calculations. The total pore volume was determined by the amount of adsorbed nitrogen at a relative pressure of 0.95. Scanning electron microscopy images were acquired on a JEOL JSM-6060. The CLSM setup consisted of an Olympus BX 60 microscope equipped with a FluoView detector and lasers operating at 488 and 543.5 nm. Optical slices in the center of the particles were selected.

Financial support by the Swiss National Science Foundation (Project 200020-117591) and by the European Commission through the Human Potential Programme (Marie-Curie RTN Nanomatch, Grant No. MRTN-CT-2006-035884) is acknowledged.

References

[1] A. Taguchi, F. Schüth, *Microporous Mesoporous Mater.* **2004**, *77*, 1.

[2] M. Vallet-Regí, F. Balas, D. Arcos, *Angew. Chem. Int. Ed.* **2007**, *46*, 7548; *Angew. Chem.* **2007**, *119*, 7692.

[3] I. I. Slowing, B. G. Trewyn, S. Giri, V. S.-Y. Lin, *Adv. Funct. Mater.* **2007**, *17*, 1225.

[4] I. I. Slowing, B. G. Trewyn, V. S.-Y. Lin, *J. Am. Chem. Soc.* **2006**, *128*, 14792.

[5] M. Liong, J. Lu, M. Kovochich, T. Xia, S. G. Ruehm, A. E. Nel, F. Tamanoi, J. I. Zink, *ACS Nano* **2008**, *2*, 889.

[6] K. Cheng, C. C. Landry, *J. Am. Chem. Soc.* **2007**, *129*, 9674.

[7] a) S. Megelski, A. Lieb, M. Pauchard, A. Drechsler, S. Glaus, C. Debus, A. J. Meixner, G. Calzaferri, *J. Phys. Chem. B* **2001**, *105*, 25; b) M. Pauchard, S. Huber, R. Méallet-Renault, H. Maas, R. Pansu, G. Calzaferri, *Angew. Chem. Int. Ed.* **2001**, *40*, 2839; *Angew. Chem.* **2001**, *113*, 2921; c) C. Seebacher, J. Rau, F.-W. Deeg, C. Bräuchle, S. Altmaier, R. Jäger, P. Behrens, *Adv. Mater.* **2001**, *13*, 1374; d) G. Calzaferri, S. Huber, H. Maas, C. Minkowski, *Angew. Chem. Int. Ed.* **2003**, *42*, 3732; *Angew. Chem.* **2003**, *115*, 3860.

[8] Y. Kievsky, I. Sokolov, *IEEE Trans. Nanotechnol.* **2005**, *4*, 490.

[9] a) Y. Ma, L. Qi, J. Ma, Y. Wu, O. Liu, H. Cheng, *Colloids Surf. A* **2003**, *229*, 1; b) A. Katiyar, N. G. Pinto, *Small* **2006**, *2*, 644.

[10] H. Salmio, D. Brühwiler, *J. Phys. Chem. C* **2007**, *111*, 923.

[11] a) V. Antochshuk, M. Jaroniec, *Chem. Commun.* **1999**, 2373; b) V. Antochshuk, M. Jaroniec, *Chem. Mater.* **2000**, *12*, 2496.

[12] a) H. Ritter, M. Nieminen, M. Karppinen, D. Brühwiler, *Microporous Mesoporous Mater.* **2009**, *121*, 79; b) H. Ritter, D. Brühwiler, *J. Phys. Chem. C* **2009**, *113*, 10667.

[13] K. C. Vrancken, K. Possemiers, P. Van Der Voort, E. F. Vansant, *Colloids Surf. A* **1995**, *98*, 235.

[14] K. K. Sharma, A. Anan, R. P. Buckley, W. Ouellette, T. Asefa, *J. Am. Chem. Soc.* **2008**, *130*, 218.

[15] C. A. Melero, G. D. Stucky, R. van Grieken, G. Morales, *J. Mater. Chem.* **2002**, *12*, 1664.

[16] N. Lang, A. Tuel, *Chem. Mater.* **2004**, *16*, 1961.

[17] A. Sayari, P. Liu, M. Kruk, M. Jaroniec, *Chem. Mater.* **1997**, *9*, 2499.

[18] P. I. Ravikovitch, S. C. O. Domhnaill, A. V. Neimark, F. Schüth, K. K. Unger, *Langmuir* **1995**, *11*, 4765.

7. Publication F

The effect of water on the functionalization of mesoporous silica with 3-aminopropyltriethoxysilane

Nando Gartmann, Christina Schütze, Hanna Ritter, Dominik Brühwiler*

Institute of Inorganic Chemistry, University of Zurich, Winterthurerstrasse 190, 8057 Zurich, Switzerland

J. Phys. Chem. Lett. 1 (2010) 379 – 382

Abstract. The effect of water on the reaction of 3-aminopropyltriethoxysilane (APTES) with mesoporous silica is investigated on two model systems. A MCM-41 type material with a well-defined pore size is used to investigate changes in the pore size distribution upon reaction with APTES in toluene containing various amounts of water. It is found that with increasing amount of water, clustering of APTES occurs, leading to a non-uniform distribution of the grafted amino groups and a scarcely functionalized pore body. A second model system with defined particle morphology and one-dimensional channels is employed to visualize the distribution of the grafted amino groups by fluorescent labeling and confocal laser scanning microscopy. The combination of nitrogen sorption and confocal laser scanning microscopy provides valuable insights concerning the role of trace water in the functionalization of mesoporous silica with alkoxysilanes.

Postsynthetic functionalization by grafting of substituted trialkoxysilanes is one of the most popular methods for the modification of mesoporous silica. Aminopropylalkoxysilanes are frequently employed for this purpose, allowing subsequent reaction with a variety of functional groups, such as isothiocyanate or sulfonyl chloride. Amino-functionalized mesoporous silicas have further been investigated in terms of their potential applications in drug delivery,[1] catalysis,[2–6] and adsorption.[7,8] The identification of the parameters that control the distribution of the grafted amino groups has been the topic of recent publications. It has been shown that the polarity of the solvent used in the reaction of aminoalkyl-substituted alkoxysilanes with mesoporous silica has a pronounced influence on the distribution of the surface-anchored amino groups.[2,9] Water has been identified as one of the most important parameters in the reaction of trialkoxysilanes with silica surfaces. Excellent work has been carried out to identify possible binding modes of 3-aminopropyltriethoxysilane (APTES) on silica gel in dependence of surface water, leading to the conclusion that polymerization of APTES takes place on the silica surface after adsorption of the silane molecules.[10,11] In the case of mesoporous silica, one can assume that the polymerization of APTES on the pore surface affects the diffusion of further silane molecules and therefore determines the final distribution of the grafted functional groups.

Acquiring information on the distribution of functional groups on mesoporous silica is challenging and generally requires a comparative investigation of the nitrogen sorption isotherms.[12,13] Inspired by results obtained from the analysis of the spatial distribution of fluorescent guests in zeolites,[14,15] we have combined the nitrogen sorption based analysis with confocal laser scanning microscopy (CLSM).

The investigation of the functional group distribution by means of nitrogen sorption requires a starting material with a pore size distribution that is as narrow as possible, allowing the identification of subtle differences in the sorption isotherms upon functionalization. Our MCM-41 sample fulfils this condition and we have previously used this type of material for the study of functional group distributions.[12] However, the morphology of this particular MCM-41 sample is irregular and therefore not suitable for CLSM, which requires relatively large particles of defined morphology. Hexagonal particles (arrays of silica nanochannels, ASNCs)[16] are ideal for this purpose (Fig. 1, Tab. 1).

Starting from calcined MCM-41, we have prepared amino-functionalized samples by grafting APTES in toluene containing different amounts of water (Tab. 2). Amounts of water corresponding to 0.5, 1, and 2 theoretical monolayer(s) were used, taking into account that one water molecule occupies 0.106 nm^2 in an adsorbed monolayer.[17] A comparison of the pore size distribution and the amino group content of the products provides insight into the effect of water on the grafting behavior. While the amount of grafted amino groups is largely independent of the amount of water in the reaction mixture, the pore size distribution is clearly affected (Fig. 2). As expected, the sample prepared in dry toluene, M-0, features a narrow and symmetrical pore size distribution. Samples prepared with additional water, on the other hand, feature an increasing contribution of larger pores, suggesting a less uniform distribution of the amino groups.

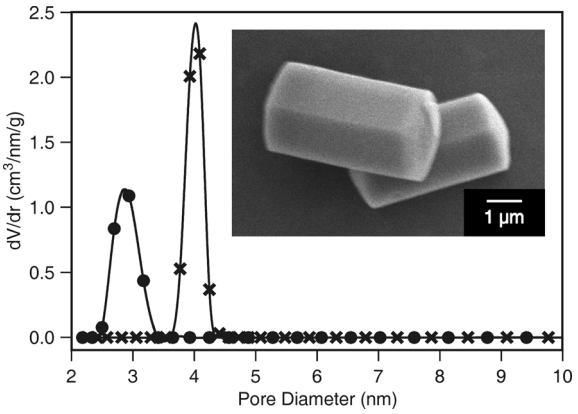

Figure 1. Pore size distributions of MCM-41 (crosses) and ASNCs (circles). The inset shows a scanning electron microscopy image of ASNCs.

Table 1. Structural properties of the parent materials.

sample	d_{NLDFT}[a] [nm]	S_{BET}[b] [m^2/g]	S_{Ext}[c] [m^2/g]	V_{tot}[d] [cm^3/g]
MCM-41	4.1	1014	78	0.86
ASNCs	2.9	1120	37	0.62

[a] pore diameter calculated by NLDFT
[b] total BET surface area
[c] external particle surface area
[d] total pore volume

Table 2. Amino-functionalized materials.

sample	silica	APTES [mmol/g]	H_2O[a]	$-NH_2$[b] [mmol/g]	FITC[c] [mmol/g]
M-0	MCM	0.40	0	0.36	–
M-0.5	MCM	0.40	0.5	0.36	–
M-1	MCM	0.40	1	0.35	–
M-2	MCM	0.40	2	0.34	–
A-0	ASNCs	0.40	0	0.36	0.11
A-1	ASNCs	0.40	1	0.37	0.11
A-2	ASNCs	0.40	2	0.36	0.08
A-0.1-2	ASNCs	0.10	2	0.10	0.02

[a] number of monolayers
[b] experimental amount of grafted amino groups
[c] experimental amount of coupled FITC

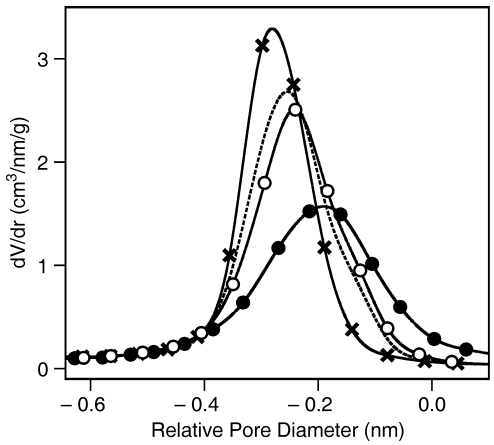

Figure 2. Pore size distributions of M-0 (crosses), M-0.5 (dashed line), M-1 (empty circles), and M-2 (full circles). The pore diameter is given relative to the maximum of the pore size distribution of the unmodified material.

From studies of the reaction of APTES with silica gel it is known that surface water promotes the interaction of the amino groups with the surface, partially by proton transfer from the surface silanols to the amino moieties and subsequent electrostatic interaction.[18] The resulting orientation of the amino groups towards the silica surface provides accessible triethoxysilyl moieties for cross-linking, ultimately leading to the formation of clusters. The presence of such clusters can render pores partially inaccessible for additional APTES molecules, thus resulting in a non-uniform distribution of the grafted amino groups. It should be noted that despite APTES clustering, the pores are still accessible for nitrogen molecules, leading to the detection of larger pores in materials functionalized in the presence of water. Pore volumes of the amino-functionalized materials were found to be largely independent of the presence of water in the reaction mixture. This is in agreement with the almost equal amounts of surface-anchored amino groups in the functionalized MCM-41 samples (Tab. 2).

The distribution of amino groups on mesoporous silica can be imaged by CLSM after fluorescent labeling, provided that the particles are large and of well defined morphology.[9] ASNCs are ideal for this purpose. The pore openings of the ASNCs are located at the hexagonal bases and the channels run parallel to the long axis of the particles.[19] Fig. 3 shows CLSM images of APTES-functionalized ASNCs after labeling with fluorescein isothiocyanate (FITC). Particles functionalized in the presence of an amount of water equivalent to one monolayer show only minor differences compared to particles prepared under dry conditions. Despite the fact that particles with spatially non-uniform luminescence can be found (e.g. particle #3 of A-1, Fig. 3), clustering of APTES is obviously not sufficiently severe to cause inhomogeneities that are detectable with our CLSM setup. However, increasing the amount of water to two monolayers clearly causes an accumulation of labeled amino groups at the pore entrances. We can conclude that in this case, clustering of APTES in the channels leads to pore blocking. It should be noted that based on the CLSM images of A-2, we cannot exclude the presence of amino groups in the center of the channels, as they might have been rendered inaccessible for FITC labeling. However, taking into consideration the results of the analysis by nitrogen sorption, there is evidence for a pronounced gradient of the density of grafted amino groups, with higher density at the channel entrances and scarcely functionalized channel centers. The observation that A-2 binds less FITC than A-1 and A-0 (Tab. 2) can be explained by the presence of closely spaced amino groups and partial pore blocking in A-2.

An interesting question that needs to be considered is whether water adsorbed in the channels could hinder the penetration of APTES. Assuming that this would be the case, we would expect to see a non-uniform distribution of labeled amino groups even for low amino contents. However, Fig. 3 (sample A-0.1-2) shows that a reduction of the amino content leads to an uniform distribution of the coupled FITC labels, even in the presence of water. In fact, it seems that at

this low APTES concentration, clusters cannot grow large enough to significantly affect the diffusion of FITC through the channels.

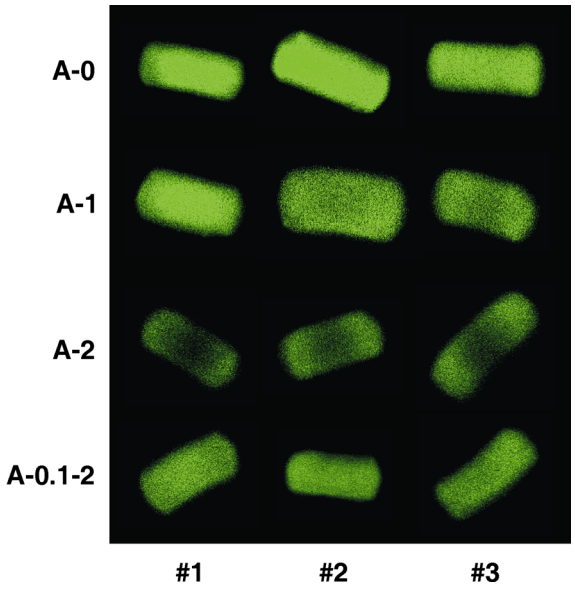

Figure 3. CLSM images of ASNCs after functionalization with APTES in toluene under dry conditions (A-0), and in the presence of water equivalent to one (A-1) or two (A-2) monolayers. Sample A-0.1-2 was prepared in the presence of an amount of water equivalent to two monolayers, but with a four times lower amino content. Three particles are shown for each reaction condition. Optical slices in the center of the particles were selected. The length of the particles is approximately 5 µm.

Based on the CLSM images given for samples A-0, A-1, and A-2, one could further speculate that an increased reactivity of APTES in the presence of water leads to preferential grafting to the most accessible sites, namely those on the external particle surface and on the pore surface close to the channel entrances. Such a hypothesis is largely based on the observation that the silanol groups of the hydrolyzed silanes react faster with the silica surface than the alkoxysilane groups.[20,21] Considering the uniform functional group distribution obtained for sample A-0.1-2, we can, however, exclude this possibility.

The combination of nitrogen sorption and CLSM imaging for the analysis of fluorescence-labeled functionalized mesoporous silica provides insights into the parameters that govern the distribution of the grafted functional groups. While we have focused on the role of water in the deposition of APTES from toluene, a variety of further parameters, such as solvent polarity, temperature, or the presence of co-adsorbed species other than water, can be thought of in terms of their influence on the grafting process. From the present study, we can conclude that clustering of APTES in mesopores is promoted by the presence of water and eventually leads to pore blocking and non-uniform distributions of functional groups with higher grafting densities at the pore entrances. Clustering of organosilanes on the pore surface close to the pore openings is a process that is not desirable for most applications of functionalized mesoporous silica. There are, however, instances where a high local concentration of cross-linked organosilanes at the pore entrances might in fact be useful. Mesoporous silica based drug delivery devices often require the functionalization of the pore entrances to install a gating mechanism.[22–24] Having multiple, closely spaced anchoring points with some degree of vertical polymerization might facilitate the stable attachment of the gatekeepers.

Experimental Methods

MCM-41 was synthesized as described in reference 12. Arrays of silica nanochannels (ASNCs) were prepared according to a method reported by Kievsky and Sokolov.[16] Samples were stored at 80 °C after calcination. Postsynthetic modification was performed as follows: Calcined mesoporous silica was dispersed in dry toluene (containing less than 0.005 % of H_2O, Fluka, puriss., absolute, stored over molecular sieve). After a few seconds of ultrasonication, a calculated amount of deionized H_2O was added and the suspension was again briefly ultrasonicated before being stirred for 1 h at room temperature. Finally, 0.10 or 0.40 mmol of 3-aminopropyltriethoxysilane (APTES, Fluka, ≥ 98.0 %) per gram of silica was added, and the mixture was stirred for 3 h at 80 °C. The product was recovered by filtration, washed with ethanol, and dried in a vacuum. Labeling with fluorescein 5-isothiocyanate (FITC, Fluka, ≥ 97.5 %) was carried out according to reference 12, with a coupling time of 24 h at room temperature (in absolute ethanol).

The amount of surface-grafted amino groups was analyzed by the fluorogenic derivatization reaction with fluorescamine.[25] In the investigated range of amino contents, the average relative error of this analysis method is typically below 10 %.[13] The

amount of coupled fluorescein was determined by dissolving the sample in a 0.2 M aqueous solution of NaOH and measuring the UV-vis absorption spectrum of the resulting clear solution. An extinction coefficient of 75000 $M^{-1}cm^{-1}$ (at λ_{max} = 490 nm) was used for the calculations.[13] Nitrogen sorption isotherms were collected at 77 K using a Quantachrome NOVA 2200. Samples were vacuum-degassed at 80 °C for 3 h. The total surface area S_{BET} was obtained using the standard BET method for adsorption data in a relative pressure range from 0.05 to 0.20.[26] The total pore volume V_{tot} was calculated from the amount of nitrogen adsorbed at a relative pressure of 0.95. The external surface area S_{Ext} was determined from the linear part of the α_S-plot ($\alpha_S > 1$).[27] Mesopore size distributions of the functionalized samples were evaluated from the desorption branches of the nitrogen isotherms by means of the BJH method.[28] All MCM-41 samples exhibited type IV isotherms, and condensation in the primary mesopores was not accompanied by hysteresis. The average pore diameter and pore size distribution of the parent materials was calculated from the respective adsorption isotherms by means of a NLDFT model developed for silica exhibiting cylindrical pore geometry (NOVAWin2 software, Version 2.2, Quantachrome Instruments).[29] Scanning electron microscopy images were acquired on a JEOL JSM-6060. The CLSM setup consisted of a Olympus BX 60 microscope with a FluoView confocal unit. The FITC-labeled samples were excited at 488 nm.

Acknowledgment. Financial support was provided by the European Commission through the Human Potential Program (Marie-Curie RTN Nanomatch, Grant No. MRTN-CT-2006-035884) and by the Swiss National Science Foundation (Project 200020-117591).

References

1. Balas, F.; Manzano, M.; Horcajada, P.; Vallet-Regi, M. Confinement and Controlled Release of Bisphosphonates on Ordered Mesoporous Silica-Based Materials. *J. Am. Chem. Soc.* **2006**, *128*, 8116-8117.
2. Sharma, K. K.; Anan, A.; Buckley, R. P.; Ouellette, W.; Asefa, T. Toward Efficient Nanoporous Catalysts: Controlling Site-Isolation and Concentration of Grafted Catalytic Sites on Nanoporous Materials with Solvents and Colorimetric Elucidation of Their Site-Isolation. *J. Am. Chem. Soc.* **2008**, *130*, 218-228.
3. Sharma, K. K.; Asefa, T. Efficient Bifunctional Nanocatalysts by Simple Postgrafting of Spatially Isolated Catalytic Groups on Mesoporous Materials. *Angew. Chem. Int. Ed.* **2007**, *46*, 2879-2882.
4. Wang, X.; Lin, K. S. K.; Chan, J. C. C.; Cheng, S. Direct Synthesis and Catalytic Applications of Ordered Large Pore Aminopropyl-Functionalized SBA-15 Mesoporous Materials. *J. Phys. Chem. B* **2005**, *109*, 1763-1769.
5. Macquarrie, D. J.; Jackson, D. B. Aminopropylated MCMs as Base Catalysts: A Comparison with Aminopropylated Silica. *Chem. Commun.* **1997**, 1781-1782.
6. Cauvel, A.; Renard, G.; Brunel, D. Monoglyceride Synthesis by Heterogeneous Catalysis Using MCM-41 Type Silicas Functionalized with Amino Groups. *J. Org. Chem.* **1997**, *62*, 749-751.
7. Liu, A. M.; Hidajat, K.; Kawi, S.; Zhao, D. Y. A New Class of Hybrid Mesoporous Materials with Functionalized Organic Monolayers for Selective Adsorption of Heavy Metal Ions. *Chem. Commun.* **2000**, 1145-1146.
8. Han, Y.-J.; Stucky, G. D.; Butler, A. Mesoporous Silicate Sequestration and Release of Proteins. *J. Am. Chem. Soc.* **1999**, *121*, 9897-9898.
9. Gartmann, N.; Brühwiler, D. Controlling and Imaging the Functional-Group Distribution on Mesoporous Silica. *Angew. Chem. Int. Ed.* **2009**, *48*, 6354-6356.
10. Vrancken, K. C.; Van Der Voort, P.; Gillis-D'Hamers, I.; Vansant, E. F.; Grobet, P. Influence of Water in the Reaction of γ-aminopropyltriethoxysilane with Silica Gel. A Fourier-Transform Infrared and Cross-Polarisation Magic-Angle-Spinning Nuclear Magnetic Resonance Study. *J. Chem. Soc., Faraday Trans.* **1992**, *88*, 3197-3200.
11. Kallury, K. M. R.; Macdonald, P. M.; Thompson, M. Effect of Surface Water and Base Catalysis on the Silanization of Silica by (Aminopropyl)alkoxysilanes Studied by X-ray Photoelectron Spectroscopy and ^{13}C Cross-Polarization/Magic Angle Spinning Nuclear Magnetic Resonance. *Langmuir* **1994**, *10*, 492-499.
12. Salmio, H.; Brühwiler, D. Distribution of Amino Groups on a Mesoporous Silica Surface after Submonolayer Deposition of Aminopropylsilanes from an Anhydrous Liquid Phase. *J. Phys. Chem. C* **2007**, *111*, 923-929.
13. Ritter, H.; Brühwiler, D. Accessibility of Amino Groups in Postsynthetically Modified Mesoporous Silica. *J. Phys. Chem. C* **2009**, *113*, 10667-10674.
14. Megelski, S.; Lieb, A.; Pauchard, M.; Drechsler, A.; Glaus, S.; Debus, C.; Meixner, A. J.; Calzaferri, G. Orientation of Fluorescent Dyes in the Nano Channels of Zeolite L. *J. Phys. Chem. B* **2001**, *105*, 25-35.
15. Pauchard, M.; Huber, S.; Méallet-Renault, R.; Maas, H.; Pansu, R.; Calzaferri, G. Time- and Space-Resolved Luminescence of a Photonic Dye–Zeolite Antenna. *Angew. Chem. Int. Ed.* **2001**, *40*, 2839-2842.
16. Kievsky, Y.; Sokolov, I. Self-Assembly of Uniform Nanoporous Silica Fibers. *IEEE Trans. Nanotechnol.* **2005**, *4*, 490-494.
17. Baker, F. S.; Sing, K. S. W. Specificity in the Adsorption of Nitrogen and Water on Hydroxylated and Dehydroxylated Silicas. *J. Colloid Interface Sci.* **1976**, *55*, 605-613.

18. Caravajal, G. S.; Leyden, D. E.; Quinting, G. R.; Maciel, G. E. Structural Characterization of (3-Aminopropyl)-triethoxysilane-Modified Silicas by Silicon-29 and Carbon-13 Nuclear Magnetic Resonance. *Anal. Chem.* **1988**, *60*, 1776-1786.
19. Kievsky, Y. Y.; Carey, B.; Naik, S.; Mangan, N.; ben-Avraham, D.; Sokolov, I. Dynamics of Molecular Diffusion of Rhodamine 6G in Silica Nanochannels. *J. Chem. Phys.* **2008**, *128*, 151102.
20. Assink, R. A.; Kay, B. D. Sol-Gel Kinetics. I. Functional Group Kinetics. *J. Non-Cryst. Sol.* **1988**, *99*, 359-370.
21. Luechinger, M.; Prins, R.; Pirngruber, G. D. Functionalization of Silica Surfaces with Mixtures of 3-aminopropyl and Methyl Groups. *Microporous Mesoporous Mater.* **2005**, *85*, 111-118.
22. Mal, N. K.; Fujiwara, M.; Tanaka, Y. Photocontrolled Reversible Release of Guest Molecules from Coumarin-modified Mesoporous Silica. *Nature* **2003**, *421*, 350-353.
23. Lai, C.-Y.; Trewyn, B. G.; Jeftinija, D. M.; Jeftinija, K.; Xu, S.; Jeftinija, S.; Lin, V. S.-Y. A Mesoporous Silica Nanosphere-Based Carrier System with Chemically Removable CdS Nanoparticle Caps for Stimuli-Responsive Controlled Release of Neurotransmitters and Drug Molecules. *J. Am. Chem. Soc.* **2003**, *125*, 4451-4459.
24. Hernandez, R.; Tseng, H.-R.; Wong, J. W.; Stoddart, J. F.; Zink, J. I. An Operational Supramolecular Nanovalve. *J. Am. Chem. Soc.* **2004**, *126*, 3370-3371.
25. Ritter, H.; Nieminen, M.; Karppinen, M.; Brühwiler, D. A Comparative Study of the Functionalization of Mesoporous Silica MCM-41 by Deposition of 3-aminopropyltrimethoxysilane from Toluene and from the Vapor Phase. *Microporous Mesoporous Mater.* **2009**, *121*, 79-83.
26. Brunauer, S.; Emmett, P. H.; Teller, E. Adsorption of Gases in Multimolecular Layers. *J. Am. Chem. Soc.* **1938**, *60*, 309-319.
27. Kruk, M.; Jaroniec, M.; Ryoo, R.; Kim, J. M. Monitoring of the Structure of Siliceous Mesoporous Molecular Sieves Tailored Using Different Synthesis Conditions. *Microporous Mater.* **1997**, *12*, 93-106.
28. Barrett, E. P.; Joyner, L. G.; Halenda, P. P. The Determination of Pore Volume and Area Distributions in Porous Substances. I. Computations from Nitrogen Isotherms. *J. Am. Chem. Soc.* **1951**, *73*, 373-380.
29. Ravikovitch, P. I.; Domhnaill, S. C. O.; Neimark, A. V.; Schüth, F.; Unger, K. K. Capillary Hysteresis in Nanopores: Theoretical and Experimental Studies of Nitrogen Adsorption on MCM-41. *Langmuir* **1995**, *11*, 4765-4772.

8. Publication G

Direct synthesis and fluorescent imaging of bifunctionalized mesoporous iodopropyl-silica

Jan H. Ramm, Nando Gartmann, Dominik Brühwiler*

Institute of Inorganic Chemistry, University of Zurich, Winterthurerstrasse 190, 8057 Zurich, Switzerland

J. Colloid Interf. Sci. 345 (2010) 200 – 205

Abstract. The co-condensation of 3-iodopropyltrimethoxysilane and tetraethoxysilane with an additional substituted trimethoxysilane (RTMS) in the presence of Pluronic P123 and hydrogen iodide yields bifunctionalized mesoporous silica. The pore size distribution of these materials depends on the nature of the RTMS additive. Excellent results in terms of a narrow pore size distribution were obtained with methyltrimethoxysilane. A particularly interesting bifunctionalized mesoporous material is formed by the co-inclusion of iodopropyl and aminopropyl moieties. The complementary reactivity of these two functional groups is demonstrated by the selective labeling of the amino-iodo-functionalized mesoporous silica with 2-hydroxy substituted nile red and fluorescein isothiocyanate, allowing further characterization of the functional group distribution by confocal laser scanning microscopy.

G.1. Introduction

Bifunctionalized mesoporous silica has recently attracted increased interest in the fields of catalysis [1], adsorption [2], and sensing [3]. A variety of functional group pairs have been explored, including sulfonic acid/amino [1d], sulfonic acid/mercapto [1e], amino/-carboxyl [4], mercapto/acetyl-acetonato [5], and amino/phenyl [6]. Among the many functional groups that have been incorporated into mesoporous silica, the iodopropyl group stands out as a particularly interesting option in terms of the intriguing possibilities for further modification by means of nucleophilic substitution. Alauzun et al. have shown that the direct synthesis of iodopropyl-functionalized SBA-15 type materials is successful if HCl is replaced by HI to avoid the formation of chloropropyl groups [7]. Based on this procedure, we have investigated the direct synthesis of bifunctionalized mesoporous silica containing iodopropyl as primary functional group. Additional organic groups can for example be envisaged to provide pores with increased hydrophobicity, which for many applications, including catalysis, sensing, low *k* dielectrics, and drug delivery, might be more desirable than the environment created by the abundant surface hydroxyl groups common to mesoporous silica based materials after removal of the respective structure-directing agent (SDA) [8]. On the other hand, the presence of surface groups with complementary reactivity, such as iodopropyl and aminopropyl, is expected to facilitate further modification towards multifunctionalized materials.

The inclusion of functional groups into mesoporous silica is most conveniently accomplished by a co-condensation approach (also referred to as *direct synthesis* or *one-pot synthesis*), as postsynthetic modification often leads to a preferential functionalization of the most accessible sites (external surface and pore entrances) [9,10]. However, the quality of the porous inorganic-organic hybrid materials resulting from co-condensation depends on the nature of the respective alkoxysilane precursors. Having an organic group that is sufficiently hydrophobic to interact with the core of the micelles is often advantageous.

Obtaining information on the distribution of the functional groups is a key issue in the synthesis of functionalized mesoporous silicas. Confocal laser scanning microscopy (CLSM) offers intriguing possibilities in this regard, and has already been successfully applied to zeolites [11] and mesoporous silicas [12] containing luminescent guests, as well as for determining the distribution of aminopropyl moieties after postsynthetic modification [9]. In order to apply CLSM to bifunctionalized mesoporous silica, 3-iodopropyltrimethoxysilane (IPTMS) was co-condensed with 3-aminopropyltrimethoxysilane (APTMS). This results in a material containing functional groups that can be labeled independently with fluorescent moieties.

G.2. Materials and methods

G.2.1. Synthesis of bifunctionalized mesoporous iodopropyl-silica

The preparation of mesoporous silica containing iodopropyl groups and additional organic moieties is derived from the synthesis of iodopropyl-functionalized mesoporous silica reported by Alauzun et al. [7]. Briefly, an amount of 2.00 g of Pluronic P123 ($EO_{20}PO_{70}EO_{20}$, M_{av} = 5800, Aldrich) was dissolved in 80 mL of H_2O containing 0.58 mL of aqueous HI (55–58 %, Fluka). This solution was added to a mixture containing 4.75 mL (21 mmol) of tetraethoxysilane (TEOS, Fluka, ≥ 99 %), 29.6 µL (0.15 mmol) or 220 µL (1.12 mmol) of 3-iodopropyltrimethoxysilane (IPTMS, ABCR Karlsruhe), and a specific amount of an additional substituted trimethoxysilane RTMS (Table 1). The mixture was stirred at room temperature for 90 min. After heating to 60 °C, 0.04 g of NaF was added, and the mixture was stirred for 72 h at 60 °C. The product was recovered by filtration. After washing with 200 mL of acetone, the SDA was removed by Soxhlet extraction with ethanol over a period of 24 h. The resulting white solid was oven-dried at 60 °C, yielding typically around 1.4 g of product. Particles with irregular morphology and sizes ranging from 2 µm to larger aggregates of ca. 50 µm were obtained. Methyltrimethoxysilane (Aldrich, ≥ 98 %), phenyltrimethoxysilane (Aldrich, 97 %), octyltrimethoxysilane (Aldrich, 96 %), octadecyltrimethoxysilane (Aldrich, ≥ 90 %), 3-aminopropyltrimethoxysilane (Fluka, ≥ 97 %), and isobutyltrimethoxysilane (ABCR Karlsruhe, 97 %) were used as received.

G.2.2. Synthesis and coupling of 2-hydroxy substituted nile red

G.2.2.1. 5-Diethylamino-2-nitrosophenol (DNP)

An amount of 3.36 g (20 mmol) of 3-diethylaminophenol (Aldrich, 97 %) was dissolved in 8 mL of 32 % aqueous HCl and 20 g of ice. A solution of 1.68 g (24 mmol) of $NaNO_2$ in 6 mL of water was added dropwise (during 1 h) to the above solution and the temperature was kept between 0 and 5 °C. The result-

ing brown slurry was stirred for 2 h. Following filtration and washing with 10 mL of 4 M aqueous HCl, the product was dried under vacuum and recrystallized with 150 mL of ethanol. After addition of 20 mL of diethylether, the suspension was cooled to 0 °C and kept over night for crystallization. The precipitate was filtered, washed with a few milliliters of ethanol and dried under vacuum yielding 3.33 g (14 mmol, 71 %) of a yellow product (DNP hydrochloride). The DNP hydrochloride can be converted to the free compound by diluting in 100 mL of 0.1 M aqueous $NaHCO_3$, followed by an extraction with 100 mL and two times 50 mL of dichloromethane, with subsequent drying of the organic phase over Na_2SO_4. ^{13}C NMR (400 MHz, [$^2H_6$]DMSO): δ = 169.6, 158.0, 150.1, 135.4 (CH), 116.3 (CH), 96.0 (CH), 46.5 (NCH_2CH_3), 14.9 (NCH_2-CH_3). ^1H NMR (400 MHz, [$^2H_6$]DMSO): δ = 7.32 (1H, d, J = 10 Hz), 6.90–6.87 (1H, m), 5.74 (1H, d, J = 3 Hz), 3.60–3.58 (4H, m), 1.20 (6H, t, J = 7.2 Hz). IR (KBr)/cm^{-1}: 2980, 2937, 1629, 1514.

G.2.2.2. 9-Diethylamino-2-hydroxy-5H-benzo[a]-phenoxazin-5-one (NR–OH)

2-Hydroxy substituted nile red (NR–OH), which we use as a fluorescent label for the co-condensed iodopropyl groups, was synthesized according to reference 13. Briefly, DNP hydrochloride (1.28 g, 5.5 mmol) and 1,6-dihydroxy-naphthalene (0.90 g, 5.6 mmol, ABCR Karlsruhe, 97 %) were dissolved in dry DMF and heated for 4 h under reflux. The solvent was removed under reduced pressure to yield a dark blue-green solid. Subsequent purification by column chromatography (ethyl acetate/isopropanol 4:1) resulted in 0.66 g (2.0 mmol, 36 %) of a dark brown solid. ^{13}C NMR (500 MHz, [$^2H_6$]DMSO): δ = 182.5 (CO), 161.5, 152.5, 151.6, 147.3, 139.6, 134.6, 131.7 (CH), 128.3 (CH), 124.8, 119.3 (CH), 110.8 (CH), 109.0 (CH), 105.0 (CH), 97.0 (CH), 45.3 (NCH_2CH_3), 13.3 (NCH_2CH_3). ^1H NMR (500 MHz, [$^2H_6$]DMSO): δ = 10.41 (1H, s), 7.98 (1H, d, J = 8.5 Hz), 7.89 (1H, d, J = 2 Hz), 7.59 (1H, d, J = 9.5 Hz), 7.10 (1H, dd, J = 8.5 Hz and 2.5 Hz), 6.82 (1H, dd, J = 9 Hz and 2.5 Hz), 6.64 (1H, s, J = 2.5 Hz), 6.15 (1H, s), 3.52 (4H, q, J = 7 Hz), 1.18 (6H, t, J = 7 Hz).

Table 1. Structural properties of the functionalized samples

Sample	R	n(IPTMS) [mmol]	n(RTMS) [mmol]	n(I)[a] [mmol/g]	n(R)[b] [mmol/g]	d_{BJH}[c] [nm]	S_{BET}[d] [m^2/g]	C_{BET}	V_{tot}[e] [cm^3/g]
Ip	–	0.15	0	0.09	0	10.0	832	95	1.65
Ip/Me	methyl	0.15	1.5	0.09	0.83	10.2	862	79	1.27
Ip/iBu	isobutyl	0.15	1.5	0.07	1.16	5.8	1057	61	0.94
Ip/Ph	phenyl	0.15	1.5	0.08	1.06	6.0	1010	76	0.82
Ip/Oc	octyl	0.15	1.5	0.06	0.66	–	798	56	1.07
Ip/Od	octadecyl	0.15	1.5	0.05	0.73	9.1	503	63	0.93
Ip-1.1	–	1.12	0	0.53	0	6.7	865	83	0.84
Ip-1.1/Me	methyl	1.12	1.5	0.53	0.52	5.9	969	62	0.95
Ip/Ap	3-aminopropyl	0.15	0.15	0.09	0.09	10.8	702	76	1.57

[a] Iodine content from elemental analysis
[b] Est. from the C content obtained from elemental analysis (in case of Ip/Ap, the N content was used instead)
[c] Average pore diameter calculated from the adsorption isotherm by the BJH method
[d] Total BET surface area
[e] Total pore volume (calculated at p/p_0 = 0.98)

G.2.2.3. Coupling of NR–OH to iodopropyl groups

Functionalized mesoporous silica (250 mg) was dispersed in 5 mL of dry DMF and 20 mg (60 µmol) of NR–OH was added. After the addition of 45 mg of K_2CO_3, the mixture was stirred under nitrogen for 24 h at room temperature. The product was recovered by centrifugation and washed with 100 mL of 0.1 M aqueous HCl. The silica was subsequently dispersed in 20 mL of water for 10 min and recovered by centrifugation. This step was repeated until the washing solution had a pH above 6 (typically requiring three washing steps). After a final washing with 100 mL of ethanol, the samples were Soxhlet extracted with ethanol and dried at 60 °C.

The amount of coupled NR–OH was determined by dissolving 10–20 mg of the dry sample in 20 mL of 0.1 M NaOH (in ethanol/water 1:1) and measuring the UV-Vis absorption spectrum of the resulting solution (ε_{max} = 22000 $M^{-1}cm^{-1}$).

G.2.3. Coupling of fluorescein isothiocyanate

Labeling of the amino groups in iodopropyl-aminopropyl-functionalized mesoporous silica was accomplished as follows: A calculated amount of fluorescein isothiocyanate (FITC, Fluka, isomer I, ≥ 97.5 %, 1.5-fold excess relative to the amount of amino groups) was dissolved in 25 mL of absolute ethanol. After the addition of 80 mg of functionalized mesoporous silica, the suspension was stirred for 24 h at room temperature. The labeled product was recovered by filtration, washed with ethanol, and dried at 80 °C.

The amount of coupled FITC was determined by dissolving 15–30 mg of the sample in 25 mL of 0.2 M aqueous NaOH and measuring the UV-Vis absorption spectrum of the solution (ε_{max} = 75000 $M^{-1}cm^{-1}$) [14].

G.2.4. Characterization

Nitrogen sorption isotherms were collected at 77 K with a Quantachrome NOVA 2200. Samples were vacuum-degassed at 80 °C for 3 h. Mesopore size distributions were evaluated from the adsorption branches of the nitrogen isotherms by means of the BJH method [15]. The total surface area S_{BET} was calculated by the BET method [16]. The total pore volume V_{tot} was determined from the amount of nitrogen adsorbed at a relative pressure of 0.98. Photoluminescence spectra were recorded with a Perkin-Elmer LS50B spectrofluorometer equipped with a front surface accessory for the measurement of powdered samples. UV-Vis absorption spectra were measured in ethyl benzoate as an index-matching solvent (n = 1.504). Elemental (CHN) analysis of the mesoporous materials was performed with a LECO CHNS-932. The iodine content of the samples was analyzed following a Schöniger digestion [17]. Scanning electron microscopy images were acquired on a JEOL JSM-6060. The confocal laser scanning microscopy setup consisted of an Olympus BX 60 microscope equipped with a FluoView confocal unit and lasers operating at 488 (Ar ion) and 543.5 nm (He/Ne).

G.3. Results and discussion

G.3.1. General observations

The nitrogen sorption isotherms of samples synthesized with an IPTMS/RTMS ratio of 1:10 are shown in Figure 1. The corresponding pore size distributions (PSDs) are given in Figure 2 with additional characterization data compiled in Table 1. Comparison with the monofunctionalized sample (Ip) reveals that the addition of methyltrimethoxysilane (MTMS) to the synthesis mixture does not cause a significant change in the porosity of the material (Ip/Me). The course of the respective adsorption isotherm at a relative pressure above 0.80 even suggests that Ip/Me features less textural porosity. This observation is supported by the pore volumes calculated at relative pressures of 0.98 and 0.80. In the case of Ip/Me, the total pore volume V_{tot} (p/p_0 = 0.98) is 1.27 cm^3/g, whereas $V_{0.80}$ (p/p_0 = 0.80) amounts to 1.02 cm^3/g. For Ip, the difference between these two values is significantly larger (V_{tot} = 1.65 cm^3/g, $V_{0.80}$ = 0.86 cm^3/g). The presence of the methyl groups in Ip/Me furthermore leads to a decrease of the C_{BET} value (Table 1). The C_{BET} parameter is related to the energy of interaction of nitrogen with the surface and is therefore a rough estimate for the polarity. C_{BET} values close to 100 are characteristic of hydroxylated silica surfaces, whereas modification with hydrophobic groups generally reduces C_{BET} [18].

Compared to Ip and Ip/Me, co-condensation of IPTMS with isobutyltrimethoxysilane or phenyltrimethoxysilane produced samples with smaller pore diameter (Ip/iBu and Ip/Ph) and, particularly in the case of Ip/Ph, a less defined PSD. Interestingly, the sample synthesized with octyltrimethoxysilane (Ip/Oc) does not possess defined mesopores, whereas the sample prepared with octadecyltrimethoxysilane (Ip/Od) features a comparatively well-defined PSD with a maximum at 9.1 nm. It seems that the interaction of the SDA with octadecyl chains is more favorable for the

formation of a defined pore structure than the interaction with the shorter octyl chains. Irrespective of the employed RTMS, C_{BET} values are lower than for the sample synthesized in the absence of a RTMS additive. This is in agreement with the presence of hydrophobic groups on the pore surface of the bifunctionalized samples.

The determination of the absolute amount of incorporated R moieties is complicated by a slight esterification of the silica surface upon extraction with ethanol [19] and the potential presence of residual SDA. The values given in Table 1 were therefore obtained by taking Ip as a reference. In accordance with the relative amounts of IPTMS and RTMS in the synthesis mixture, the n(R)/n(I) ratios in the final products are reasonably close to 10. More importantly, we can conclude that the presence of a RTMS additive does not cause a significant change of the amount of incorporated iodopropyl moieties. In all cases, scanning electron microscopy images showed particles with irregular morphology and sizes ranging from 2 µm to larger aggregates of ca. 50 µm.

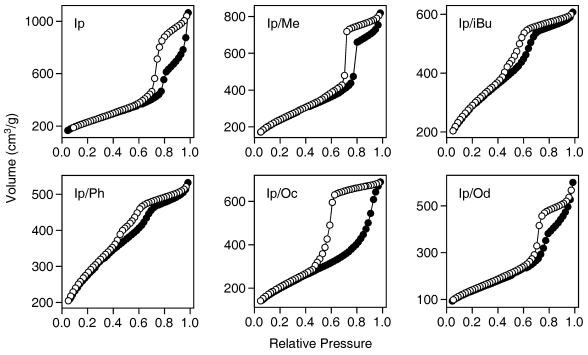

Figure 1. Nitrogen adsorption (●) and desorption isotherms (○) of mesoporous iodopropyl-silica (Ip) and of bifunctionalized mesoporous iodopropyl-silica.

G.3.2. High iodopropyl content

In terms of the PSD, the best results were obtained with MTMS as an additive (Figure 2). We have therefore conducted the same synthesis with an increased amount of IPTMS (samples Ip-1.1 and Ip-1.1/Me). The 7.5-fold increase of the IPTMS concentration led to a substantially smaller pore size (Figure 3). Interestingly, the pore size difference between Ip-1.1 and Ip is retained after removal of the grafted iodopropyl moieties by calcination (550 °C, 16 h, Figure 4), thus indicating that the amount of IPTMS in the reaction mixture has a significant effect on the condensation of the silica framework.

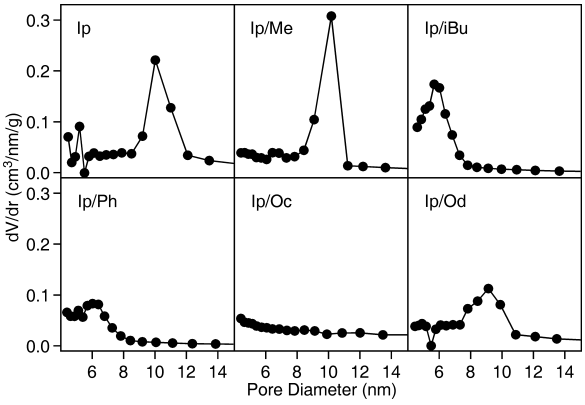

Figure 2. Pore size distributions of mesoporous iodopropyl-silica (Ip) and of bifunctionalized mesoporous iodopropyl-silica calculated from the adsorption isotherms shown in Figure 1.

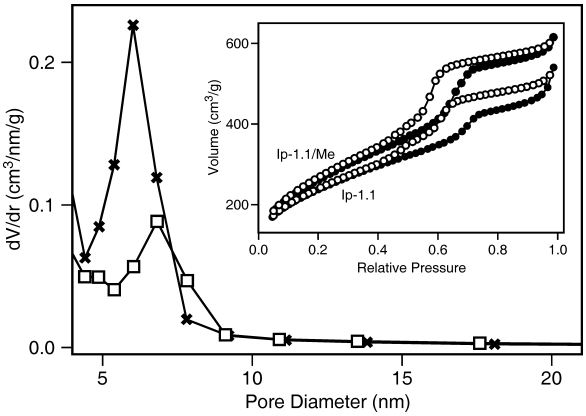

Figure 3. Pore size distributions of Ip-1.1 (1.12 mmol of IPTMS, □) and Ip-1.1/Me (1.12 mmol of IPTMS and 1.5 mmol of MTMS, ×). The corresponding nitrogen sorption isotherms are shown in the inset.

The bifunctionalized sample Ip-1.1/Me is superior to the monofunctionalized sample Ip-1.1 in terms of containing a minimum relative amount of textural porosity. This is in agreement with the results obtained from the corresponding samples synthesized with a smaller concentration of IPTMS (Ip and Ip/Me). Furthermore, the addition of MTMS obviously does not affect the incorporation of IPTMS into the silica framework, as indicated by the iodo contents of Ip-1.1 and Ip-1.1/Me (Table 1).

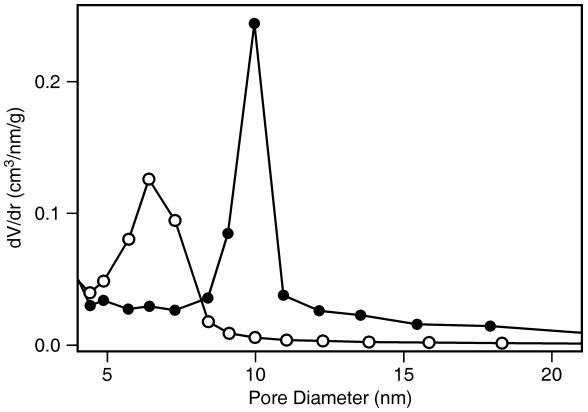

Figure 4. Pore size distribution of Ip-1.1 (○) and Ip (●) after removal of the iodopropyl moieties by calcination.

G.3.3. Fluorescent labeling and confocal laser scanning microscopy

The use of APTMS as an additional precursor offers possibilities for subsequent fluorescent labeling and for the analysis of the functional group distribution by CLSM. A narrow PSD is obtained when using 0.15 mmol of each IPTMS and APTMS (Figure 5). Similar to the materials synthesized with alkyltrimethoxysilanes, the iodo- and aminopropyl containing sample (Ip/Ap) features significant textural porosity, as evident from the hysteresis in the high pressure section of the nitrogen sorption isotherm (Figure 5, inset).

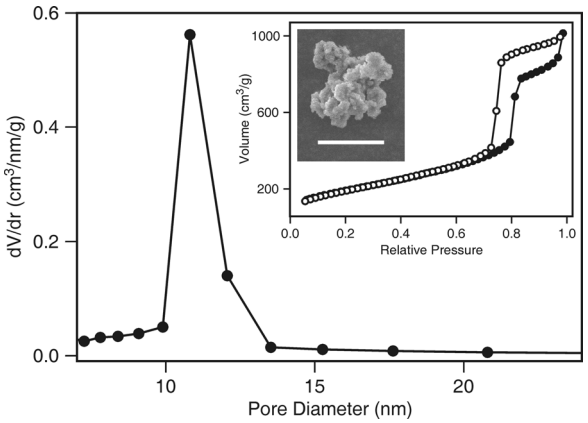

Figure 5. Pore size distribution of Ip/Ap. The corresponding nitrogen sorption isotherms are shown in the inset together with a scanning electron microscopy image of an Ip/Ap particle. The length of the scale bar is 10 µm.

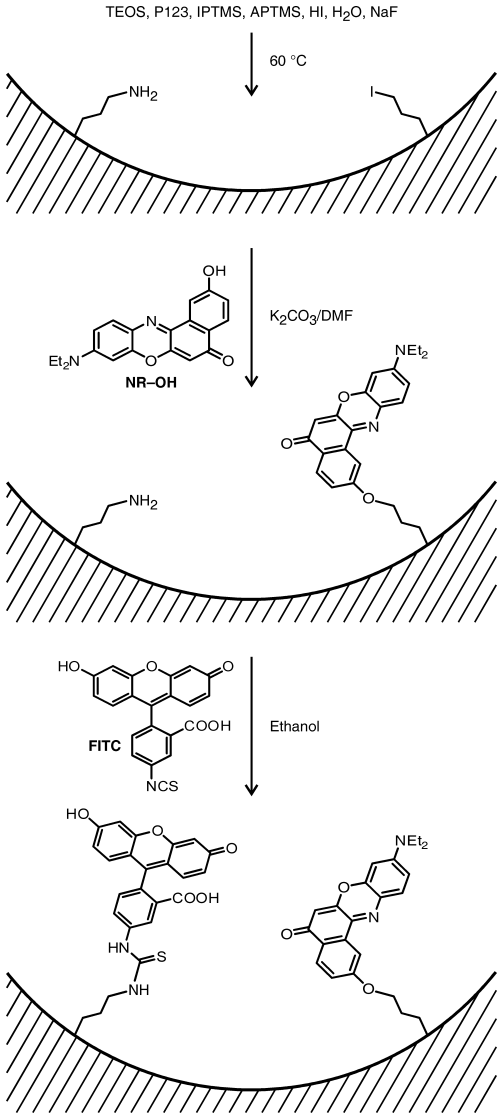

Figure 6. Labeling of iodopropyl-aminopropyl-functionalized mesoporous silica with 2-hydroxy substituted nile red (NR–OH) and fluorescein isothiocyanate (FITC).

The co-condensed iodopropyl and aminopropyl groups can be labeled selectively with NR–OH and FITC, respectively (Figure 6). No labeling was observed upon reaction of NR–OH with mesoporous silica containing only aminopropyl groups. FITC, on the other hand, did not bind to iodopropyl-silica in the absence of aminopropyl groups. However, the consecutive reaction of Ip/Ap with NR–OH and FITC yields a material containing both fluorescent labels. Analysis by UV-Vis spectroscopy revealed a nile red content of 5 µmol/g and a fluorescein content of 14 µmol/g. The absorption spectrum of the powdered

sample measured in an index-matching solvent (ethyl benzoate, Figure 7, bottom panel) features three maxima at 462, 488, and 537 nm, as well as a shoulder around 430 nm, corresponding well to the maxima found in the spectra of the materials containing only one of the labels (Figure 7, top panel). The occurrence of two maxima (and a short wavelength shoulder) in the absorption spectrum of coupled FITC indicates the presence of fluorescein moieties in different protonation states (dianion, monoanion, neutral) [20]. The luminescence spectrum of the FITC/NR–OH labeled sample (Figure 7, bottom panel) shows a comparatively weak luminescence of the coupled FITC. This can be attributed to the considerable overlap between the emission band of the FITC labels and the absorption band of the NR–OH labels, leading to radiative energy transfer. Assuming a homogeneous distribution of the fluorescent labels on the surface of Ip/Ap, a density of roughly 0.016 nm^{-2} is obtained, corresponding to one label per 60 nm^2. Additionally taking into account the fact that most of the surface of the material is concave, leading for example to situations where labels occupy sites on opposing channel walls, non-radiative energy transfer might contribute to the low luminescence intensity of the coupled FITC labels. Nonetheless, the intensity of the fluorescein emission is still sufficient for imaging by CLSM.

CLSM allows us to selectively image the fluorescein and nile red emission of the particles. A non-uniform spatial distribution of the luminescence intensity is usually a sign of a non-uniform distribution or insufficient accessibility of the incorporated functional groups [9,21]. The bifunctionalized mesoporous iodopropyl-silica particles are relatively large and feature irregular morphology. Observing optical slices at the center of such particles therefore provides representative information on the distribution of the fluorescent moieties. The spatial distribution of the coupled FITC (green) and coupled NR–OH (red) is very similar (Figure 8). This indicates that the distribution of the amino- and iodopropyl groups in Ip/Ap is uniform, as is commonly expected for co-condensed mesoporous silica samples. Furthermore, and maybe more importantly, amino- and iodopropyl groups located in the center of the particles are accessible. It is very likely that the relatively pronounced textural porosity of the samples contributes to the accessibility of the functional groups.

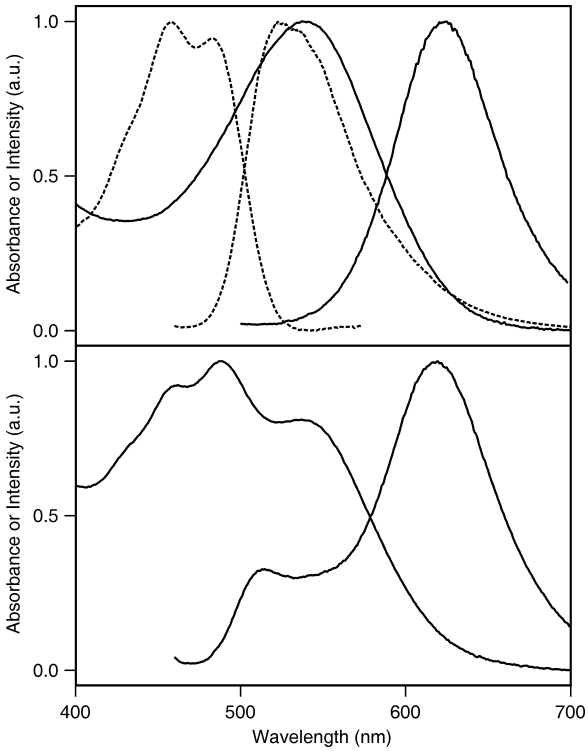

Figure 7. Absorption and luminescence spectra of Ip/Ap after either FITC labeling (dashed curves, top panel, excitation at 450 nm) or NR–OH labeling (solid curves, top panel, excitation at 490 nm). The bottom panel shows the absorption and luminescence spectra (excitation at 450 nm) of an Ip/Ap sample after labeling with NR–OH and FITC as schematically shown in Figure 6.

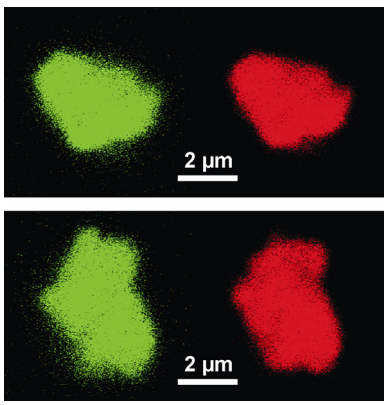

Figure 8. Confocal laser scanning microscopy images of two Ip/Ap particles after labeling with NR–OH and FITC. Excitation was performed at 488 and 543.5 nm. Optical slices in the center of the particles were selected. The left (green) images show the luminescence of the coupled FITC labels, whereas the right (red) images display the luminescence of coupled NR–OH.

G.4. Conclusions

IPTMS and RTMS can be co-condensed with TEOS in the presence of Pluronic P123 as a structure-directing agent to yield bifunctionalized mesoporous silica. The best results in terms of a narrow pore size distribution were obtained with R = methyl. As evident from the low C_{BET} values, the inclusion of alkyl moieties causes a change in surface properties, thus opening possibilities to tailor the environment of the iodopropyl sites. The co-inclusion of iodopropyl and aminopropyl groups is particularly interesting due to their complementary reactivity. Mesoporous silica providing iodo and amino groups as anchoring sites can serve as a starting material for the synthesis of mesoporous inorganic-organic hybrid materials with multiple functionality. Selective fluorescent labeling enables the imaging of the spatial distribution of the incorporated amino and iodo groups by confocal laser scanning microscopy. The results indicate that the organic moieties in bifunctionalized mesoporous iodopropyl-silica are uniformly distributed and that the porosity renders groups located in the center of the particles accessible.

Acknowledgments. Financial support was provided by the European Commission through the Human Potential Program (Marie-Curie RTN Nanomatch, Grant MRTN-CT-2006-035884) and by the Swiss National Science Foundation (Project 200020-117591).

References

[1] (a) S. Huh, H.-T. Chen, J.W. Wiench, M. Pruski, V.S.-Y. Lin, J. Am. Chem. Soc. 126 (2004) 1010; (b) S. Huh, H.-T. Chen, J.W. Wiench, M. Pruski, V.S.-Y. Lin, Angew. Chem. Int. Ed. 44 (2005) 1826; (c) I.K. Mbaraka, B.H. Shanks, J. Catal. 229 (2005) 365; (d) R.K. Zeidan, S.-J. Hwang, M.E. Davis, Angew. Chem. Int. Ed. 45 (2006) 6332; (e) E.L. Margelefsky, A. Bendjériou, R.K. Zeidan, V. Dufaud, M.E. Davis, J. Am. Chem. Soc. 130 (2008) 13442.

[2] T.-H. Kim, M. Jang, J.K. Park, Microporous Mesoporous Mater. 108 (2008) 22.

[3] (a) V.S.-Y. Lin, C.-Y. Lai, J. Huang, S.-A. Song, S. Xu, J. Am. Chem. Soc. 123 (2001) 11510; (b) M. Comes, M.D. Marcos, R. Martínez-Máñez, F. Sancenón, J. Soto, L.A. Villaescusa, P. Amorós, D. Beltrán, Adv. Mater. 16 (2004) 1783; (c) A.B. Descalzo, K. Rurack, H. Weisshoff, R. Martínez-Máñez, M.D. Marcos, P. Amorós, K. Hoffmann, J. Soto, J. Am. Chem. Soc. 127 (2005) 184.

[4] L. Han, J. Ruan, Y. Li, O. Terasaki, S. Che, Chem. Mater. 19 (2007) 2860.

[5] R. Mouawia, A. Mehdi, C. Reyé, R. Corriu, New J. Chem. 30 (2006) 1077.

[6] S.R. Hall, C.E. Fowler, B. Lebeau, S. Mann, Chem. Commun. (1999) 201.

[7] J. Alauzun, A. Mehdi, C. Reyé, R. Corriu, New J. Chem. 31 (2007) 911.

[8] (a) Y. Kuwahara, K. Maki, Y. Matsumara, T. Kamegawa, K. Mori, H. Yamashita, J. Phys. Chem. C 113 (2009) 1552; (b) Y. Zhu, T.E. Müller, J.A. Lercher, Adv. Funct. Mater. 18 (2008) 3427; (c) A.B. Descalzo, M.D. Marcos, C. Monte, R. Martínez-Máñez, K. Rurack, J. Mater. Chem. 17 (2007) 4716; (d) K. Inumaru, T. Ishihara, Y. Kamiya, T. Okuhara, S. Yamanaka, Angew. Chem. Int. Ed. 46 (2007) 7625; (e) J.A. Melero, J. Iglesias, J.M. Arsuaga, J. Sainz-Pardo, P. de Frutos, S. Blazquez, J. Mater. Chem. 17 (2007) 377; (f) J.C. Doadrio, E.M.B. Sousa, I. Izquierdo-Barba, A.L. Doadrio, J. Perez-Pariente, M. Vallet-Regí, J. Mater. Chem. 16 (2006) 462; (g) F. Omota, A.C. Dimian, A. Bliek, Appl. Catal. A, 294 (2005) 121; (h) A. Matsumoto, K. Tsutsumi, K. Schumacher, K.K. Unger, Langmuir 18 (2002) 4014; (i) A. Bhaumik, T. Tatsumi, Catal. Lett. 66 (2000) 181.

[9] N. Gartmann, D. Brühwiler, Angew. Chem. Int. Ed. 48 (2009) 6354.

[10] (a) T. Yokoi, H. Yoshitake, T. Tatsumi, J. Mater. Chem. 14 (2004) 951; (b) M.H. Lim, A. Stein, Chem. Mater. 11 (1999) 3285; (c) A. Stein, B.J. Melde, R.C. Schroden, Adv. Mater. 12 (2000) 1403; (d) F. Hoffmann, M. Cornelius, J. Morell, M. Fröba, Angew. Chem. Int. Ed. 45 (2006) 3216.

[11] (a) S. Megelski, A. Lieb, M. Pauchard, A. Drechsler, S. Glaus, C. Debus, A. J. Meixner, G. Calzaferri, J. Phys. Chem. B 105 (2001) 25; (b) M. Pauchard, S. Huber, R. Méallet-Renault, H. Maas, R. Pansu, G. Calzaferri, Angew. Chem. Int. Ed. 40 (2001) 2839.

[12] C. Seebacher, J. Rau, F.-W. Deeg, C. Bräuchle, S. Altmaier, R. Jäger, P. Behrens, Adv. Mater. 13 (2001) 1374.

[13] M.S.J. Briggs, I. Bruce, J.N. Miller, C.J. Moody, A.C. Simmonds, E. Swann, J. Chem. Soc., Perkin Trans. 1 (1997) 1051.

[14] H. Ritter, D. Brühwiler, J. Phys. Chem. C 113 (2009) 10667.

[15] E.P. Barrett, L.G. Joyner, P.P. Halenda, J. Am. Chem. Soc. 73 (1951) 373.

[16] S. Brunauer, P.H. Emmett, E. Teller, J. Am. Chem. Soc. 60 (1938) 309.

[17] W. Schöniger, Microchim. Acta 43 (1955) 123.

[18] (a) M.F. Ottaviani, A. Moscatelli, D. Desplantier-Giscard, F. Di Renzo, P.J. Kooyman, B. Alonso, A. Galarneau, J. Phys. Chem. B 108 (2004) 12123; (b) D. Brunel, A. Cauvel, F. Di Renzo, F. Fajula, B. Fubini, B. Onida, E. Garrone, New J. Chem. 24 (2000) 807; (c) L. Jelinek, E. Kováts, Langmuir 10 (1994) 4225.

[19] (a) C.C. Ballard, E.C. Broge, R.K. Iler, D.S. St. John, J.R. McWhorter, J. Phys. Chem. 65 (1961) 20; (b) T. Kimura, K. Kuroda, Y. Sugahara, K. Kuroda, J. Porous Mater. 5 (1998) 127.

[20] M.M. Martin, L. Lindqvist, J. Lumin. 10 (1975) 381.

[21] N. Gartmann, C. Schütze, H. Ritter, D. Brühwiler, J. Phys. Chem. Lett. 1 (2010) 379.

PART II

Dye-Zeolite Materials for Solar Energy Conversion Devices

Financial Support:
Swiss Commission of Technology and Innovation KTI/CTI (9231.2 PFNM-NM)
European Commission Marie-Curie RTN *Nanomatch* (MRTN-CT-2006-035884)

The following text is taken from the publication *Nanochannel Materials for Quantum Solar Energy Conversion Devices* (Dominik Brühwiler*, Le-Quyenh Dieu, and Gion Calzaferri, Chimia 61 (2007) 820) and serves as an introduction to the topic.

1. Introduction

1.1. General Concepts

The concept of organizing guest molecules in robust silicate-based porous solids is well established.[1] In this context, zeolites (pore diameter below 2 nm) are popular host materials, as their crystalline frameworks provide defined channel architectures[2] while being transparent from UV to near-infrared. One-dimensional channel systems are of particular interest, because the inclusion of chromophores can result in materials featuring optical anisotropy.[3] The molecular-sized channels offer possibilities to obtain high local concentrations of monomeric dyes. In such systems, electronic excitation energy is efficiently transported along the channels by means of Förster resonance energy transfer (FRET).[4] Furthermore, dyes in the channels are protected by the inert aluminosilicate framework, often leading to increased stability. The interplay of confinement and enhanced guest stability has been studied for specific cases.[5] Generally, it can be inferred that the penetration and diffusion of reactants is limited due to the steric constraints imposed by the guest-filled channels. In the following, we present two concepts outlining the potential use of dye-nanochannel inclusion compounds in quantum solar energy conversion devices.

1.2. Sensitization of Organic Solar Cells

Figure 1.1 illustrates the design of a nanochannel-based photonic antenna currently being investigated in our lab. Various zeolites featuring one-dimensional channel systems can in principle be used as host materials in such an assembly. Even mesoporous solids are interesting candidates, given the recent progress in the synthesis of ordered thin films with perpendicular orientation of the channels.[6] For guest molecules smaller than 7 Å (at least in two dimensions), zeolite L is an ideal choice. Crystals of zeolite L are typically cylindrical. Channels run through the entire crystal along the cylinder axis and are accessible through 7.1 Å windows located at the base surfaces (see Figure 1.2). A zeolite L crystal of 550 nm diameter provides approximately 80'000 parallel channels. Different crystal sizes ranging from 30 to 20'000 nm in length are feasible.[7] The aspect ratio can be tuned to a certain extent, affording disc-shaped or rod-shaped morphologies. A disc-shaped morphology is ideal for the preparation of zeolite L monolayers with the channels oriented perpendicular to the substrate surface.[8] A multitude of cationic and neutral dye molecules has been included into zeolite L

by cation exchange and adsorption from the gas phase, respectively.[1a] It was generally observed that dye molecules cannot pass each other once they are in the channels. Sequential introduction of different dye molecules therefore results in highly ordered materials featuring dye domains (Figure 1.1B). This allows for directed transport of electronic excitation energy along the channels. The energy transfer efficiency of a given donor-acceptor pair thereby depends on the relative orientation of the electronic transition dipole moments and the donor-acceptor distance. The latter should be minimal, but excluding π-interaction. For the optimization of FRET efficiency, dye molecules with bulky alkyl substituents are ideal. Such moieties are able to inhibit π-interactions by filling the intrachannel space between adjacent guest molecules.

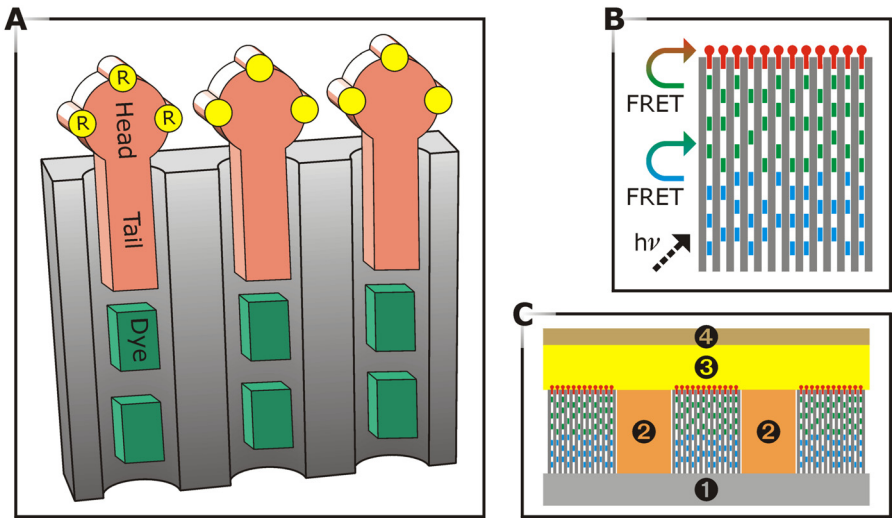

Figure 1.1. A) Schematic axial cut through channels containing dye molecules (green) and stopcocks (red) with intrinsic insulating groups (yellow). The channel length depends on the crystal size. B) Nanochannels containing two types of dye molecules (blue and green) and stopcocks (red). Light absorbed by the blue molecules travels to the stopcock heads by FRET via the green molecules. C) Integration of dye-stopcock-zeolite crystals into an organic solar cell (1: contacting oxide, 2: conducting polymer, 3: active material, 4: back contact).

A mediator is required to extract the electronic excitation energy that has reached the channel entrances via an energy transfer cascade (Figure 1.1B). This is accomplished by employing stopcock molecules, which are designed to specifically adsorb at the channel entrances, either by physisorption, electrostatic interaction or covalent bonding.[9] A stopcock molecule contains a tail that can enter the zeolite channel (Figure 1.1A). For maximum stability, this tail should carry a reactive group for coupling to amino-functionalized channel entrances.[10] The

chromophoric head, which is too large to enter the channels, figures as the acceptor for the electronic excitation energy. Large spectral overlap between donor emission and stopcock head absorption is crucial. Furthermore, parallel alignment of the electronic transition dipole moments of the included donor molecules and the stopcock heads should be provided to ensure efficient FRET. Once the energy has reached the stopcock heads, it is available for transfer to an external component, e.g., the active layer in an organic solar cell.[11] In order to prevent electron transfer, a thin insulating layer should be present between the stopcock heads and the active material. As an elegant solution, we propose to incorporate this insulating layer into the stopcock heads by means of suitable peripheral substituents (Figure 1.1A).[12]

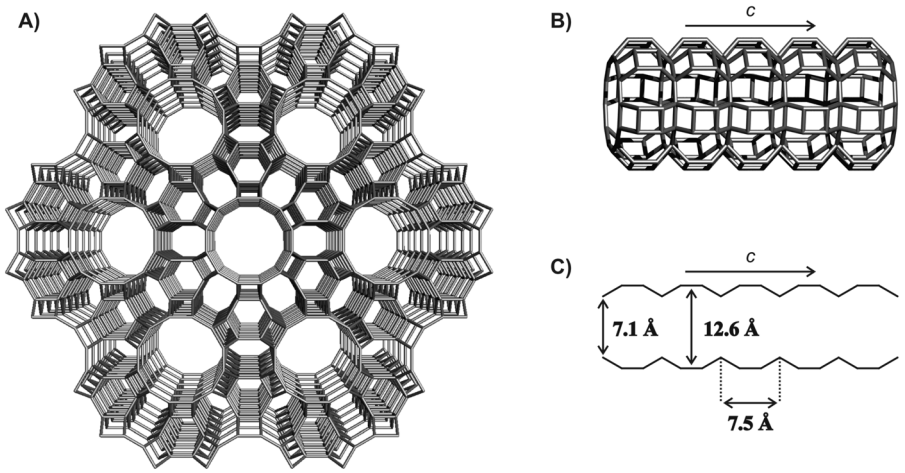

Figure 1.2. A) Zeolite L framework projected along the channel axis (c-axis). The lines represent oxygen bridges between Si and Si/Al. B) Side view of the main channel and C) its dimensions.

A possible solar cell design based on oriented monolayers of dye-stopcock-zeolite crystals is shown in Figure 1.1C. Charge transport is accomplished by a conducting polymer, such as PEDOT,[13] which is placed between the zeolite crystals. Consequently, the coat of a given cylindrical zeolite crystal is exposed to a different environment than its base. Recent results show that the coat and base surfaces of zeolite L can be functionalized independently,[14] thus allowing for an optimization of these various interfaces. The stopcock molecules are separated from the active material by intrinsic insulating groups, preventing electron transfer (Figure 1.1A). Zinc phthalocyanine (ZnPc) is an example of a suitable active material for such a design.[11] ZnPc features weak or even no absorption between 400 and 550 nm. This gap can easily be covered by a corresponding dye-zeolite antenna.

1.3. Luminescent Solar Concentrators

A luminescent solar concentrator (LSC) is basically a transparent plate (plastic or glass) containing luminescent centers. Light enters the face of the plate and is partially absorbed and re-emitted by these centers. A fraction of the luminescent light is trapped by total internal reflection and guided to the edges of the plate where it can be converted to, for example, electricity by a solar cell. As the edge area of the plate is much smaller than the face area, the LSC operates as a concentrator of light.[15]

The photostability of the dye-matrix composite is an important factor determining the potential of LSCs for photovoltaic energy conversion applications. Direct inclusion of luminescent organic molecules into an organic matrix is particularly problematic in this regard. Introducing suitable dye molecules into nano-sized zeolite crystals and dispersing the resulting dye-zeolite composites in an organic polymer is expected to yield increased photostability. This "prepackaging" of molecules furthermore opens possibilities for the use of dyes which would be incompatible with a given organic matrix. A first step into this direction has recently been accomplished by the successful preparation of transparent zeolite-polymer hybrids.[16]

For strongly luminescent materials, there is a considerable overlap between absorption and emission spectra. Self-absorption therefore becomes an important loss mechanism in LSCs. A solution to this problem is the use of a two-dye-zeolite system. Absorption and emission spectra are separated by employing an absorbing species **A** and an emitting species **B**. The concentration of **A** is high to ensure efficient light absorption. The electronic excitation energy is transferred along the zeolite channels by FRET to **B**, which then emits light in a wavelength range where **A** does not absorb. As the concentration of **B** does not necessarily need to be high, self-absorption of light emitted by **B** becomes negligible. Zeolites containing more than two dyes can be used to create an energy transfer cascade[5c] and to adjust the absorption properties of the LSC to the spectrum of the incident radiation.

The design shown in Figure 1.3 goes a step further by employing oriented dye-zeolite monolayers instead of homogeneously dispersed and randomly oriented dye-zeolite nanoparticles. Such a design is promising in terms of exploiting the defined orientation of electronic transition dipole moments present in dye-zeolite composites. For a given guest molecule in zeolite L, the possible orientations of its electronic transition dipole moment can be described by a double cone shaped distribution.[17] The opening angle of this cone depends to a large extent on the size of the guest molecule.[3] For most of the organic dyes that have been included into zeolite L, the electronic transition dipole moment of the first $\pi^* \leftarrow \pi$ transition coincides with the long axis of the molecule.[1a] As a long molecule tends to align with its long axis parallel to the channel axis, the opening angle of the corresponding transi-

tion dipole moment double cone is small. Short molecules, on the other hand, typically feature larger opening angles.

Light shining on the face of a LSC plate will be mostly absorbed by dipoles which are oriented parallel to the face. However, such dipoles also have a higher probability of emitting light into the escape cone. The half apex angle of the escape cone is given by arcsin(1/*n*), where *n* is the index of refraction of the plate. Light emitted into the escape cone will not be totally internally reflected and therefore literally escape (if no reabsorption occurs). An arrangement as shown in Figure 1.3 could be used to minimize emission into the escape cone. In a first step, light entering the face of the plate is absorbed by molecules with a wide double cone distribution of electronic transition dipole moments (blue). In a second step, the electronic excitation energy is transported by FRET to an acceptor featuring a narrower double cone distribution (green), therefore having a lower probability of emitting into the escape cone (red). Whether such an arrangement would be beneficial for the efficiency of LSCs has yet to be experimentally verified.

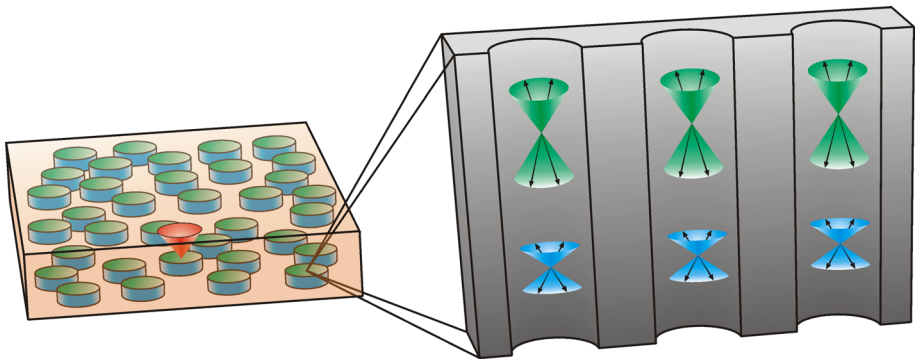

Figure 1.3. Luminescent solar concentrator (LSC) based on oriented dye-zeolite crystals. The channels of the disc-shaped zeolite crystals run perpendicular to the face of the LSC. The schematic axial cut (right) shows the double cone distribution of the electronic transition dipole moments for two different dyes. The blue double cones represent the light absorbing molecules (large cone angle), whereas the green double cones indicate the light emitting molecules (small cone angle). The concentration of the latter is kept low to avoid self-absorption. The red cone illustrates an escape cone originating at a light emitting molecule located close to a channel entrance.

1.4. Conclusions

When using zeolites as host materials, the options for combining different guest species and engineering the photophysical properties are manifold. One-dimensional channel systems, as present in zeolite L, allow for a high degree of supramolecular organization, which can be exploited to obtain energy transfer cascades and orientation of electronic transition dipole moments. The excellent compatibility of zeolites with many different environments and the extensive tunability of dye-zeolite inclusion compounds offers new challenges for implementation in photonic devices for solar energy conversion.

References (Chapter 1)

1. a) D. Brühwiler, G. Calzaferri, *Microporous Mesoporous Mater.* **2004**, *72*, 1; b) G. Schulz-Ekloff, D. Wöhrle, B. van Duffel, R. A. Schoonheydt, *Microporous Mesoporous Mater.* **2002**, *51*, 91.
2. Ch. Baerlocher, L. B. McCusker, D. H. Olson, 'Atlas of Zeolite Framework Types', 6th edition, Elsevier, Amsterdam, **2007**.
3. H. Maas, A. Khatyr, G. Calzaferri, *Microporous Mesoporous Mater.* **2003**, *65*, 233.
4. C. Minkowski, G. Calzaferri, *Angew. Chem. Int. Ed.* **2005**, *44*, 5325.
5. a) M. L. Cano, V. Fornés, H. Garcia, M. A. Miranda, J. Pérez-Prieto, *J. Chem. Soc., Chem. Commun.* **1995**, 2477; b) H. Garcia, S. Garcia, J. Pérez-Prieto, J. C. Scaiano, *J. Phys. Chem.* **1996**, *100*, 18158; c) M. Pauchard, A. Devaux, G. Calzaferri, *Chem. Eur. J.* **2000**, *6*, 3456.
6. a) S. H. Tolbert, A. Firouzi, G. D. Stucky, B. F. Chmelka, *Science* **1997**, *278*, 264; b) B. Platschek, N. Petkov, T. Bein, *Angew. Chem. Int. Ed.* **2006**, *45*, 1134; c) C.-W. Wu, T. Ohsuna, M. Kuwabara, K. Kuroda, *J. Am. Chem. Soc.* **2006**, *128*, 4544.
7. a) A. Zabala Ruiz, D. Brühwiler, T. Ban, G. Calzaferri, *Monatsh. Chem.* **2005**, *136*, 77; b) Y.-J. Lee, J. S. Lee, K. B. Yoon, *Microporous Mesoporous Mater.* **2005**, *80*, 237; c) T. Ban, H. Saito, M. Naito, Y. Ohya, Y. Takahashi, *J. Porous Mater.* **2007**, *14*, 119; d) A. Zabala Ruiz, D. Brühwiler, L.-Q. Dieu, G. Calzaferri, in 'Materials Syntheses', Ed. U. Schubert, N. Hüsing, R. Laine, Springer, Wien, **2008**, p. 9–19.
8. a) J. S. Lee, H. Lim, K. Ha, H. Cheong, K. B. Yoon, *Angew. Chem. Int. Ed.* **2006**, *45*, 5288; b) A. Zabala Ruiz, H. Li, G. Calzaferri, *Angew. Chem. Int. Ed.* **2006**, *45*, 5282.
9. A. Devaux, K. Lutkouskaya, G. Calzaferri, L.-Q. Dieu, D. Brühwiler, L. De Cola, T. Torres, *Chimia* **2007**, *61*, 626.
10. S. Huber, G. Calzaferri, *Angew. Chem. Int. Ed.* **2004**, *43*, 6738.

11. R. Koeppe, O. Bossart, G. Calzaferri, N. S. Sariciftci, *Sol. Energy Mater. Sol. Cells* **2007**, *91*, 986.
12. L.-Q. Dieu, A. Devaux, I. López-Duarte, M. V. Martinez-Diaz, D. Brühwiler, G. Calzaferri, T. Torres, *Chem. Comm.* **2008**, 1187.
13. L. Groenendaal, F. Jonas, D. Freitag, H. Pielartzik, J. R. Reynolds, *Adv. Mater.* **2000**, *12*, 481.
14. a) D. Brühwiler, G. Calzaferri, *C. R. Chimie* **2005**, *8*, 391; b) M. Busby, H. Kerschbaumer, G. Calzaferri, L. De Cola, *Adv. Mater.* **2008**, *20*, 1614.
15. a) W. H. Weber, J. Lambe, *Appl. Opt.* **1976**, *15*, 2299; b) A. Goetzberger, W. Greubel, *Appl. Phys.* **1977**, *14*, 123; c) J. S. Batchelder, A. H. Zewail, T. Cole, *Appl. Opt.* **1979**, *18*, 3090; d) J. S. Batchelder, A. H. Zewail, T. Cole, *Appl. Opt.* **1981**, *20*, 3733; e) P. Kittidachachan, L. Danos, T. J. J. Meyer, N. Alderman, T. Markvart, *Chimia* **2007**, *61*, 780.
16. S. Suárez, A. Devaux, J. Bañuelos, O. Bossart, A. Kunzmann, G. Calzaferri, *Adv. Funct. Mater.* **2007**, *17*, 2298.
17. S. Megelski, A. Lieb, M. Pauchard, A. Drechsler, S. Glaus, C. Debus, A. J. Meixner, G. Calzaferri, *J. Phys. Chem. B* **2001**, *105*, 25.

2. Phthalocyanine-based Stopcocks

A photonic antenna material for the sensitization of organic solar cells based on zinc phthalocyanine (ZnPc, Figure 1.1) requires a molecular species that is able to extract the electronic excitation energy from the dyes in the channels.[1] In a collaboration with the research group of Prof. Tomás Torres (University of Madrid), we have developed stopcock molecules featuring a ZnPc head and various tail moieties (Figure 2.1). While the tail is able to enter the channels, the ZnPc head is too large and remains on the external surface.

ZnPc-R stopcocks were deposited onto the zeolite crystals from a solvent. The optimization of the channel entrance adsorption (with tails extending into the channels) while simultaneously avoiding adsorption on the coat of the crystals is a delicate process that generally requires extensive screening of solvents and adsorption conditions. The principle of selectively adsorbing molecules at the channel entrances makes use of the different properties of the base and coat surfaces of zeolite L crystals (Figure 2.2).

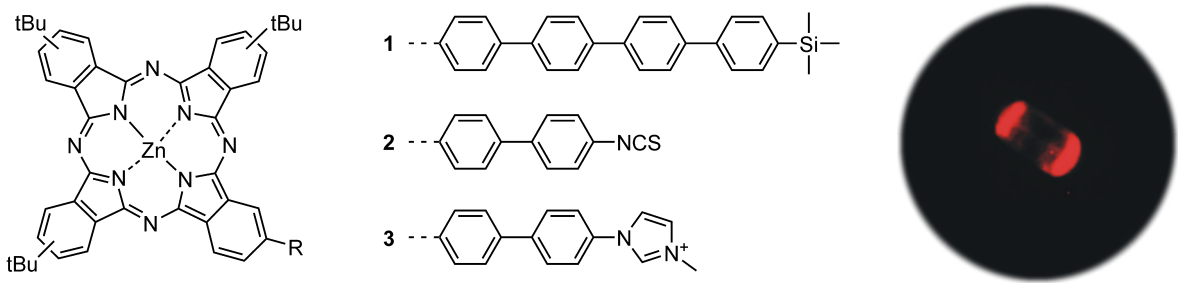

Figure 2.1. Stopcocks ZnPc-R with various tail moieties (R = 1, 2, 3). The *tert*-butyl groups mimic an intrinsic insulating layer. The representative fluorescence microscopy image shows a single zeolite L crystal (ca. 5 µm length) that has been functionalized with ZnPc-1. Bright fluorescence is observed at the base surfaces of the cylindrical crystal.

Selective adsorption at the channel entrances of zeolite L was accomplished for all three ZnPc-R stopcocks.[2,3] First results were obtained with ZnPc-1. Energy transfer was observed in combination with oxonine molecules (acting as donors) in the channels. However, characterization and further processing of this antenna material proved difficult due to the weak interaction of ZnPc-1 with the zeolite channels. To obtain a more robust attachment of the stopcocks, we focused on a tail with an isothiocyanate group (ZnPc-2), allowing coupling with 3-aminopropyldimethylmethoxysilane (APDMMS) and subsequent covalent anchoring in the zeolite channels. Despite the increased stability, antenna materials prepared with thionine as donor molecules showed only minor improvement in terms of energy transfer compared to

the materials containing ZnPc-1. It is very likely that the long tail of the silane-coupled ZnPc-2 resulted in distances between donor molecules and stopcocks that are too large for efficient FRET (Figure 2.3).

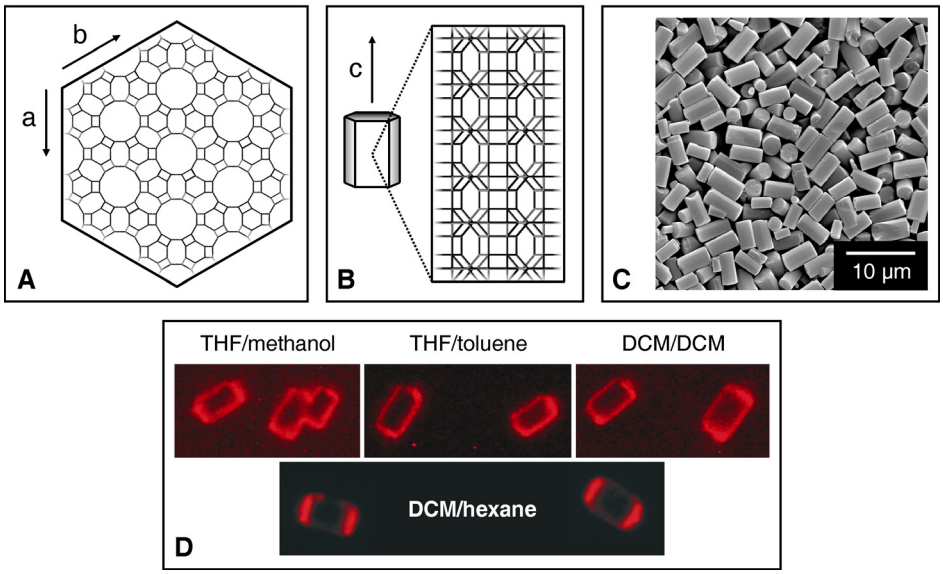

Figure 2.2. Selective adsorption at the channel entrances of zeolite L vs. non-specific adsorption. A) Hexagonal face along the c-axis of the crystal showing the channel entrances. B) View of a side wall (coat) of a crystal. C) Typical zeolite L crystals used for fluorescence microscopy imaging of the distribution of molecules in the channels and on the base and coat surfaces. D) Fluorescence microscopy images of zeolite L crystals (ca. 5 µm length) after adsorption of ZnPc-1 from various solvent mixtures. The first component of the solvent pairs indicates the solvent used for preparing a solution of ZnPc-1. This solution was subsequently added to a dispersion of zeolite L crystals in a second solvent. In all cases, the amount of ZnPc-1 in the solution corresponded to the number of channel entrances. Selective adsorption at the channel entrances is observed when a solution of ZnPc-1 in dichloromethane (DCM) is added to a dispersion of zeolite L in n-hexane.[2]

Photoluminescence measurements of antenna materials containing ZnPc-R were performed on suspensions in $CHCl_3$ and on dry layers on a quartz plate. In the latter configuration, we observed quenching, most likely being caused by interactions between ZnPc-R stopcocks on adjacent zeolite L crystals that are in contact via their base surfaces.

In terms of stability and energy transfer efficiency, the best results were obtained with ZnPc-3. This stopcock features a cationic tail (PF_6^- is the counter ion). Adsorption at the channel entrances of zeolite L proceeds via cation exchange. The electrostatic interaction between

the tail and the negatively charged aluminosilicate framework stabilizes the channel end adsorbed ZnPc-3. Remarkable energy transfer was observed in combination with thionine donors in nano-sized zeolite L crystals (Figure 2.4).[3] This system provides an excellent starting point for further research on dye-zeolite based materials for the sensitization of organic solar cells.

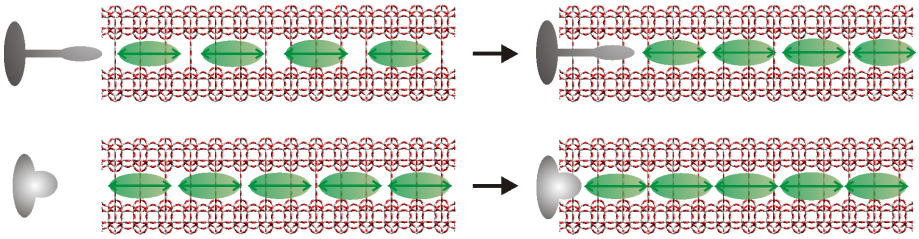

Figure 2.3. Attaching stopcocks to the channel entrance of zeolite L already densely packed with guest molecules. In the top case, adsorption of the stopcock implies diffusion of the guest molecules and might therefore be difficult to achieve under mild conditions. Stopcocks with short tails require electrostatic interaction with the zeolite framework or covalent attachment to the channel entrance for sufficient stability.[4]

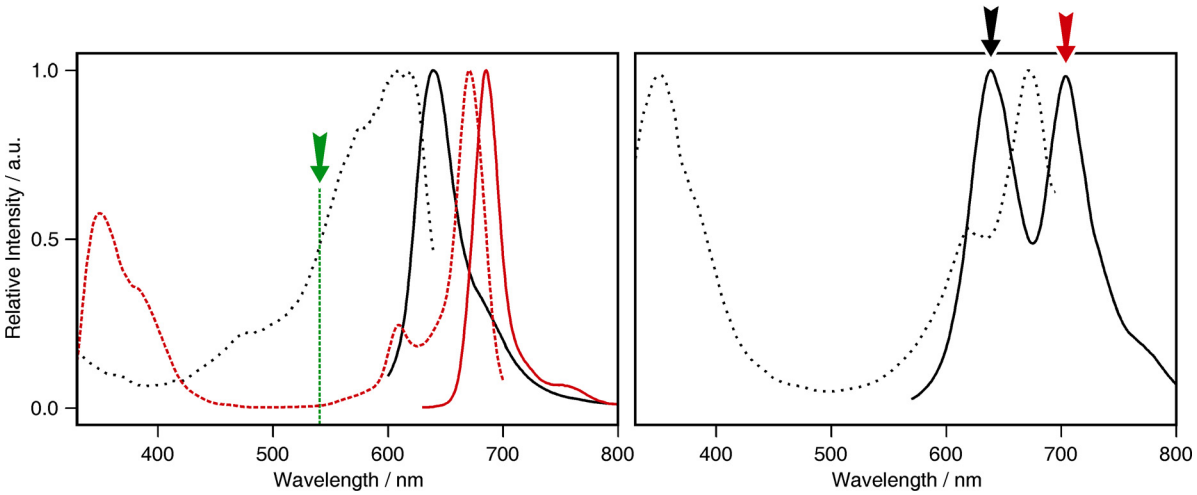

Figure 2.4. Left: Excitation (black, dotted) and emission spectrum (black, solid) of thionine compared to the excitation (red, dashed) and emission spectrum (red, solid) of ZnPc-3. Right: Excitation (dotted) and emission spectrum (solid) of a thionine/ZnPc-3 antenna material. Zeolite L crystals with an average size of 50 nm were used. Upon selective excitation of thionine at 540 nm (green arrow), the emission spectrum of the antenna material features two well developed bands at 638 nm (black arrow) and 704 nm (red arrow), corresponding to thionine and ZnPc-3, respectively. The excitation spectrum observed at 720 nm shows contributions of thionine and ZnPc-3.[3]

A maximum number of channel entrances has to be equipped with ZnPc stopcocks to obtain efficient energy transfer. For this purpose, a combined electrostatic and covalent attachment would be ideal.[4] In a first step, the stopcock is adsorbed by cation exchange (as for ZnPc-3). Conditions are then changed to induce a reaction between a group located on the stopcock head and silanol groups at the channel entrances, removing the respective ZnPc stopcocks from the cation exchange equilibrium. ZnPc stopcock adsorption by cation exchange and subsequent covalent attachment is then repeated to obtain a maximum number of closed channels. Synthetic work towards stopcocks with such combined binding abilities is currently in progress.

Once the energy transfer from a given donor to a ZnPc stopcock has been optimized, the light-harvesting properties of the photonic antenna system can be adjusted by adding a further donor, possibly on the short wavelength side of thionine, thereby establishing an energy transfer cascade (see also Chapter 3.3).

References (Chapter 2)

1. R. Koeppe, O. Bossart, G. Calzaferri, N. S. Sariciftci, *Sol. Energy Mater. Sol. Cells* **2007**, *91*, 986.
2. L.-Q. Dieu, A. Devaux, I. Lòpez-Duarte, M. V. Martínez-Díaz, D. Brühwiler, G. Calzaferri, T. Torres, *Chem. Commun.* **2008**, 1187.
3. a) L.-Q. Dieu, PhD Thesis, University of Zurich, 2010; b) I. Lòpez-Duarte, L.-Q. Dieu, M. V. Martínez-Díaz, T. Torres, D. Brühwiler, G. Calzaferri, *manuscript in preparation*.
4. D. Brühwiler, G. Calzaferri, T. Torres, J. H. Ramm, N. Gartmann, L.-Q. Dieu, I. Lòpez-Duarte, M. V. Martínez-Díaz, *J. Mater. Chem.* **2009**, *19*, 8040.

3. An Advanced Luminescent Solar Concentrator

3.1. Self-Absorption: The Problem

The conventional design of a luminescent solar concentrator (LSC) involves a dye with a high luminescence quantum yield dispersed in a transparent polymer. However, the efficiency of devices based on this concept is insufficient for applications in solar energy conversion. Self-absorption due to the spectral overlap of absorption and emission is clearly a major problem of conventional LSCs. The use of triplet emitters to spectrally separate the absorption and emission bands cannot be considered a possible solution, as the long-lived triplet states are highly problematic in terms of stability.

We have systematically examined the performance of conventional thin film LSCs based on a fluorescent dye in PMMA (Figure 3.1). The results show that despite excellent light-harvesting, self-absorption strongly limits the optical efficiency of such LSCs.[1] The perylene dye Lumogen F Red 305 (BASF, hereafter referred to as Red 305), which is frequently used as the luminescent species in LSCs,[2,3] was dissolved in $CHCl_3$ containing PMMA (Aldrich, average molecular weight = 120'000), and the resulting mixture was cast onto a glass substrate. Red 305 is ideal for this kind of application, as it features a near-unity luminescence quantum yield.[3] Its spectrum covers a large part of the visible range with emission in the red. Excellent intrinsic stability has been reported.[4] Furthermore, high concentrations of the dye in PMMA can be achieved without aggregation.

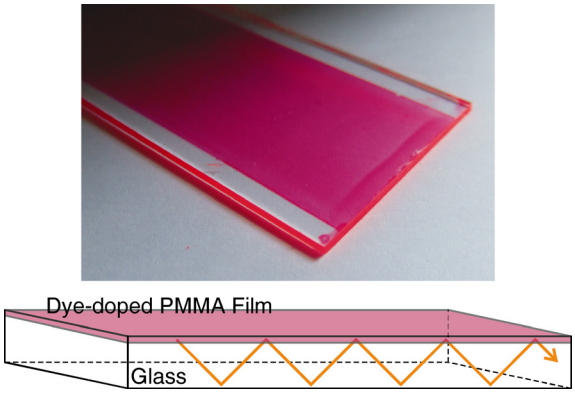

Figure 3.1. Photograph and principle of operation of a LSC based on a thin dye-doped polymer film on glass. Ideally, the first-generation fluorescence is transported to the edge without re-absorption. In conventional LSCs, such a situation can, however, not be realized.

The capability of a LSC to concentrate light depends on the geometry of the plate and is given by the ratio between the top and the edge surface area (geometric gain *G*):

$$G = \frac{A_{top}}{A_{edge}} \tag{1}$$

The photon flux gain ϕ_{opt} is defined as follows:

$$\phi_{opt} = G \cdot \eta_{opt} \tag{2}$$

where η_{opt} is the optical efficiency. The optical efficiency of a LSC is the energy coming out of the edges of the plate divided by the energy falling on the plate and can be described by three main processes: (i) Absorption of the incident light, (ii) re-emission of the absorbed photons, and (iii) photon transport to the edges of the plate. This corresponds to the product given in equation (3).[5]

$$\eta_{opt} = \eta_{LHE}\,\eta_{SA}\,\eta_{yield}\,\eta_{Stokes}\,\eta_{trap}\,\eta_{mat}\,(1-R) \tag{3}$$

η_{LHE} is the light-harvesting efficiency, which depends on the extinction coefficient, the absorption spectrum, and the concentration of the dye, as well as on the thickness of the plate or thin film. This parameter can be calculated from the fraction of incident photons absorbed by the LSC and the photon flux of the light source. The self-absorption parameter, η_{SA}, is mainly governed by the Stokes shift of the dye. The luminescence quantum yield of the dye is given by η_{yield} and depends on the photophysics and the micro-environment of the dye. The Stokes efficiency η_{Stokes} corresponds to the ratio of the emission and absorption maximum (in wavenumbers). The parameter η_{trap} includes the trapping efficiency governed by the refractive index of the medium. Parameters related to photon transport losses, such as scattering and parasitic absorption by matrix defects, are expressed by η_{mat}. *R* is the Fresnel reflection coefficient of the LSC surface.

The light-harvesting efficiency η_{LHE} can be determined from the absorption spectrum of the respective LSC and the emission spectrum of the light source:

$$\eta_{LHE} = \frac{\int_0^\infty S_{so}(\lambda)\left[1-10^{-A(\lambda)}\right]\,\mathrm{d}\lambda}{\int_0^\infty S_{so}(\lambda)\,\mathrm{d}\lambda} \tag{4}$$

The term $(1–10^{-A(\lambda)})$ gives the fraction of absorbed incident photons. $A(\lambda)$ is the absorbance of the system at a wavelength λ, whereas S_{so} is the photon flux spectrum of the light source.

In principle, the self-absorption parameter η_{SA} can be calculated from equation (5), where ε is the extinction coefficient, *c* the dye concentration and *d* the distance covered by the photons until they reach the detector.[6]

$$\eta_{SA} = \int_0^\infty S'_{true}(\lambda) \cdot 10^{-\varepsilon(\lambda)cd} \, \mathrm{d}\lambda \quad \text{with} \quad \int_0^\infty S'_{true} \, \mathrm{d}\lambda = 1 \tag{5}$$

However, the distance *d* remains usually unknown. Thus, η_{SA} is calculated from the emission spectrum of a dilute solution of Red 305 and the edge emission spectrum of the LSC under full surface illumination. The emission spectrum of the dilute solution represents the true emission spectrum in the absence of self-absorption, S_{true}, corresponding to η_{SA} = 1. To calculate η_{SA}, the photoluminescence spectrum measured at the edge is scaled, so that its long wavelength part matches S_{true} (Figure 3.2).[6,7] The scaled edge spectrum is called S'_{edge}. η_{SA} can thus be determined as follows:

$$\eta_{SA} = \frac{\int_0^\infty S'_{edge}(\lambda) \, \mathrm{d}\lambda}{\int_0^\infty S_{true}(\lambda) \, \mathrm{d}\lambda} \tag{6}$$

η_{SA} is independent of the spectrum of the light source, but can depend on the light intensity. A near-unity luminescence quantum yield was found for Red 305 in PMMA, hence η_{yield} = 1.[3] A Stokes efficiency, η_{Stokes}, of 0.94 was calculated from the absorption and emission maxima. It should be noted that the Stokes efficiency concerns losses in terms of energy but does not influence the number of photons. The trapping efficiency can be determined as follows:

$$\eta_{trap} = \sqrt{1 - \frac{1}{n^2}} \tag{7}$$

With $n \approx 1.5$ (for PMMA and glass), a trapping efficiency of 0.75 is obtained. Assuming perfect photon transport (η_{mat} = 1) and a Fresnel reflection coefficient *R* of 0.04 (for PMMA and glass), the optical efficiency of the LSCs can be estimated. The results are given in Figure 3.2, illustrating how an increasing light-harvesting efficiency is typically compensated by an increased degree of self-absorption, thus leading to only minor improvement of the optical efficiency. The optical efficiencies estimated from the spectral-based analysis are consistent with values obtained from measuring the effective photon flux gain.[1]

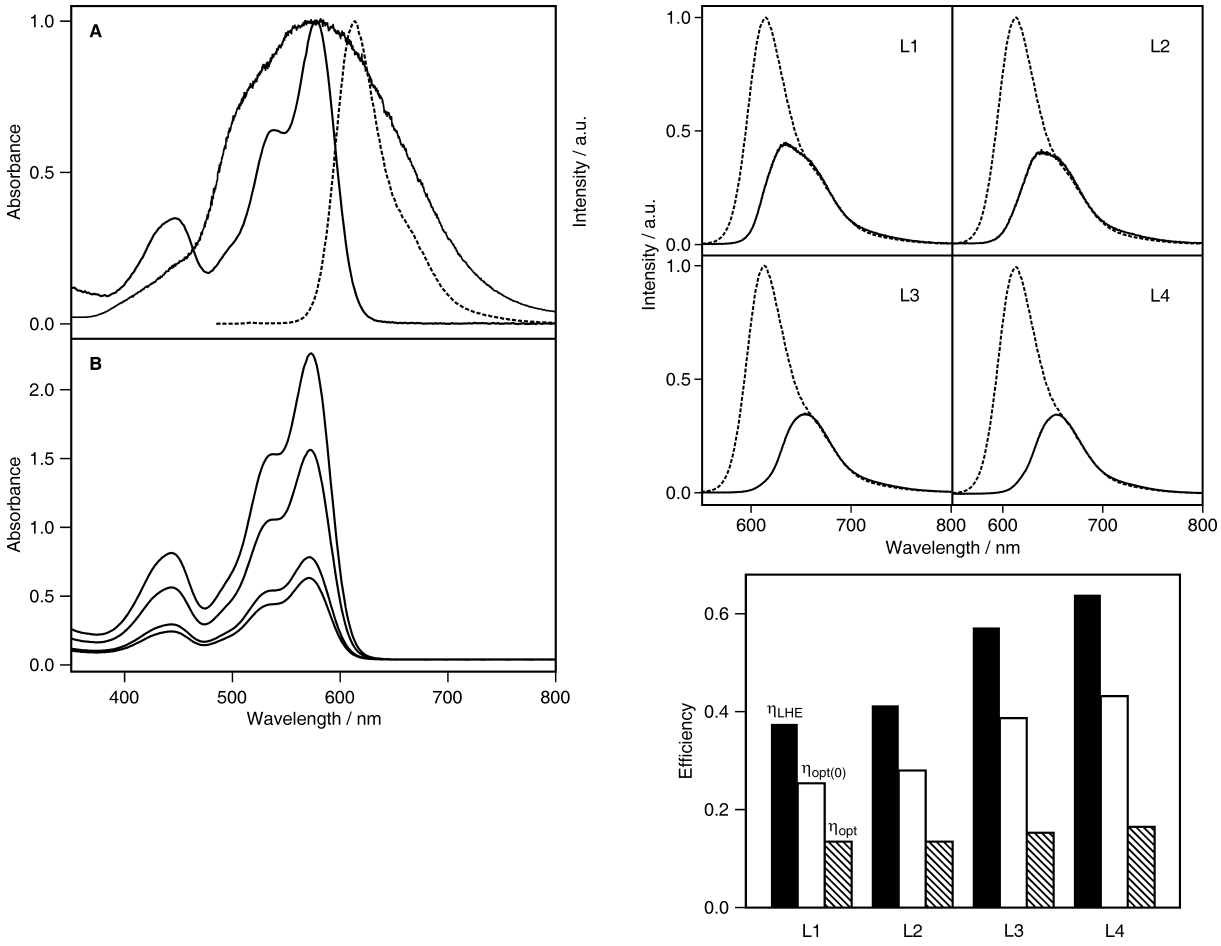

Figure 3.2. Left panel: A) Absorption (solid) and emission (dashed) spectra of Red 305 in ethanol. The spectral characteristics of the light source are represented by the broad emission band. B) Absorption spectra of thin film LSCs L1 (4 µm), L2 (5 µm), L3 (10 µm), and L4 (15 µm, from bottom to top). Right panel: Comparison of the true emission spectrum (dashed) and the scaled edge emission spectra of the LSCs. Note that the red shift of the edge emission increases with increasing film thickness. The bar chart shows the values for the light-harvesting efficiency η_{LHE}, the optical efficiency in absence of self-absorption $\eta_{opt(0)}$, and the optical efficiency η_{opt} obtained by means of a spectral-based analysis according to equation 3 (including self-absorption).

3.2. Self-Absorption: A Possible Solution

An efficient LSC requires low self-absorption of the emitted photons, while maintaining a high absorptivity for the incoming photons. As described in Chapter 1, our patented approach employs an energy transfer cascade in dye-filled zeolite L nanochannels to achieve a spectral separation of absorption and emission.[8] Dye domains are obtained by sequential insertion of different chromophores into zeolite L (Figure 3.3).[9] High local concentrations of

monomeric dye molecules, often impossible to achieve in dye/polymer dispersions, are accessible by this approach.

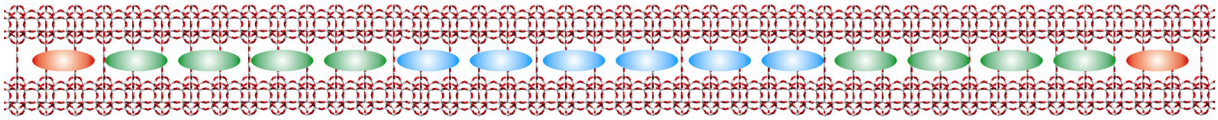

Figure 3.3. The sequential insertion of different dye molecules into the channels of zeolite L leads to the formation of dye domains and establishes an energy transfer cascade.

The potential of the dye-zeolite approach for the preparation of strongly light-absorbing polymer thin films is demonstrated by the example shown in Figure 3.4. We have prepared a single dye system with PR149 (Figure 3.5) as chromophore. Insertion of the dye was accomplished by sublimation in vacuum. After removing molecules adsorbed on the external surface of the zeolite crystals, the PR149-zeolite was dispersed in PMMA/$CHCl_3$ and subsequently spread on a glass substrate by doctor blading, yielding a thin PR149-zeolite/polymer film (ca. 35 µm). Because of the excellent matching of the refractive indices of zeolite and PMMA, dye-zeolite/PMMA films exhibit very little scattering. In the absorption maximum, 95 % of the incoming photons are absorbed by the thin film (Figure 3.4), despite of the fact that, as a consequence of the relatively slow intrachannel diffusion of PR149, only about 17 % of the available sites in the zeolite channels are occupied.

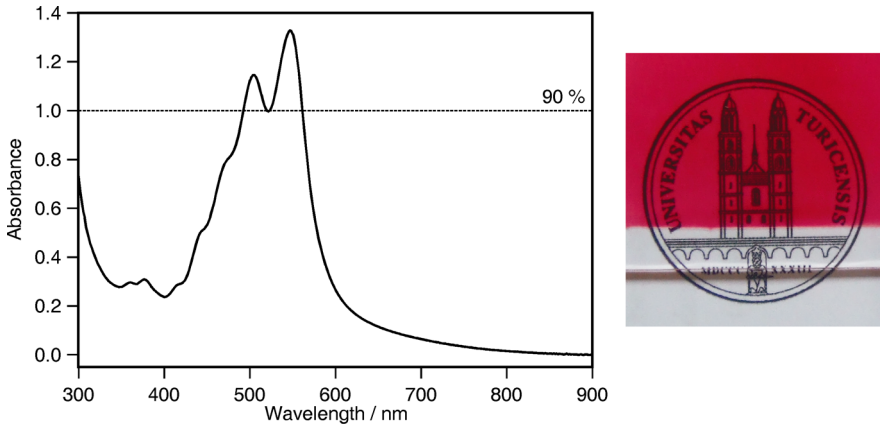

Figure 3.4. Absorption spectrum of a PR149-zeolite/PMMA thin film on glass. The image shows a sample on top of a white paper with a seal of the University of Zurich.

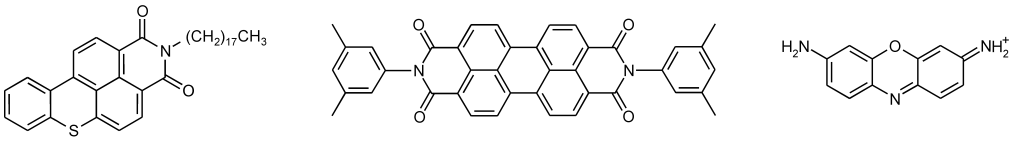

Figure 3.5. Dye molecules used for first prototypes of luminescent solar concentrators based on dye-zeolite inclusion compounds.

The reduction of self-absorption requires a system with an efficient energy transfer between the light-absorbing dyes (donors) and the light-emitting dyes (acceptors). To ensure efficient light absorption, the concentration of the donors has to be kept high. A suitable donor needs to fulfill a series of requirements. Besides the obvious photophysical properties (high extinction coefficient, high luminescence quantum yield, spectral overlap of the emission with the acceptor absorption, high intrinsic photostability), donors should be able to efficiently enter and diffuse through the zeolite L channels. This considerably facilitates the synthesis of highly loaded dye-zeolite samples. Extensive screening led us to the commercial dye HY3G (Figure 3.5). High loading levels of HY3G can be achieved under relatively mild conditions. The requirements for the acceptors, which are inserted at the end of the channels in low concentration, are different compared to the donors. Neutral molecules, such as HY3G, are adsorbed in the zeolite channels via van der Waals interactions. To avoid leaching of the donors, the adsorption of the acceptors should be comparatively strong. This condition is fulfilled if cationic molecules are used as acceptors. The aluminosilicate framework of zeolite L is negatively charged and charge compensating cations (usually Na^+ or K^+) can be exchanged. The electrostatic interaction between cationic dye and zeolite framework leads to a stable occlusion of the neutral donors. The donor/acceptor combination of HY3G/Ox^+ proved to be a good choice in terms of energy transfer efficiency. The absorption spectrum of a HY3G-Ox^+-zeolite/PMMA thin film on glass (Figure 3.6) illustrates the large excess of donor molecules (donor/acceptor ≈ 20). Selective excitation of the donor produces a fluorescence spectrum featuring a dominant acceptor emission despite an extremely low acceptor concentration. The energy transfer efficiency in this particular system is close to 80 %. HY3G-Ox^+-zeolite/PMMA thin films can be prepared in free-standing form (Figure 3.7).

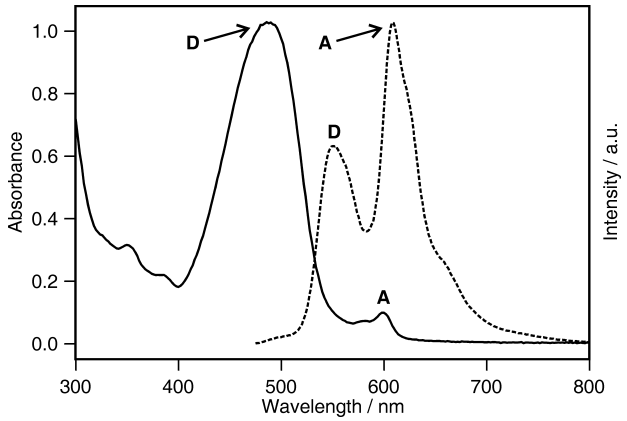

Figure 3.6. Absorption spectrum (solid line) and emission spectrum (dashed line) of a HY3G-Ox^{+}-zeolite/PMMA thin film on glass. The bands are assigned to the donor (**D**) and acceptor molecules (**A**). The emission spectrum was recorded upon selective excitation of the donor at 450 nm.

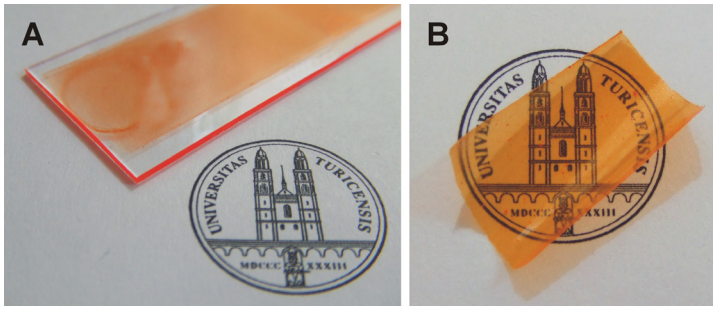

Figure 3.7. A) Photographic image of a HY3G-Ox^{+}-zeolite/PMMA thin film on glass. The image was taken under diffuse light (indoor, no artificial light source). Even under these conditions, an intense emission at the edges of the LSC is visible. B) Free-standing HY3G-Ox^{+}-zeolite/PMMA thin film. The diameter of the University seal is 2 cm.

The length of the hexagonal zeolite L crystals, and thus the length of the nanochannels, is an important parameter determining the properties of the energy transfer systems. A large variety of crystal sizes is available for zeolite L.[10] We found that a channel length of about 600 nm is ideal for our purpose. In the case of longer channels, high dye loadings are increasingly difficult to obtain and the overall energy transfer efficiency tends to decrease as the distance that the electronic excitation energy needs to travel increases. Shorter channels, on the other hand, do not allow the introduction of an amount of donor molecules (per channel) that would be sufficient to ensure the high donor/acceptor ratio required for the reduction of self-absorption.

3.3. Optimization of the First Prototypes

Obtaining quantitative energy transfer (no donor emission) was identified as a first key issue for optimization. In the HY3G-Ox^+ system, we were not able to achieve this goal. Lumogen Yellow F 083 (LYF083, Figure 3.8) in combination with Ox^+, however, gave excellent results (Figure 3.9). LYF083 can be inserted into the channels of zeolite L under relatively mild conditions. Sealing of the channels is particularly important for this donor dye, as considerable leaching was observed upon adsorption of water.

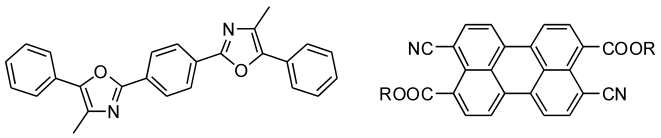

DMPOPOP LYF083 (R = isobutyl)

Figure 3.8. Dye molecules used for the optimization of the first prototypes. DMPOPOP is a short-wavelength absorber, whereas Lumogen Yellow F 083 (LYF083) can be inserted into the channels of zeolite L in high loading and under mild conditions.

The preparation of the dye-zeolite/PMMA thin films had to be improved in order to increase the area of the LSCs from 14 cm^2 (Figure 3.7A) to 100 cm^2 (Figure 3.9) while maintaining good optical quality. A 3-step technique that includes the deposition of an adhesion layer (PMMA/$CHCl_3$), an intermediate zeolite/PMMA layer (from acetonitrile/butanol), and a final PMMA cover layer, gave excellent results.

LSCs which absorb green and yellow light, but are transparent for blue and red light, are ideal for covering the windows of greenhouses, as they are able to harvest the part of the visible spectrum that cannot be converted by green plants. To cover a wider range of wavelengths, we have investigated possibilities for the preparation of a 3-dye system, containing two types of donor dyes and one type of acceptor dye. The absorption and emission properties of a representative 3-dye system are shown in Figure 3.10. Absorption occurs almost over the entire range of visible light. The red emission of Ox^+ is dominant irrespective of the wavelength of excitation.

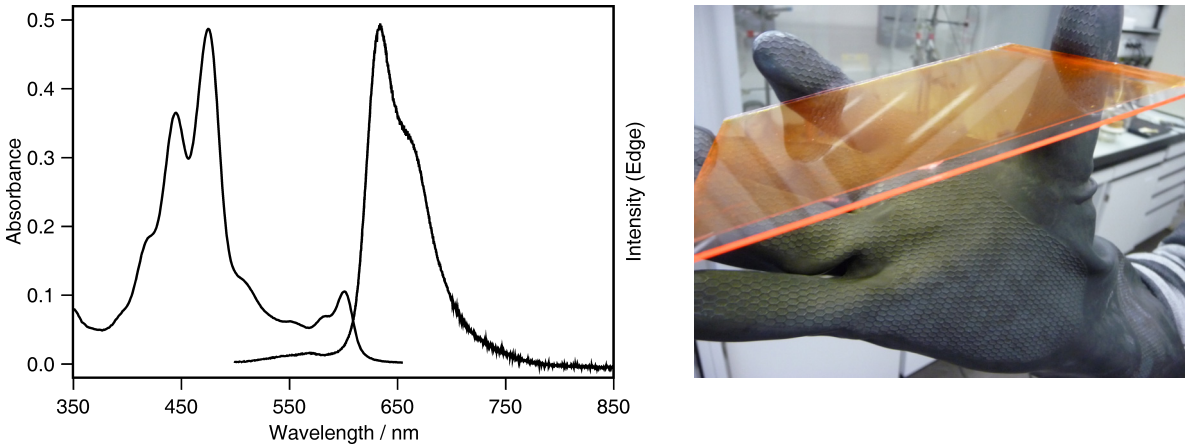

Figure 3.9. Absorption and emission spectrum (edge) of a LYF083-Ox^+-zeolite/PMMA film on glass. The emission spectrum, showing exclusive acceptor fluorescence, was recorded upon selective excitation of the donor. The photographic image shows a corresponding LSC plate with an area of approximately 100 cm^2.

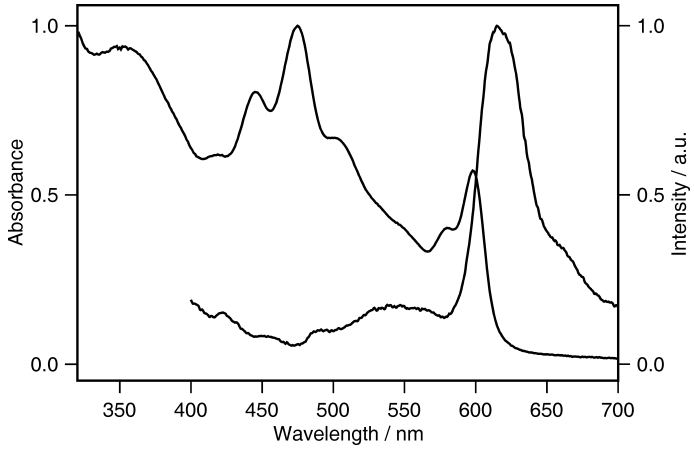

Figure 3.10. Absorption and emission spectrum of a 3-dye system containing DMPOPOP and LYF083 as donors. Ox^+ was used as acceptor dye. Excitation was performed at 375 nm.

Apart from self-absorption, a further key problem that has limited the commercial viability of LSCs is the long-term stability of the luminescent centers. One could argue that concepts employing inorganic instead of organic chromophores might be more successful in this regard. Indeed, research on LSCs based on quantum dots (QDs) has recently become increasingly popular.[11] However, it should be noted that these materials suffer from their own disadvantages. QDs with the most suitable photophysical properties are typically of the core-shell type with CdSe cores. Even for these highly luminescent materials, a near-unity luminescence quantum yield has not been reached. Furthermore, and maybe more importantly, the high toxicity of the materials is problematic in view of commercial applications. Rare

earths, on the other hand, exhibit superior stability but feature narrow absorption bands with low extinction coefficients, requiring high concentrations which lead to increased cost.

The key advantages that make organic dyes attractive for use as active components in LSCs are near-unity luminescence quantum yields, high extinction coefficients (> 100'000 $M^{-1}cm^{-1}$ is possible), and availability in a wide range of colors. In terms of the long-term stability, the intrinsic photostability of the organic dyes is in fact not the main problem, as excellent progress has been made with perylenes and violanthrones. Complications arise when the dyes are dispersed in an organic polymer matrix, which typically contains monomer residues, initiators, stabilizers, and other additives.[12] Avoiding the direct contact between the dyes and the polymer matrix by incorporating them into the zeolite crystals is a potential solution for this problem. The ability of zeolites to protect organic guests against chemical attack, photobleaching or thermal decomposition has been discussed in the literature. Examples include the light-sensitive 1,6-diphenylhexatriene, which is stabilized in zeolite L, because the available space for *trans* to *cis* isomerization is insufficient.[13] Protection against chemical attack was observed in cases where reactive species had to overcome a large diffusional barrier or where anions were not able to enter the zeolite channels.[14] In the case of our dye-zeolite materials for LSCs, we found that the stability of the systems was reduced after dispersion in PMMA. To limit the diffusion of reactive species into the zeolite channels and to prevent leaching of the dyes, the channels need to be sealed. This is best accomplished by the use of trialkoxysilylated stopcock molecules.[15]

From our current state of knowledge, it is clear that a donor/acceptor ratio above 20 is required to significantly reduce self-absorption. The dye-zeolite concept is presently the only system where such an extended arrangement of molecules is feasible. Furthermore, the possibilities for "spectral engineering" (defining absorption and emission ranges) are intriguing from a scientific and application oriented point of view.

3.4. Future Directions

The concept of orienting the electronic transition dipole moments of the emitting dyes for the purpose of reducing the emission into the escape cone has been discussed in Chapter 1. Such an oriented arrangement is expected not only to affect the emission into the escape cone, but also the self-absorption and the light-harvesting efficiency. Due to the complexity of the system, these effects are difficult to predict. In principle, we already have the knowledge to assemble an oriented system as schematically shown in Figure 1.3. Oriented monolayers of disc-shaped zeolite L crystals can be prepared so that the channels are running perpendicular to the substrate. The orientation of the electronic transition dipole moments is largely

a function of the size of the respective molecule and can be described by a double cone shaped distribution.[16] For the acceptor dye, a large molecule such as PR149, that aligns along the channel axis, is ideal (Figure 3.11). Calculations indicate that at least three monolayers of zeolite crystals (corresponding to ca. 2 g of dye-zeolite per m^2) would be needed to obtain a sufficiently high light-harvesting efficiency. In order to achieve efficient FRET, the double cone distribution of the donor dyes should have a small opening angle. However, it should be noted that this will reduce the absorption of light entering perpendicular to the face of the LSC.

Due to the relatively small channel entrance of zeolite L (0.71 nm, Figure 1.2), many interesting dyes, particularly such that emit in the red/near-infrared cannot be inserted. In fact, 95 % of the known zeolite framework types have pore entrances with ring sizes of 12 or below, leading to pore diameters considerably smaller than 1 nm. The few examples of extra-large pore zeolites (Table 3.1) only slightly increase the pore diameter range.

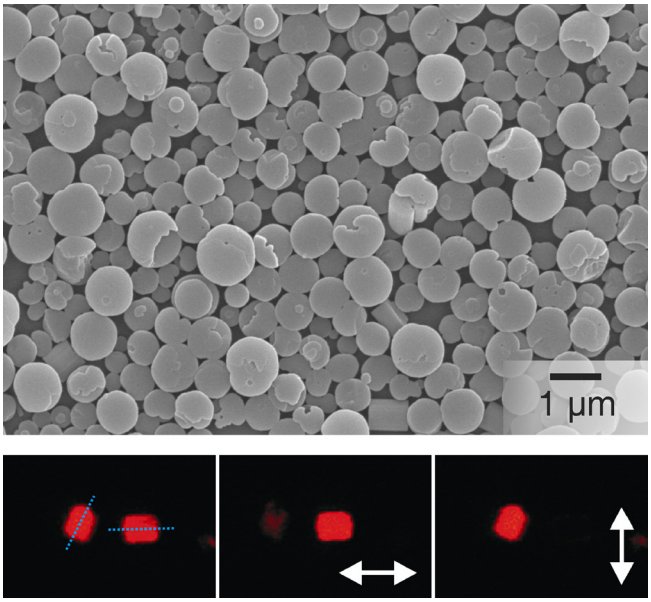

Figure 3.11. Top: Scanning electron microscopy image of a monolayer of oriented zeolite L crystals. Bottom: Orientation of the electronic transition dipole moment of PR149 in the channels of zeolite L. The fluorescence microscopy images show two PR149-zeolite crystals with a length of approximately 2 µm. The channel axis (c-axis) is indicated by the blue line. The image on the left was taken without a polarizer. The direction of the polarizer used for the middle and right image is represented by the double arrow.[9]

Table 3.1. Selection of extra-large pore zeolites (one-dimensional channel systems only)[17]

Material	Composition	Ring Size	Pore Size [nm]
VPI-5	$AlPO_4$	18	1.27 × 1.27
AlPO-8	$AlPO_4$	14	0.79 × 0.87
UTD-1F	SiO_2	14	0.81 × 0.82
CIT-5	SiO_2	14	0.72 × 0.75

Based on our experience with mesoporous silica (see Part I), we decided to follow, in terms of the pore size, a top-down approach. Arrays of silica nanochannels (ASNCs) can be considered a mesoporous analogue of zeolite L, with the main differences being the larger pore size and the amorphous silica framework. The standard synthesis of ASNCs yields a material with a pore diameter of approximately 3 nm (Figure 3.12).[18,19] Adjustments to this procedure, for example by using a structure-directing agent with a shorter alkyl chain, are problematic, as the hexagonal morphology of the particles is extremely sensitive to changes in the composition of the reaction mixture. We have found that the pore size can be reduced in a well-controlled manner without significant broadening of the pore size distribution by postsynthetically depositing tetraethoxysilane (Figure 3.12). It is therefore possible to adapt the diameter of the channels to the size of a given guest molecule.

As outlined in Part I, the channel walls of mesoporous silica are highly functionalizable. Regarding the use of ASNCs as host material for luminescent molecules, this opens various intriguing possibilities. The external surface and the pore surface can be modified independently (Figure 3.12A), providing an optimized interaction with the surrounding medium (to maximize the dispersibility in a polymer, for example), while maintaining an ideal environment for the guests. Functional groups can be placed predominantly at the pore openings, enabling channel sealing (Figure 3.12B). Gradients of functional groups can be generated, allowing the definition of domains for the adsorption of different guests (Figure 3.12C). In terms of preparing energy transfer cascades similar to those in dye-zeolite L materials, such gradients are expected to be of particular importance.

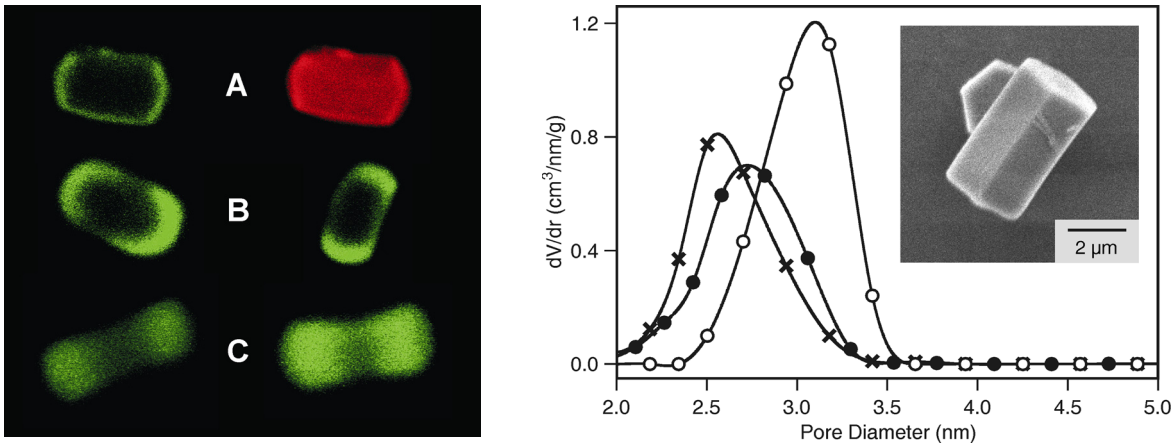

Figure 3.12. Left: Confocal laser scanning microscopy images of functionalized and fluorescence-labeled ASNCs showing selective functionalization of external and pore surfaces (A), predominant modification of channel entrances (B), and concentration gradients of grafted groups (C). Optical slices in the center of the particles were selected. In all cases, aminopropyl moieties acted as functional groups.[19] Right: Scanning electron microscopy image of ASNCs and pore size distribution (NLDFT) of calcined ASNCs before (○) and after deposition of additional silica layers (● and ×).

References (Chapter 3)

1. T. Dienel, C. Bauer, I. Dolamic, D. Brühwiler, *Solar Energy*, in press.
2. a) L. H. Slooff, E. E. Bende, A. R. Burgers, T. Budel, M. Pravettoni, R. P. Kenny, E. D. Dunlop, A. Büchtemann, *Phys. Stat. Sol. (RRL)* **2008**, *2*, 257; b) T. J. J. Meyer, T. Markvart, *J. Appl. Phys.* **2009**, *150*, 063110.
3. L. R. Wilson, B. S. Richards, *Appl. Opt.* **2009**, *48*, 212.
4. W. G. J. H. M. van Sark, K. W. J. Barnham, L. H. Slooff, A. J. Chatten, A. Büchtemann, A. Meyer, S. J. McCormack, R. Koole, D. J. Farrell, R. Bose, E. E. Bende, A. R. Burgers, T. Budel, J. Quilitz, M. Kennedy, T. Meyer, C. De Mello Donegá, A. Meijerink, D. Vanmaekelbergh, *Optics Express* **2008**, *16*, 21773.
5. A. Zastrow, *Proc. SPIE* **1994**, *2255*, 534.
6. T.-S. Ahn, R. O. Al-Kaysi, A. M. Müller, K. M. Wentz, C. J. Bardeen, *Rev. Sci. Instrum.* **2007**, *78*, 086105.
7. P. Kittidachachan, L. Danos, T. J. J. Meyer, N. Alderman, T. Markvart, *Chimia* **2007**, *61*, 780.
8. G. Calzaferri, A. Kunzmann, D. Brühwiler, C. Bauer, Pat. CH 698333, WO 2010/009560.
9. D. Brühwiler, G. Calzaferri, T. Torres, J. H. Ramm, N. Gartmann, L.-Q. Dieu, I. Lòpez-Duarte, M. V. Martínez-Díaz, *J. Mater. Chem.* **2009**, *19*, 8040.

10. a) A. Zabala Ruiz, D. Brühwiler, T. Ban, G. Calzaferri, *Monatsh. Chem.* **2005**, *136*, 77; b) A. Zabala Ruiz, D. Brühwiler, L.-Q. Dieu, G. Calzaferri, in 'Materials Syntheses', Ed. U. Schubert, N. Hüsing, R. Laine, Springer, Wien, **2008**, p. 9–19.
11. B. C. Rowan, L. R. Wilson, B. S. Richards, *IEEE J. Select. Top. Quant. Electron.* **2008**, *14*, 1312.
12. R. Kinderman, L. H. Slooff, A. R. Burgers, N. J. Bakker, A. Büchteman, R. Danz, J. A. M. van Roosmalen, *J. Sol. Ener. Eng.* **2007**, *129*, 277.
13. M. Pauchard, A. Devaux, G. Calzaferri, *Chem. Eur. J.* **2000**, *6*, 3456.
14. a) G. Calzaferri, D. Brühwiler, S. Megelski, M. Pfenniger, M. Pauchard, B. Hennessy, H. Maas, A. Devaux, U. Graf, *Solid State Sci.* **2000**, *2*, 421; b) M. L. Cano, V. Fornés, H. García, M. A. Miranda, J. Pérez-Prieto, *J. Chem. Soc., Chem. Commun.* **1995**, 2477; c) H. García, S. García, J. Pérez-Prieto, J. C. Scaiano, *J. Phys. Chem.* **1996**, *100*, 18158.
15. a) T. Ban, D. Brühwiler, G. Calzaferri, *J. Phys. Chem. B* **2004**, *108*, 16348; b) M. M. Tsotsalas, K. Kopka, G. Luppi, S. Wagner, M. P. Law, M. Schäfers, L. de Cola, *ACS Nano* **2010**, *4*, 342.
16. a) S. Megelski, A. Lieb, M. Pauchard, A. Drechsler, S. Glaus, C. Debus, A. J. Meixner, G. Calzaferri, *J. Phys. Chem. B* **2001**, *105*, 25; b) A. Gasecka, L.-Q. Dieu, D. Brühwiler, S. Brasselet, *J. Phys. Chem. B* **2010**, *114*, 4192.
17. Ch. Baerlocher, W. M. Meier, D. H. Olson, 'Atlas of Zeolite Framework Types', 5th edition, Elsevier, Amsterdam, **2001**.
18. Y. Kievsky, I. Sokolov, *IEEE Trans. Nanotechnol.* **2005**, *4*, 490.
19. N. Gartmann, D. Brühwiler, *Angew. Chem. Int. Ed.* **2009**, *48*, 6354.

4. Pattern Formation in Zeolite/Polymer Films

When preparing zeolite/polymer films, we observed the formation of patterns under certain conditions. The size and shape of the patterns was controllable and reproducible. The resemblance of the zeolite patterns to biological patterns motivated us to investigate the underlying mechanisms in more detail. The formation of self-organized patterns involves the spontaneous emergence of order from a population of interacting elements. Concepts of pattern formation in non-living systems are increasingly applied as tools to investigate the organization of cells[1] and to provide new insights in the field of developmental biology.[2] Zeolite L is ideal for such studies, as this material is available in a wide range of sizes and morphologies[3] and can be filled with a large variety of luminescent guests,[4] allowing convenient imaging by fluorescence microscopy. The external surface of the zeolite crystals can furthermore be functionalized to tune the interaction of the particles with the surrounding medium.[5]

The pattern formation in the zeolite/polymer/solvent system can be understood within the general framework of the model of local self-activation and lateral inhibition, i.e., a short-range positive feedback coupled to a long-range negative feedback (Figure 4.1). This type of mechanism has been used to explain biological pattern formation and is based on the amplification of local inhomogeneities by an autocatalytic process which is complemented by an inhibitory component.[6]

To visualize the patterns, the channels of the zeolite crystals were filled with the luminescent dye oxonine (Figure 3.5).[7] Dye-loaded zeolite crystals were prepared by refluxing 70 mg of zeolite L (Lucidot® DISC, Clariant, height = 0.2 – 0.4 μm, diameter = 0.5 – 2 μm) in an aqueous solution of oxonine chloride (4.5 mL, 0.13 mM) for 16 h. The crystals were recovered by centrifugation, washed with methanol to remove molecules adsorbed on the external surface, and oven-dried at 60 °C. To prepare the zeolite/PMMA films, the oxonine-loaded crystals were dispersed in chloroform by ultrasonication for 30 min. In parallel, PMMA (M_{av} = 120'000, Aldrich) was dissolved in chloroform. The zeolite dispersion and the PMMA solution were mixed and stirred to obtain a homogeneous suspension containing typically 1 mL of chloroform. Zeolite/PMMA films were then prepared on ordinary microscopy glass slides by doctor blading on an area of 7 cm × 2 cm, resulting in a specific initial thickness of the wet zeolite/PMMA film (t_0, see Figure 4.1). The evaporation of the solvent subsequently takes place in less than 15 s. The slides were washed with ethanol and distilled water before use.

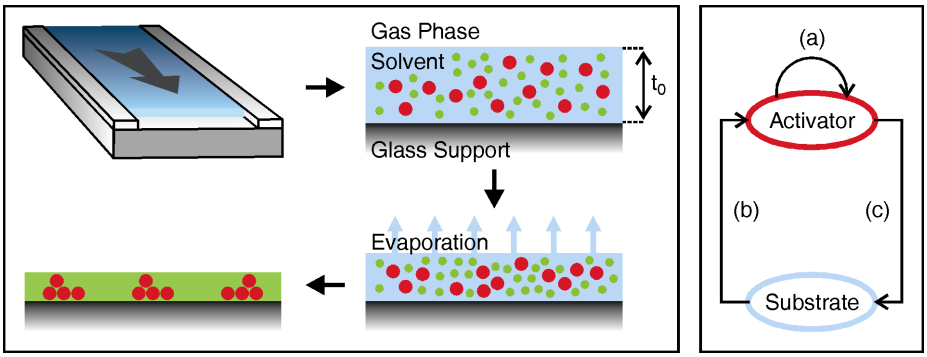

Figure 4.1. Pattern formation and feedback loops. The left panel illustrates schematically the solvent (blue) evaporation that leads to the formation of patterns of zeolite crystals (red) in a polymer (green). The initial wet film thickness, t_0, is an important parameter controlling the size and shape of the patterns. The right panel shows the feedback loops involved in the pattern formation (activator = zeolite, substrate = solvent). Activating processes (a) and (c) are complemented by an inhibitory process (b).

To obtain octyl-modified zeolite crystals, an oxonine-loaded sample (50 mg) was dispersed in dry toluene (10 mL) containing octyltrimethoxysilane (20 µL, 0.08 mmol, Aldrich) and stirred at 75 °C for 20 h. The octyl-modified crystals were recovered by centrifugation, washed with hexane, and oven-dried at 60 °C. For the preparation and characterization of PMMA films with mixtures of octyl-modified and unmodified zeolite, the unmodified crystals were loaded with pyronine instead of oxonine by refluxing 35 mg of zeolite in an aqueous solution of pyronine (3,6-diaminoxanthylium) acetate (5 mL, 0.04 mM) for 20 h. Fluorescence microscopy images were acquired on a Olympus BX 60 microscope.

The size and the shape of the patterns in the zeolite/PMMA/$CHCl_3$ system can be controlled by adjusting three starting parameters, namely the initial PMMA concentration (c_0), the zeolite concentration, and the wet film thickness (t_0). Figure 4.2 shows fluorescence microscopy images of the patterns as a function of t_0 and c_0.

With c_0 = 10.2 wt% and t_0 = 50 µm, a pattern featuring zeolite aggregates with a diameter on the order of 80 µm was obtained (Figure 4.2, pattern A1). Interestingly, the aggregates display central regions that are free of zeolite crystals. With decreasing c_0, the spacing between the aggregates becomes larger, as the lower viscosity apparently facilitates the motion of the zeolite crystals (pattern B1 and C1). Furthermore, aggregates with distinct central regions free of zeolite crystals are less common at low c_0 (pattern C1).

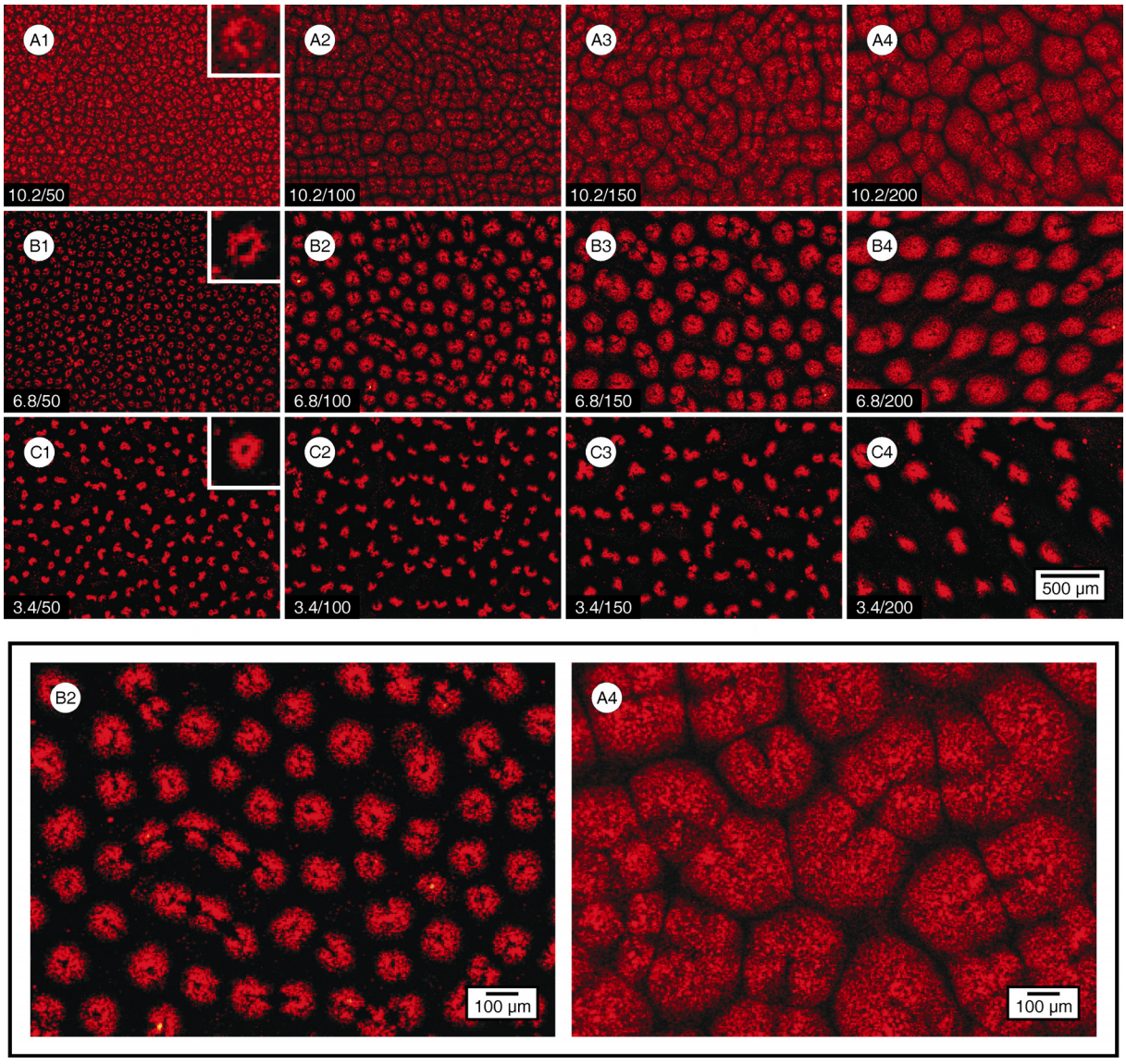

Figure 4.2. Patterns of oxonine-loaded zeolite crystals in PMMA films imaged by fluorescence microscopy. The numbers in the lower left corner of each image indicate the values for c_0 and t_0 in [wt%] and [µm], respectively. The insets in column 1 show a 5-fold zoom of single zeolite aggregates. The bottom panel gives a magnified view of patterns B2 and A4. All patterns were prepared with a zeolite concentration of 5g/L.

In the investigated range, the size of the zeolite aggregates was found to increase linearly with increasing t_0 (Figure 4.3, left). For a given value of t_0, on the other hand, the average size of the zeolite aggregates increases with increasing c_0 (Figure 4.3, right). A particularly interesting effect is observed in the case of c_0 = 10.2 wt% (Figure 4.2, series A). As t_0 increases, the aggregates are no longer isolated, but form groups of aggregates with the appearance of spiral defect chaos in certain regions. With c_0 = 6.8 wt% (Figure 4.2, series B), the zeolite aggregates exhibit shapes such as rings, half-moons, and two parallel bands

(patterns B1 and B2). The population of circular aggregates increases with increasing t_0 and the zeolite-free region in the center of the aggregates gradually disappears (patterns B3 and B4). For c_0 = 3.4 wt% (Figure 4.2, series C), the shape of the aggregates is comparatively indistinct.

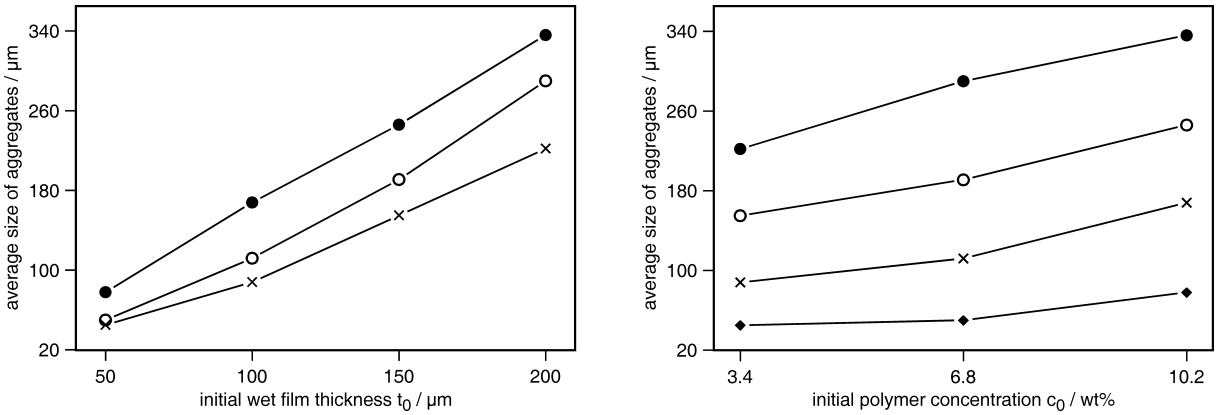

Figure 4.3. Left: Average size of aggregates of zeolite crystals as a function of the initial wet film thickness for an initial polymer concentration of 10.2 wt% (●), 6.8 wt% (○), and 3.4 wt% (×). Right: Average size of aggregates of zeolite crystals as a function of the initial polymer concentration for an initial wet film thickness of 200 µm (●), 150 µm (○), 100 µm (×), and 50 µm (♦). The uncertainty of the average values is typically ± 20 %.

Figure 4.4 (top) illustrates the influence of the zeolite concentration on the patterns. At low zeolite concentration (4 g/L), no distinct pattern is formed. At a concentration of 8 g/L, a pattern consisting of ring-shaped aggregates can be identified. Keeping c_0 and t_0 constant and further increasing the zeolite concentration leads to a decrease of the size of these aggregates. A fluorescence microscopy image of the cross-section of a zeolite/PMMA film on glass is shown in the bottom left panel of Figure 4.4. The red spots correspond to zeolite aggregates, confirming the inclusion of the zeolite crystals in the PMMA film. Images taken with raking light (Figure 4.4, bottom right) reveal a considerable surface roughness, indicating that three-dimensional aggregation of the zeolite crystals occurs.

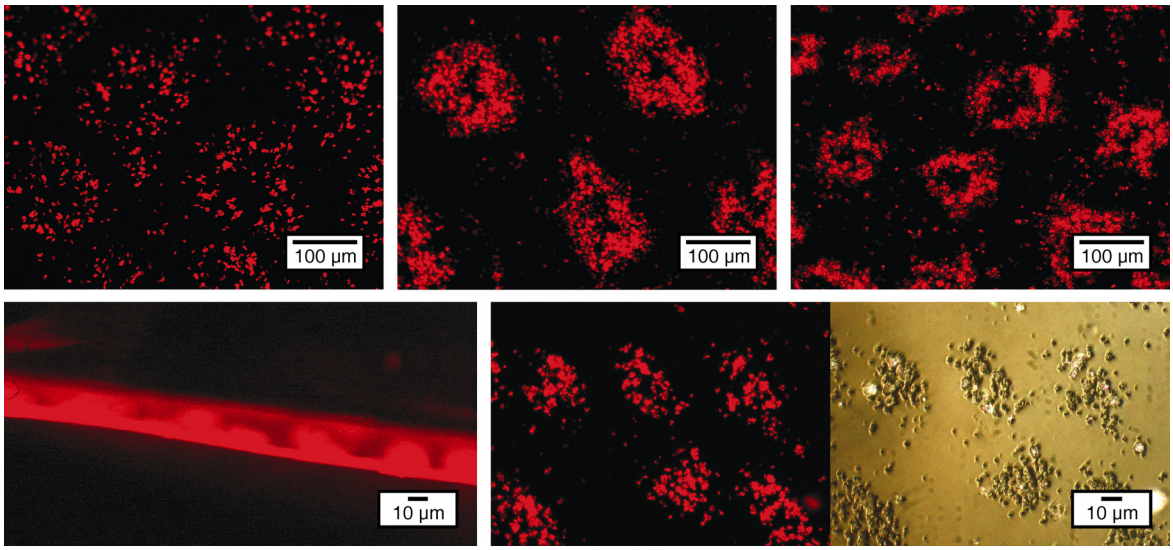

Figure 4.4. Top: Fluorescence microscopy images of patterns formed at various zeolite concentrations. Values for c_0 and t_0 were kept constant (3.2 wt% and 200 µm, respectively). The zeolite concentration increases from left to right (4, 8, and 16 g/L). Bottom: Evidence for three-dimensional aggregation. Left: Fluorescence microscopy image showing a cross-sectional view of a zeolite/PMMA film. Right: Fluorescence microscopy and raking light image of the same area of a zeolite/PMMA film.

Because of the non-equilibrium and non-linear nature of the system, the identification of the mechanism responsible for the pattern formation is challenging. It is reasonable to assume that the formation of the patterns is a direct consequence of the instability driven by the evaporation of the solvent. To explain the formation of patterns under such conditions, Rayleigh-Bénard and Marangoni convection have been invoked.[8] Alternative mechanisms have been proposed to explain the formation of mesoscopically scaled patterns in polymer solution systems.[9] The present system is more complex, as it additionally includes microparticles. For Turing patterns, the instability is driven by the diffusion of the species involved in the chemical reactions.[10] Here, a physical process (the evaporation of the solvent) creates an instability, leading to the appearance of patterns. Nevertheless, the general principles of the Turing model can be employed to explain the pattern formation. We propose that the self-organization in the present system follows a mechanism based on a short-range positive feedback coupled to a long-range negative feedback.[6] In a similar way as for the mechano-chemical theory applied to the aggregation of cells in an elastic matrix,[11] the attraction between the zeolite particles is responsible for the feedback loops. The positive feedback (Figure 4.1, process (a)) can be understood as follows: A region of high zeolite particle density recruits an increasing amount of particles from its vicinity, as the particles facilitate the evaporation of the solvent (Figure 4.1, process (c)), rendering the zeolite particles in the

aggregates less mobile. The long-range negative feedback (Figure 4.1, process (b)) is caused by the evaporation of the solvent occurring over the entire surface of the film, inhibiting the local increase of particle density. As the solvent gradually disappears, the PMMA/solvent system, which acts as the matrix in which the zeolite crystals can move, becomes less penetrable. Furthermore, a cross-inhibition occurs, as the growth of a given aggregate of zeolite crystals reduces the number of crystals that are available to form aggregates at other sites. According to this mechanism, we can expect that the self-organization process is insensitive towards the specific interaction of the zeolite with the solvent and the polymer. To test this hypothesis, we have functionalized the external zeolite surface with octyl chains by following a well established procedure that is based on the reaction of surface silanol groups with respective organotrialkoxysilane precursors.[5] Patterns obtained with octyl-modified zeolite were indeed very similar to those obtained with unmodified zeolite (Figure 4.5, pattern A and B). The preparation of PMMA films with mixtures of octyl-modified and unmodified zeolite crystals (loaded with oxonine and pyronine, respectively) yielded a uniform distribution of the two types of crystals throughout the pattern (Figure 4.5, pattern C).

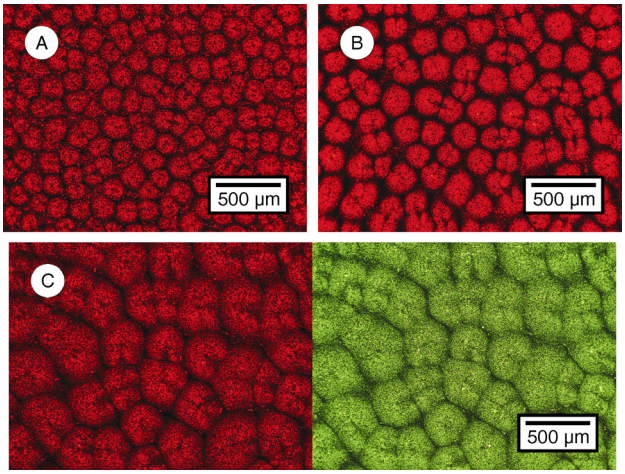

Figure 4.5. Fluorescence microscopy image of a pattern formed by octyl-modified zeolite crystals (A). The pattern obtained with unmodified zeolite crystals under otherwise identical conditions is shown for comparison (B). The bottom panel (C) shows the pattern obtained upon preparation of a PMMA film containing a mixture of octyl-modified zeolite crystals (loaded with oxonine, red emission) and unmodified zeolite crystals (loaded with pyronine, green emission).

We have shown that in a three-component system consisting of zeolite crystals, polymer, and a solvent, a variety of patterns can be obtained by the variation of one of three parameters. A mechanism based on local self-activation and lateral inhibition is most likely responsi-

ble for the organization of the zeolite crystals in the polymer films. A series of further studies on this system can be envisaged, concerning, for example, the influence of particle size or solvent volatility. The identification of the control parameters in relation with theoretical models is expected to yield valuable insight into the mechanisms for the formation of patterns far from equilibrium.[12]

References (Chapter 4)

1. a) E. Karsenti, *Nature Rev.* **2008**, *9*, 255; b) A. S. Mikhailov, G. Ertl, *ChemPhysChem* **2009**, *10*, 86.
2. a) J. D. Murray, in 'Mathematical Biology', Springer, Berlin, **2008**; b) 'Mathematical models for biological pattern formation', Ed. P. K. Maini, H. G. Othmer, Springer, Berlin, **2000**.
3. A. Zabala Ruiz, D. Brühwiler, T. Ban, G. Calzaferri, *Monatsh. Chem.* **2005**, *136*, 77.
4. D. Brühwiler, G. Calzaferri, T. Torres, J. H. Ramm, N. Gartmann, L.-Q. Dieu, I. López-Duarte, M. V. Martínez-Díaz, *J. Mater. Chem.* **2009**, *19*, 8040.
5. a) B.-Z. Zhan, M. A. White, M. Lumsden, *Langmuir* **2003**, *19*, 4205; b) D. Brühwiler, G. Calzaferri, *C. R. Chimie* **2005**, *8*, 391; c) S. Suárez, A. Devaux, J. Bañuelos, O. Bossart, A. Kunzmann, G. Calzaferri, *Adv. Funct. Mater.* **2007**, *17*, 2298.
6. a) A. Gierer, H. Meinhardt, *Kybernetik* **1972**, *12*, 30; b) A. J. Koch, H. Meinhardt, *Rev. Mod. Phys.* **1994**, *66*, 1481; c) H. Meinhardt, A. Gierer, *BioEssays* **2000**, *22*, 753.
7. N. Gfeller, S. Megelski, G. Calzaferri, *J. Phys. Chem. B* **1998**, *102*, 2433.
8. a) Z. Mitov, E. Kumacheva, *Phys. Rev. Lett.* **1998**, *81*, 3427; b) M. Li, S. Xu, E. Kumacheva, *Langmuir* **2000**, *16*, 7275.
9. a) P. G. de Gennes, *Eur. Phys. J. E* **2001**, *6*, 421; b) E. Bormashenko, R. Pogreb, O. Stanevsky, Y. Bormashenko, T. Stein, R. Cohen, S. Reis, O. V. Gendelman, *J. Mater. Sci.* **2006**, *41*, 455.
10. A. M. Turing, *Trans. Roy. Soc. (London)* **1952**, *B237*, 37.
11. a) J. D. Murray, G. F. Oster, A. K. Harris, *J. Math. Biol.* **1983**, *17*, 125; b) J. D. Murray, G. F. Oster, *J. Math. Biol.* **1984**, *19*, 265.
12. C. Bauer, N. Gartmann, L.-Q. Dieu, N. Zuber, I. Dolamic, J. H. Ramm, D. Brühwiler, *submitted*.

5. Dye-Zeolite Materials: Scientific Collaborations

The previous Chapters of Part II have described research that is strongly motivated by specific applications. Nonetheless, investigating the various levels of organization achievable with dye-zeolite materials remains a challenge. Possibilities in terms of guest species, characterization techniques, or assembly into macroscopic structures are manifold. We are engaged in a series of scientific collaborations targeting specific aspects of organization in dye-zeolite materials. Results of two of these collaborations are briefly outlined in this Chapter.

Information on the orientation of dye molecules in the channels of zeolite L is particularly useful for optimizing the radiationless transport of electronic excitation energy. Previous work has shown that the distribution of electronic transition dipole moments of dyes in the zeolite L channels can be described by a double cone shaped distribution.[1] In collaboration with the group of Sophie Brasselet (Institut Fresnel, Aix-Marseille Université), we have refined this model. The implementation of a polarimetric two-photon excitation fluorescence (TPEF) technique allowed the identification of molecular disorder. Extending the technique to microscopy enabled us to investigate the spatial heterogeneity of the molecular order information. The approach provides a tool to probe the molecular organization of *a priori* unknown distributions with a submicroscopic spatial resolution.[2]

The traditional model, describing the orientational distribution of guest molecules by a cone shape with an aperture angle Θ, was further developed to account for a potential degree of disorder, either dynamic or spatial. This leads to an angular distribution represented by an enlarged cone surface the width of which is a bell-shaped function. The distribution then depends on three parameters (Θ, Ψ, ρ), where Θ is the cone aperture or center of the distribution (mean molecular orientation), Ψ is the full width at half-maximum of the distribution (molecular disorder), and ρ is the global orientation of the cone axis in the macroscopic frame. The latter was found to generally lie along the crystal c-axis (channel axis), as expected from the symmetry of the structure. In agreement with earlier reports,[1] Θ strongly depended on the size of the guest species, with smaller molecules (oxonine or pyronine) adopting large angles (Figure 5.1, Table 5.1). Measurements performed on random positions provided information on the spatial angular heterogeneity. Interestingly, it was observed that a high disorder is correlated with a high molecular concentration, or, in other words, a dense packing of the guest molecules in the channels.

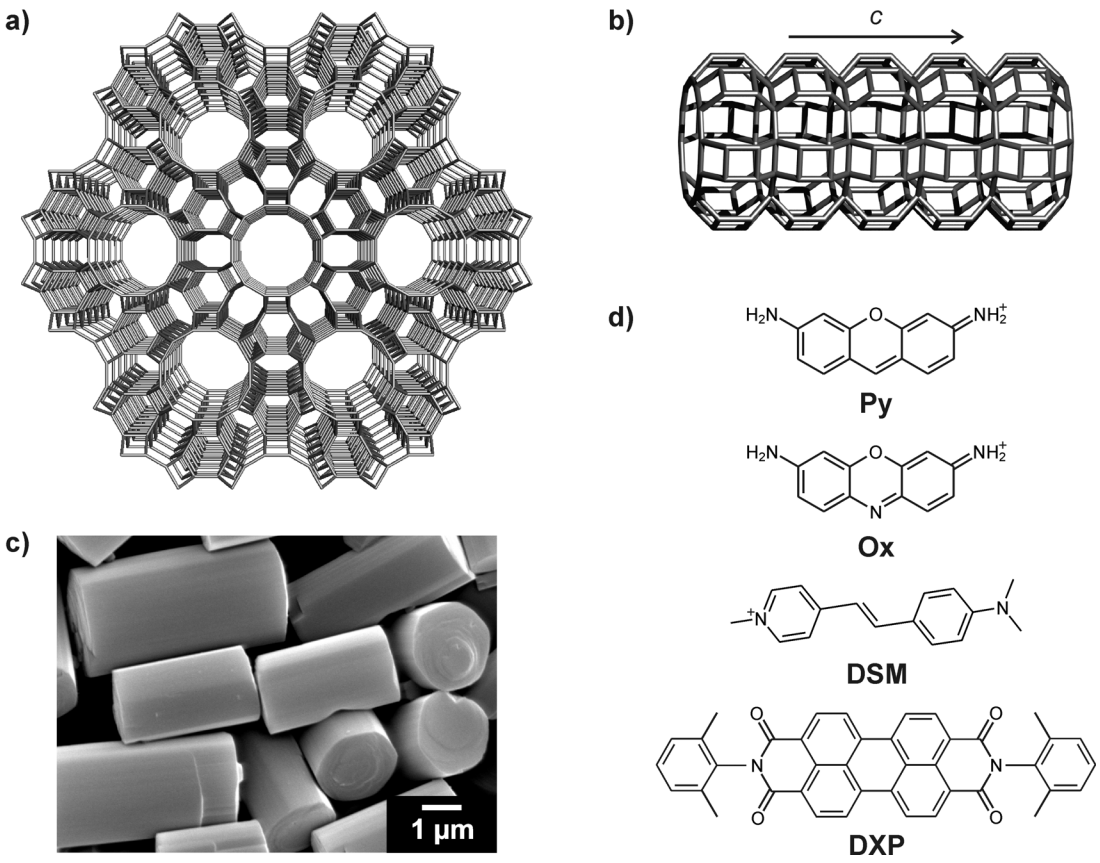

Figure 5.1. (a) Framework of zeolite L viewed along the c-axis. (b) Side view of a main channel. (c) Scanning electron microscopy image of zeolite L crystals used for TPEF polarimetric measurements. (d) Guest molecules.[2]

Table 5.1. Parameters of the distribution obtained from TPEF polarimetric measurements[2]

	DXP	DSM	Ox	Py
Θ	16°	16°	77°	80°
Ψ	19°	26°	24°	15°

The investigation of the spectroscopic properties of furo[3,4-c]furanone[3] in solution (**FF**, Figure 5.2) revealed a complex behavior of absorption and excitation spectra as a function of the concentration, without affecting the fluorescence spectra. Collaborating with Robert Häner and Gion Calzaferri (Departement für Chemie und Biochemie, Universität Bern), we were able to find an explanation for these surprising results.[4]

At concentrations above 10^{-5} M, excitation spectra of **FF** in THF and DCM, showing at low concentrations a maximum at 355 nm, exhibit a pronounced concentration dependence,

splitting into two new bands at 329 nm and 387 nm. Above 10^{-4} M, a further, sharp band appears at 396 nm. This long wavelength band was attributed to the formation of a J-aggregate (collinear orientation of the electronic transition dipole moments). The splitting at medium concentration was assigned to an aggregate in which the electronic transition dipole moments are not on a plane (hereafter referred to as MM-aggregate), leading to allowed transitions to both excited states induced by the interaction. The three types of excitation spectra of **FF** were thus interpreted as being due to equilibria between monomers and two different types of aggregates. Further evidence for this hypothesis was obtained by including **FF** into the channels of zeolite L, thereby inhibiting the formation of the sterically more demanding MM-aggregates, but still allowing the assembly into J-aggregates at high loading levels. Interestingly, the shape and position of the fluorescence spectra of **FF** in solution and in zeolite L were found to be independent of concentration (or loading), temperature, and excitation wavelength. An explanation for this surprising observation is based on the Stokes shift, which was, under all conditions we have investigated, larger than the shift due to J-aggregate coupling. The excited state of the aggregates therefore rapidly reaches the relaxed S_1 state of the monomer, which acts as the lowest emitting state (Figure 5.2).[4]

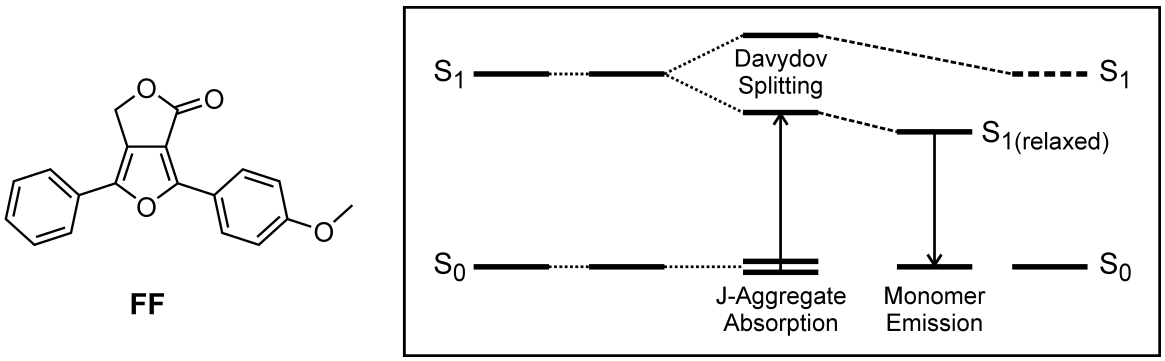

Figure 5.2. Left: Structure of furo[3,4-c]furanone. Right: Energy level diagram of a J-aggregate, suggesting a relaxed monomer emission.[4]

References (Chapter 5)

1. S. Megelski, A. Lieb, M. Pauchard, A. Drechsler, S. Glaus, C. Debus, A. J. Meixner, G. Calzaferri, *J. Phys. Chem. B* **2001**, *105*, 25.
2. A. Gasecka, L.-Q. Dieu, D. Brühwiler, S. Brasselet, *J. Phys. Chem. B* **2010**, *114*, 4192.
3. T. Meng, C. A. Fuhrer, R. Häner, *Synlett* **2009**, *12*, 1951.
4. G. Calzaferri, D. Brühwiler, T. Meng, L.-Q. Dieu, V. L. Malinovskii, R. Häner, *Chem. Eur. J.*, in press.

Appendix

Curriculum Vitae

Personal Data

Name	Dominik Brühwiler
Private Address	Chörenmattstrasse 33, 8965 Berikon phone: 043 455 0035
Campus Address	Institute of Inorganic Chemistry University of Zürich Winterthurerstrasse 190, 8057 Zürich phone: 044 635 4630 e-mail: bruehwi@aci.uzh.ch
Date & Place of Birth	December 6, 1971, Altstätten SG
Nationality	Swiss
Marital Status	Married, 2 children

Research Experience

12/2004 – present	Oberassistent / Research Group Leader Supervisor of 4 PhD theses and 1 MSc thesis Institute of Inorganic Chemistry, University of Zürich
01/2003 – 12/2004	Young Researcher European Union Research Training Network “Nanochannels” Department of Chemistry and Biochemistry, University of Bern
10/2001 – 01/2003	Postdoctoral Fellow Physical Biosciences / Lawrence Berkeley National Laboratory University of California, Berkeley, USA

Teaching Experience

2009 – present	Lecture in Nanochemistry (CHE 621) (University of Zürich)
2005 – 2008	Lecture in Solid State Chemistry (CHE 325.1) Practical courses in Inorganic Chemistry (University of Zürich)
2003 – 2004	Practical courses in Advanced Quantum Chemistry Lecture in Thermodynamics (temporary) Lecture in Chemical Kinetics (temporary) (University of Bern)
1997 – 2001	Assistant in Physical and Quantum Chemistry lab courses (University of Bern)

Education

1997 – 2001	PhD in Chemistry (with excellence) Thesis Advisor: Prof. Dr. Gion Calzaferri University of Bern
1992 – 1997	Diploma in Chemistry University of Bern

Further Activities

- Referee for over 160 papers submitted to international journals (including Chemical Communications, Journal of Materials Chemistry, Chemical Society Reviews, Microporous and Mesoporous Materials, New Journal of Chemistry, Physical Chemistry Chemical Physics, Solar Energy, Dalton Transactions, Angewandte Chemie, Journal of the American Chemical Society, Journal of Physical Chemistry, Langmuir, Nature)
- Member of the Swiss Chemical Society
- Member of the American Chemical Society
- Member of the Steering Committee of the Marie-Curie RTN Nanomatch
- Member of the Editorial Board of *Materials* (ISSN 1996-1944)

Zürich, June 2010

Publications

Self-Organized Patterns of Microparticles in Polymer Films
C. Bauer, L.-Q. Dieu, N. Zuber, N. Gartmann, I. Dolamic, J. H. Ramm, D. Brühwiler*
submitted.

Spectral-based Analysis of Thin Film Luminescent Solar Concentrators
T. Dienel, C. Bauer, I. Dolamic, D. Brühwiler*
Solar Energy, in press.

Surprising Properties of a Furo-Furanone
G. Calzaferri*, D. Brühwiler*, T. Meng, L.-Q. Dieu, V. Malinovskii, R. Häner*
Chemistry – A European Journal, in press.

Postsynthetic Functionalization of Mesoporous Silica
D. Brühwiler*
Nanoscale 2 (2010) 887 – 892.

Direct Synthesis and Fluorescent Imaging of Bifunctionalized Mesoporous Iodopropyl-Silica
J. H. Ramm, N. Gartmann, D. Brühwiler*
Journal of Colloid and Interface Science 345 (2010) 200 – 205.

Probing Molecular Order in Zeolite L Inclusion Compounds Using Two-Photon Fluorescence Polarimetric Microscopy
A. Gasecka, L.-Q. Dieu, D. Brühwiler, S. Brasselet*
Journal of Physical Chemistry B 114 (2010) 4192 – 4198.

The Effect of Water on the Functionalization of Mesoporous Silica with 3-Aminopropyl-triethoxysilane
N. Gartmann, C. Schütze, H. Ritter, D. Brühwiler*
Journal of Physical Chemistry Letters 1 (2010) 379 – 382.

Controlling and Imaging the Functional-Group Distribution on Mesoporous Silica
N. Gartmann, D. Brühwiler*
Angewandte Chemie 121 (2009) 6472 – 6475 (german version).
Angewandte Chemie International Edition 48 (2009) 6354 – 6356.
(Highlighted in ACS Noteworthy Chemistry)

Nanochannels for Supramolecular Organization of Luminescent Guests
D. Brühwiler*, G. Calzaferri*, T. Torres*, J. H. Ramm, N. Gartmann, L.-Q. Dieu, I. Lopez-Duarte, M. V. Martinez-Diaz
Journal of Materials Chemistry 19 (2009) 8040 – 8067.

Accessibility of Amino Groups in Postsynthetically Modified Mesoporous Silica
H. Ritter, D. Brühwiler*
Journal of Physical Chemistry C 113 (2009) 10667 – 10674.

A Comparative Study of the Functionalization of Mesoporous Silica MCM-41 by Deposition of 3-Aminopropyltrimethoxysilane from Toluene and from the Vapor Phase
H. Ritter, M. Nieminen, M. Karppinen, D. Brühwiler*
Microporous and Mesoporous Materials 121 (2009) 79 – 83.

Functionalized Silicate Nanochannels: Towards Applications in Drug Delivery and Solar Energy Conversion
D. Brühwiler*, H. Ritter, J. H. Ramm, L.-Q. Dieu, C. Bauer, I. Dolamic, N. Gartmann
Chimia (Special Issue on Young Academics in Switzerland) 63 (2009) 8 – 13.

Lumineszenzkonzentratoren und Lumineszenzdispergatoren auf der Basis orientierter Farbstoff-Zeolith Antennen
G. Calzaferri, A. Kunzmann, D. Brühwiler, C. Bauer
Patent CH 698333 and WO 2010/009560.

Dye Modified Nanochannel Materials for Photoelectronic and Optical Devices
G. Calzaferri*, H. Li*, D. Brühwiler*
Chemistry – A European Journal 14 (2008) 7442 – 7449.

Novel Phthalocyanine Based Stopcock for Zeolite L
L.-Q. Dieu, A. Devaux, I. Lopez-Duarte, M. V. Martinez-Diaz, D. Brühwiler*, G. Calzaferri*, T. Torres*
Chemical Communications (2008) 1187 – 1189.

Controlling Size and Morphology of Zeolite L
A. Zabala Ruiz, D. Brühwiler, L.-Q. Dieu, G. Calzaferri*
Materials Syntheses, Ed. U. Schubert, N. Hüsing, R. Laine, Springer, Vienna, 2008.

Nanochannel Materials for Quantum Solar Energy Conversion Devices
D. Brühwiler*, L.-Q. Dieu, G. Calzaferri
Chimia (Special Issue on Solar Energy) 61 (2007) 820 – 822.

Nanochannels for Supramolecular Organisation of Dyes
A. Devaux, K. Lutkouskaya, G. Calzaferri*, L.-Q. Dieu, D. Brühwiler, L. De Cola, T. Torres
Chimia (Special Issue on Photochemistry) 61 (2007) 626 – 630.

Distribution of Amino Groups on a Mesoporous Silica Surface after Submonolayer Deposition of Aminopropylsilanes from an Anhydrous Liquid Phase
H. Salmio, D. Brühwiler*
Journal of Physical Chemistry C 111 (2007) 923 – 929.

Hexagonal Network Organization of Dye-Loaded Zeolite L Crystals by Surface Tension Driven Auto-Assembly
S. Yunus*, F. Spano, A. Bolognesi, C. Botta, G. Patrinoiu, D. Brühwiler, A. Zabala Ruiz, G. Calzaferri
Advanced Functional Materials 16 (2006) 2213 – 2217.

Light Harvesting Host-Guest Antenna Materials for Quantum Solar Energy Conversion Devices
G. Calzaferri*, O. Bossart, D. Brühwiler, S. Huber, C. Leiggener, M. K. van Veen, A. Zabala Ruiz
Comptes-rendus Chimie 9 (2006) 214 – 225.

Functionalization of the External Surface of Zeolite L
D. Brühwiler, G. Calzaferri*
Comptes-rendus Chimie 8 (2005) 391 – 398.

Synthesis of Zeolite L: Tuning Size and Morphology
A. Zabala Ruiz, D. Brühwiler, T. Ban, G. Calzaferri*
Chemical Monthly 136 (2005) 77 – 89.

Selective Modification of the Channel Entrances of Zeolite L with Triethoxysilylated Coumarin
T. Ban, D. Brühwiler, G. Calzaferri*
Journal of Physical Chemistry B 108 (2004) 16348 – 16352.

Molecular Sieves as Host Materials for Supramolecular Organization
D. Brühwiler*, G. Calzaferri*
Microporous and Mesoporous Materials 72 (2004) 1 – 23.

Luminescence Properties of Ag_2S and Ag_4S_2 in Zeolite A
C. Leiggener, D. Brühwiler, G. Calzaferri*
Journal of Materials Chemistry 13 (2003) 1969 – 1977.

Structure of Ni(II) and Ru(III) Ammine Complexes Grafted onto Mesoporous Silicate Sieve
D. Brühwiler, H. Frei*
Journal of Physical Chemistry B 107 (2003) 8547 – 8556.

Luminescent Silver Sulfide Clusters
D. Brühwiler, C. Leiggener, S. Glaus, G. Calzaferri*
Journal of Physical Chemistry B 106 (2002) 3770 – 3777.

Silver Ions and Quantum-Sized Silver Sulfide Clusters in Zeolite A
D. Brühwiler, C. Leiggener, G. Calzaferri*
Studies in Surface Science and Catalysis 135 (2001) 2167 – 2172.

Quantum-Sized Silver, Silver Chloride and Silver Sulfide Clusters
G. Calzaferri*, D. Brühwiler, S. Glaus, D. Schürch, A. Currao, C. Leiggener
Journal of Imaging Science and Technology 45 (2001) 331 – 339.

Playing with Dye Molecules at the Inner and Outer Surface of Zeolite L
G. Calzaferri*, D. Brühwiler, S. Megelski, M. Pfenniger, M. Pauchard, B. Hennessy, H. Maas, A. Devaux, U. Graf
Solid State Sciences 2 (2000) 421 – 447.

Quantum-Sized Silver Sulfide Clusters in Zeolite A
D. Brühwiler, R. Seifert, G. Calzaferri*
Journal of Physical Chemistry B 103 (1999) 6397 – 6399.

Resorufin in the Channels of Zeolite L
D. Brühwiler, N. Gfeller, G. Calzaferri*
Journal of Physical Chemistry B 102 (1998) 2923 – 2929.

(June 2010)

Supervised PhD Theses (completed)

Synthesis and Analysis of Amino-Functionalised Mesoporous Silica
Hanna Ritter
University of Zurich, 07/2005 – 01/2009.

Synthesis and Fluorescent Labeling of Functional Silica Nanochannels
Jan Hinrich Ramm
University of Zurich, 11/2005 – 11/2009.

Zeolite L Antenna Materials for Organic Solar Cells and Luminescent Solar Concentrators
Le-Quyenh Dieu
University of Zurich, 03/2006 – 12/2009.

(June 2010)